



ELSEVIER

Contents lists available at ScienceDirect

## Comput. Methods Appl. Mech. Engrg.

journal homepage: [www.elsevier.com/locate/cma](http://www.elsevier.com/locate/cma)

# Multi-material topology optimization based on finite strain subloading surface nonlocal elastoplasticity

Jike Han <sup>a</sup> , Yuki Yamakawa <sup>b</sup> , Kazuhiro Izui <sup>c</sup> , Shinji Nishiwaki <sup>a</sup> , Kenjiro Terada <sup>b</sup>

<sup>a</sup> Department of Mechanical Engineering and Science, Kyoto University, Kyoto-daigaku Katsura C3, Nishikyo-ku, Kyoto, 615-8540, Japan

<sup>b</sup> Department of Civil and Environmental Engineering, Tohoku University, 6-6-06 Aramaki Aza Aoba, Aoba-ku, Sendai, 980-8579, Japan

<sup>c</sup> Department of Micro Engineering, Kyoto University, Kyoto-daigaku Katsura C3, Nishikyo-ku, Kyoto, 615-8540, Japan

## ARTICLE INFO

### Keywords:

Topology optimization  
Multi-material  
Plasticity  
Finite strain  
Subloading surface model

## ABSTRACT

This study is dedicated to the multi-material topology optimization formulation (MMTO) for finite strain nonlocal elastoplasticity. The subloading surface model is newly incorporated into the primal problem to achieve the gradual change of the deformation process from pure elastic to material-specific plastic hardening. The stress–strain relationship of the model is a smooth continuous function, which is beneficial for elastoplastic topology optimization since the resulting continuous tangent is used in the adjoint problem to determine the sensitivity. Also, the nonlocal plastic modeling is introduced to resolve mesh-dependency issues in the evolution of plastic deformation. In addition, in order to maintain computational stability and to avoid unrealistic plastic deformation occurring in voids (ersatz material), the concept of interpolating energy densities is introduced, by which linearly elastic material is chosen to represent voids. The continuous adjoint method is employed to derive the governing equations and sensitivity of the adjoint problem, and the resulting equations are valid at any position, boundary, or time in the continuum without relying on any discretization. An arbitrary number of design variables can be considered for multiple materials in the optimization problem, and by referring to the derived sensitivity, the multiple reaction–diffusion equations are solved to update the material distribution and configuration. The first numerical example demonstrates the “oscillation of deformation states” caused by the conventional plastic model and shows how the subloading surface model effectively resolves this issue, achieving stable optimization processes. Also, the second example presents the unconventional deformation magnitude-dependent stiffness maximization problems with multiple materials, in which the optimal designs are realized by referring to the same elastic but different plastic material properties.

## 1. Introduction

Topology optimization [1] is a powerful computational method for designing structures and materials with desired performance. The core of topology optimization is an iterative process of determining the distribution and configuration of material within a given design domain to achieve the best possible performance according to the set design objectives. This methodology can be widely applied to various fields, including aerospace, automotive, civil engineering, and materials science. Topology optimization was originally studied to determine the optimal distribution and configuration of a single material, and this is called “single-material

\* Corresponding author.

E-mail address: [han.jike.8r@kyoto-u.ac.jp](mailto:han.jike.8r@kyoto-u.ac.jp) (J. Han).

<https://doi.org/10.1016/j.cma.2025.118038>

Received 23 November 2024; Received in revised form 17 April 2025; Accepted 19 April 2025

Available online 9 May 2025

0045-7825/© 2025 The Author(s). Published by Elsevier B.V. This is an open access article under the CC BY-NC-ND license (<http://creativecommons.org/licenses/by-nc-nd/4.0/>).

topology optimization (SMTO)”. However, the fact that many industries usually combine multiple materials to create structures has led to research in “multi-material topology optimization (MMTO)”. The first idea about MMTO was from Bendsoe & Sigmund [2]. To date, the level-set-based and density-based methods are two widely known approaches.

Regarding the level-set-based method, the following studies are representative of MMTOs to address mechanical problems: Wang & Wang [3] proposed a level-set-based method for shape and topology optimization, in which the model eliminates the need for the material interpolation or phase mixing scheme and only requires  $m$  level-set functions to represent a structure of  $2^m$  different materials. Wang et al. [4] presented a level-set-based method for topology and shape optimizations. In this method, there is only one material at each position, which does not allow two materials to overlap. Also, the sensitivity analysis is facilitated thanks to the explicit mathematical expression of the method. Liu et al. [5] developed an efficient MMTO strategy for seeking the optimal layout of structures considering the traction–separation relationship of the interface, for which the interface behavior is simulated by combining the extended finite element method and the cohesive zone model. Vogiatzis et al. [6] developed a level-set-based method for SMTO and MMTO to address the optimal design for materials with negative Poisson’s ratio, in which MMTO is simplified by making each individual material evolve with a single level-set function and reconciling the level-set field with the Merriman–Bence–Osher operator. Ghasemi et al. [7] developed an MMTO framework for designing optimal multi-material-based flexoelectric composites, for which the multiphase vector level-set model is employed for satisfying multiple constraints and avoiding the overlap or vacuum among different phases. Gangl [8] proposed a level-set-based topology optimization algorithm for MMTO, in which the evolution of an optimization process for designing a structure constructed by multiple linear elastic materials is described by topological derivatives.

On the other hand, the following studies are relatively well-known among scholars as representatives of density-based MMTO: Zhou & Wang [9] proposed a phase-field method for MMTO, in which a Cahn–Hilliard type penalization function is inserted into the objective function to regularize the optimization problem and penalize material distribution. Hvejsel & Lund [10] presented two multi-material interpolation schemes as the direct generalizations of the Solid Isotropic Material with Penalization (SIMP) and Rational Approximation of Material Properties (RAMP) interpolation schemes, which rely on a large number of sparse linear constraints to enforce the selection of at most one material. Zuo & Saitou [11] proposed an ordered SIMP interpolation function for MMTO, by which one design variable can handle the interpolation of multiple material parameters so that the computational cost becomes independent of the number of materials under consideration. Lieu & Lee [12] presented a multi-resolution scheme for MMTO in the framework of isogeometric analysis, in which the high-resolution optimized design is realized by relying on the capability of the non-uniform rational B-spline basis functions. Gao et al. [13] proposed a multi-material isogeometric topology optimization method to address MMTO, in which the non-uniform rational B-splines basis functions are used to interpolate material properties, and the low complexity of numerical computations are achieved in MMTO. Liu et al. [14] presented a designable connective region method for creating connectable microstructures by considering repetitive unit cells and prescribed porosity, by which the connectivity between any two types of microstructures is naturally ensured. Xu et al. [15] employed the ordered SIMP method to address the stress-constrained MMTO, in which another ordered SIMP-like interpolation function is proposed to realize the relaxed and scaled stress interpolation. Han & Wei [16] developed an alternating active phase and objective algorithm for MMTO, by which the objective function is switched according to the active phases, and the proposed formulation resolves the convergence oscillation issue.

Many of the related studies to date, including those cited above, have mainly contributed to developing new and better methodologies/algorithms for MMTO. In other words, the motivation was to propose new and better MMTO frameworks, but it was not to tackle solving optimization problems while considering the advanced or complex primal problem. Thus, to the best of our knowledge, most of them simply assume linear elasticity for the material response, and the research primarily focused on material nonlinearity has not been the mainstream of MMTO development. However, considering the emergence of additive manufacturing and giga-casting for metallic materials, which have high affinities to MMTO, material nonlinearities, such as plastic material behavior with large deformation, can no longer be ignored. That is, there should be sufficient reason to study MMTO for elastoplastic materials. Unfortunately, however, even though elastoplastic topology optimization is one of the most intensively studied topics among researchers, to the best of our knowledge, it has yet to be enhanced in the direction of MMTO. As far as SMTO is concerned, numerous attempts have been made within the framework of small strain elastoplasticity, e.g., see Refs. [17–28]. However, as suggested above, since elastoplastic materials usually exhibit large deformation once plastic deformation occurs, the authors argue that kinematics should involve geometrical nonlinearity. From this perspective, Wallin et al. [29], Ivarsson et al. [30,31], Zhang & Khandelwal [32], Han et al. [33], and Kim et al. [34] developed finite strain SMTO for elastoplastic materials independently. It is worth mentioning that Han et al. [33] concisely review studies on elastoplastic topology optimization published up to that time. More recently, Han et al. [35] proposed a finite strain topology optimization formulation for nonlocal elastoplasticity to resolve mesh-dependency issues in the evolution of plastic deformation.

Meanwhile, it should be noted that all of the previous studies describe the elastoplastic material response by the “conventional plastic model”. That is, the deformation process is completely divided into two states, i.e., the elastic and plastic deformation states, at the plastic yielding point (initial yield stress). Assuming elastoplastic materials with linear plastic hardening, the corresponding material Jacobians (elastic material Jacobian and elastoplastic material Jacobian) have different order values, and the stress–strain relationship around the plastic yield point is nonsmooth, leading to a discontinuous material Jacobian; see the black-colored lines in Fig. 1. This mathematical structure is extremely unpleasant from the viewpoint of the adjoint method, which uses local material Jacobians (at material point level) of the primal problem to determine the adjoint variables and sensitivities for updating material

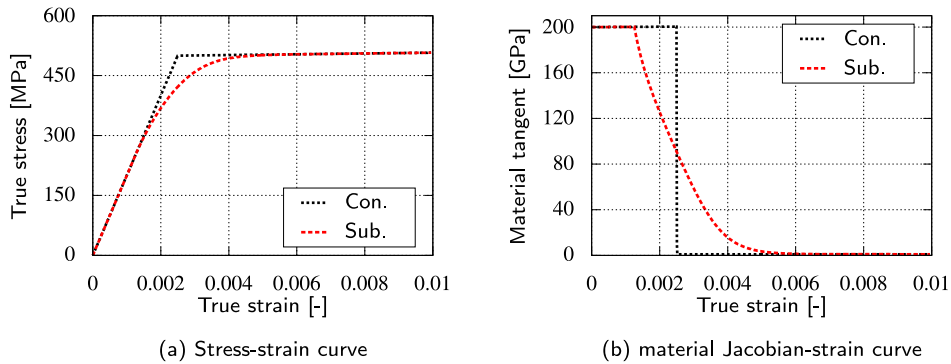


Fig. 1. Elastoplastic responses of conventional plastic model (Con.) and subloading surface model (Sub.).

distributions. More precisely, the material Jacobian in the elastic deformation state generally has a much larger value than that in the plastic deformation state, and the value may change dramatically around the plastic yield point. Thereby, the deformation state may be repeatedly changed in the optimization process at locations having strain rate around the plastic yield point, making the optimization process difficult to converge. This phenomenon was reported by Han et al. [35] and is again studied in Example 1 of this study. Although this problem can be alleviated by relaxing the convergence threshold or introducing another stabilization technique, one can also reconsider the elastoplastic constitutive law as a countermeasure. To this end, the subloading surface model [36–38] can be a promising candidate to replace the conventional plastic model as its material response is smooth as illustrated by the red-colored line in Fig. 1(a). This is because the subloading surface model has a transition range from the pure elastic deformation to the material-specific plastic hardening behavior, leading to the continuous transition from the elastic Jacobian to the elastoplastic Jacobian as shown by the red-colored line in Fig. 1(b). Hence, by enjoying the material response of the subloading surface model, the aforementioned oscillatory behavior is expected to be mitigated, which is beneficial to realize a stable or robust topology optimization process, as demonstrated in Example 1 of this study. It is also notable to note that the subloading surface model and the conventional plastic model have equivalent material response expressions, except for the difference in deformation state transitions.

With the above background, this study presents an MMTO framework for finite strain nonlocal elastoplasticity. As the primal problem to describe the material response, the subloading surface model is incorporated with the standard hyperelastic constitutive law. Also, following Han et al. [35], the nonlocal plastic modeling, say micromorphic regularization [39], is introduced to resolve mesh-dependency issues in the evolution of plastic deformation. For the optimization problem, an arbitrary number of design variables is considered to address MMTO. Interpolation of material parameters between actual materials follows the conventional SIMP-based interpolation function, whereas the energy function interpolation [40,41] is adopted for interpolation between ersatz (voids) and actual materials. Assuming that the ersatz material (voids) is purely elastic, the presence of voids does not reduce the computational stability of the primal problem because it does not exhibit unrealistic plastic deformation. Meanwhile, the continuous adjoint method is employed to derive the governing equations of the adjoint problem, from which the same number of sensitivities as the design variables are obtained. In the end, the reaction–diffusion equation-based method [33,42,43] is enhanced to update multiple design variables simultaneously.

This paper is organized as follows: In Section 2, MMTO for finite strain nonlocal elastoplasticity is formulated. The first half of Section 3 presents the spatial and temporal discretizations applied to the governing equations of the primal and adjoint problems, and the second half describes the design variable update. In Section 4, two numerical examples are presented: the first example aims to demonstrate the capability of the subloading surface model in topology optimization, and the second one is dedicated to the demonstration of MMTO realized by referring to different degrees of plastic hardening behavior. Finally, in Section 5, the summary of this study is presented, and our future plans are briefly revealed.

## 2. Formulation

This section presents a formulation of multi-material topology optimization (MMTO) for finite strain nonlocal elastoplasticity. To summarize the underlying kinematics, a nomenclature is prepared in Table 1, which covers most variables, parameters, and symbols used in this study. In what follows, the governing equations of the primal problem are derived first and subsequently modified for stable MMTO by employing the idea of the interpolation scheme for fictitious domain [40,41]. Then, the governing equations of the adjoint problem and the resulting sensitivity for MMTO are derived based on the continuous adjoint method. It is worth mentioning

**Table 1**  
Nomenclature.

Name	Letter	Description
Real coordinate space	$\mathbb{R}^n$	$n = 2, 3$
Actual time for primal and adjoint problems	$\mathcal{T}$	$t \in \mathcal{T} = [0, T]$
Pseudo time for optimization	$\tilde{\mathcal{T}}$	$\tilde{t} \in \tilde{\mathcal{T}} = [0, \tilde{T}]$
Initial configuration of a continuum body	$B_0$	$B_0 \subset \mathbb{R}^n$
Initial boundary	$\partial B_0$	$\partial B_0 \subset \mathbb{R}^{n-1}$
Initial Neumann and Dirichlet boundaries	$\partial B_0^N$ and $\partial B_0^D$	$\partial B_0^N \cup \partial B_0^D = \partial B_0, \partial B_0^N \cap \partial B_0^D = \emptyset$
Points at the initial configuration	$\mathbf{X}$	$\mathbf{X} \in B_0$
Current configuration of a continuum body	$B_t$	$B_t \subset \mathbb{R}^n$
Current boundary	$\partial B_t$	$\partial B_t \subset \mathbb{R}^{n-1}$
Current Neumann and Dirichlet boundaries	$\partial B_t^N$ and $\partial B_t^D$	$\partial B_t^N \cup \partial B_t^D = \partial B_t, \partial B_t^N \cap \partial B_t^D = \emptyset$
Points at the current configuration	$\mathbf{x}$	$\mathbf{x} \in B_t$
Displacement vector	$\mathbf{u}$	$\mathbf{u} = \mathbf{x} - \mathbf{X}$
Deformation gradient tensor	$\mathbf{F}$	$\mathbf{F} = \partial \mathbf{x} / \partial \mathbf{X}$
Elastic and plastic deformation gradient tensors	$\mathbf{F}^e$ and $\mathbf{F}^p$	$\det[\mathbf{F}^e] = \det[\mathbf{F}] = J^e, \det[\mathbf{F}^p] = 1$
Elastic left Cauchy–Green tensor	$\mathbf{b}^e$	$\mathbf{b}^e = \mathbf{F}^e \cdot \mathbf{F}^{eT}$
Rate of deformation tensor	$\mathbf{d}$	$\mathbf{d} = \text{sym}[\dot{\mathbf{F}} \cdot \mathbf{F}^{-1}]$
Rate of plastic deformation tensor	$\mathbf{d}^p$	$\mathbf{d}^p = \mathbf{F}^e \cdot \text{sym}[\dot{\mathbf{F}}^p \cdot \mathbf{F}^{p-1}] \cdot \mathbf{F}^{e-1}$
Local and nonlocal plastic hardening variables	$\alpha$ and $\bar{\alpha}$	$\alpha$ is known as “accumulated plastic strain”.
Elastic strain energy density	$\Psi^e$	$\Psi^e(\mathbf{b}^e)$
Plastic strain energy density	$\Psi^p$	$\Psi^p(\alpha)$
Micromorphic regularization energy density	$\Psi^m$	$\Psi^m(\alpha, \bar{\alpha}, \nabla \bar{\alpha})$
Kirchhoff stress tensor (or plastic force)	$\boldsymbol{\tau}$	$\boldsymbol{\tau} = 2\partial_{\mathbf{b}^e} \Psi^e \cdot \mathbf{b}^e$
First Piola–Kirchhoff stress tensor	$\mathbf{P}$	$\partial_x \Psi^e, \mathbf{P} = \boldsymbol{\tau} \cdot \mathbf{F}^{-T}$
Plastic hardening force (or resistant force)	$r^p$	$r^p = \partial_\alpha \Psi^p + \partial_\alpha \Psi^m$
Body force vector	$\mathbf{B}$	w.r.t. initial configuration
Traction force vector	$\mathbf{T}$	$\mathbf{T} = \mathbf{P} \cdot \mathbf{N}$
Prescribed traction force vector	$\tilde{\mathbf{T}}$	w.r.t. initial configuration
Prescribed displacement vector	$\tilde{\mathbf{u}}$	w.r.t. initial configuration
Outward unit normal vector	$\mathbf{N}$	w.r.t. initial configuration
Yield functions	$\Phi_{\text{sub}}^p$ and $\Phi_{\text{ela}}^p$	–
Plastic multiplier	$\gamma^p$	$\dot{\gamma}^p \geq 0$
Flow tensor	$\mathbf{n}$	$\mathbf{n} = \mathbf{n}^T$
Normal-yield ratio	$R$	$0 \leq R \leq 1$
Normal-yield threshold and saturation parameter	$R^c$ and $R^p$	–
Bulk and shear moduli	$\kappa$ and $\mu$	$\kappa = E / \{3(1 - 2\nu)\}$
Young’s modulus and Poisson’s ratio	$E$ and $\nu$	$\mu = E / \{2(1 + \nu)\}$
Plastic hardening parameters	$\gamma_0, h, \gamma_\infty,$ and $s_y$	–
Penalty and diffusion parameters for regularization	$p_p$ and $q_p$	–
Initial design domain	$D_0$	$D_0 \subset \mathbb{R}^n$
Initial design boundary	$\partial D_0$	$\partial D_0 \subset \mathbb{R}^{n-1}$
Initial Neumann design boundary	$\partial D_0^N$	$\partial D_0^N \cup \partial D_0^D = \partial D_0$
Initial Dirichlet design boundary	$\partial D_0^D$	$\partial D_0^N \cap \partial D_0^D = \emptyset$
Design variable	$\omega_i$	$i = 1, \dots, m$
Objective function and objective density functions	$F$ and $f_{B_0}$ & $f_{\partial B_0}$	–
Adjoint displacement vector	$\mathbf{w}$	–
Adjoint plastic multiplier	$\eta^p$	–
Adjoint flow tensor	$\boldsymbol{\pi}$	–
Adjoint nonlocal hardening variable	$\tilde{\beta}$	–
Adjoint deformation gradient tensor	$\mathbf{H}$	$\mathbf{H} = \partial \mathbf{w} / \partial \mathbf{X}$
Sensitivity	$s_{D_{0,i}}, s_{\partial D_0^N,i},$ and $s_{\partial D_0^D,i}$	$i = 1, \dots, m$

that although the elastoplastic formulation is mostly based on the conventional elastoplastic theory [44,45], the subloading surface theory [36,37] (or the normal-yield ratio) is newly employed to stably treat elastoplastic material response during the optimization process. Also, multiple design variables are defined to realize MMTO, each of which is updated by referring to the corresponding sensitivity by the reaction–diffusion equation.

**2.1. Primal problem**

In order to describe the nonlocal elastoplastic response in the primal problem, the subloading surface theory is employed in this study. It is worth mentioning that this theory has a long history and has been enhanced to fit various application targets, such as Hashiguchi [36] and Toluei & Kharazi [46,47] for isotropic/anisotropic plastic materials, Darabi et al. [48] for viscoplastic materials, Zhang et al. [49] for thermo-elastoplastic materials, Sun & Zhou [50] for multisurface elastoplastic materials, Asaoka et al. [51], Nakai & Hinokio [52], Hashiguchi et al. [53], and Yamakawa et al. [54] for soils, Hashiguchi et al. [55] for glassy materials,

Lai et al. [56] for damage evolutions, Hashiguchi & Ozaki [57] for friction problems, and so on. Since hundreds studies have been reported, readers can refer to Hashiguchi [36] and Hashiguchi & Yamakawa [37] for theoretical development and Hashiguchi et al. [38,58] for a comprehensive review.

First, the following energy density function corresponding to the elastoplastic material behavior represented by the subloading surface model is defined:

$$\psi^{\text{act}} = \psi^e(\mathbf{b}^e) + \psi^p(\alpha) + \psi^m(\alpha, \bar{\alpha}, \nabla \bar{\alpha}), \tag{1}$$

where  $\psi^e$ ,  $\psi^p$ , and  $\psi^m$  denote the elastic strain energy density, plastic strain energy (or plastic hardening energy) density, and micromorphic regularization energy density, respectively. Although any material constitutive laws are possible, the following Neo-Hookean material model and Voce hardening law are chosen to represent the elastic and plastic responses in this study:

$$\psi^e(\mathbf{b}^e) = \frac{\kappa}{2} \left( \frac{J^{e2} - 1}{2} - \ln J^e \right) + \frac{\mu}{2} (J^{e-2/3} \text{tr}[\mathbf{b}^e] - 3) \tag{2}$$

and

$$\psi^p(\alpha) = \int_0^\alpha (h\bar{\alpha} + (y_\infty - y_0)(1 - \exp(-s_y \bar{\alpha}))) d\bar{\alpha}. \tag{3}$$

Also, referring to Forest [39] and Han et al. [59], the second-order regularization functional for plasticity is adopted:

$$\psi^m(\alpha, \bar{\alpha}, \nabla \bar{\alpha}) = \frac{1}{2} p_p (\alpha - \bar{\alpha})^2 + \frac{1}{2} q_p \nabla \bar{\alpha} \cdot \nabla \bar{\alpha}. \tag{4}$$

It is noted that although the original subloading surface model is the so-called ‘‘local approach’’, in which the plastic evolution is solved at integration points, the micromorphic regularization [39] has been adopted to extend the model to be a ‘‘nonlocal approach’’. This extension can resolve the mesh-dependency issue of plasticity and has been demonstrated by Han et al. [35] for the single-material topology optimization (SMTO) of standard elastoplastic materials. Roughly speaking, the procedure to introduce micromorphic regularization into the subloading surface model is the same as the procedure for a standard elastoplastic model. Thus, readers can also refer to Han et al. [35] for details.

Next, to represent the elastoplastic response in terms of the subloading surface theory, the following yield functions and evolution laws of plasticity are postulated:

$$\Phi_{\text{sub}}^p = \|\tau_{\text{dev}}\| - R\sqrt{\frac{2}{3}}(y_0 + r^p), \quad \Phi_{\text{ela}}^p = \|\tau_{\text{dev}}\| - R^e\sqrt{\frac{2}{3}}(y_0 + r^p), \tag{5}$$

and

$$\mathbf{d}^p = \gamma^p \frac{\tau_{\text{dev}}}{\|\tau_{\text{dev}}\|}, \quad \dot{\alpha} = \sqrt{\frac{2}{3}} \gamma^p. \tag{6}$$

Notably, the plastic incompressibility (or the isochoric plastic flow) is ensured, i.e.,  $\det[\mathbf{F}^p] = 1$ . Also, the subloading surface model has four deformation states, i.e., elastic loading, plastic loading, elastic unloading, and plastic reloading, which can be determined algorithmically. Notably, because of this algorithmic treatment, the Karush–Kuhn–Tucker conditions (loading/unloading conditions) are not needed here. The method of determining deformation states is explained in detail in Section 3.1. Also, the subloading surface theory follows the associated flow rule, while the evolution law of plastic hardening variable in Eq. (6)<sub>2</sub> is postulated independent of the yield criterion. In this sense, the isotropic hardening law is considered non-associative.

In the end, after some manipulation [33,35], four governing equations of the primal problem are obtained as follows:

$$\left. \begin{aligned} \nabla \cdot \mathbf{P} + \mathbf{B} = \mathbf{0} \text{ in } B_0, \quad \mathbf{P} \cdot \mathbf{N} = \bar{\mathbf{T}} \text{ on } \partial B_0^N, \quad \mathbf{u} = \bar{\mathbf{u}} \text{ on } \partial B_0^D \\ \|\tau_{\text{dev}}\| - R\sqrt{\frac{2}{3}}(y_0 + r^p) = 0 \text{ in } B_0 \\ \mathbf{n} - \frac{\tau_{\text{dev}}}{\|\tau_{\text{dev}}\|} = \mathbf{0} \text{ in } B_0 \\ p_p(\bar{\alpha} - \alpha) - q_p \nabla^2 \bar{\alpha} = 0 \text{ in } B_0, \quad q_p \nabla \bar{\alpha} \cdot \mathbf{N} = 0 \text{ on } \partial B_0 \end{aligned} \right\} \forall t. \tag{7}$$

Notably, under the elastic loading/unloading states, Eq. (7)<sub>2,3</sub> are not solved.

### 2.2. Modification by interpolation scheme for fictitious domain

To describe the MMTO for  $m+1$  materials,  $m$  scalar-valued design variables  $\omega_i(\mathbf{X}) \in [0, 1]$  with  $i = 1, 2, \dots, m-1, m$  are introduced. Then, one of the straightforward strategies for determining material properties in MMTOs is using the following SIMP-based interpolation function:

$$\begin{aligned} \bullet_{1,2,\dots,m,m+1} &= \omega_m^p \bullet_{1,2,\dots,m-1,m} + (1 - \omega_m^p) \bullet_{m+1} \\ &= \omega_m^p (\omega_{m-1}^p \bullet_{1,2,\dots,m-2,m-1} + (1 - \omega_{m-1}^p) \bullet_m) + (1 - \omega_m^p) \bullet_{m+1} \\ &= \omega_m^p \omega_{m-1}^p (\omega_{m-2}^p \bullet_{1,2,\dots,m-3,m-2} + (1 - \omega_{m-2}^p) \bullet_{m-1}) + \omega_m^p (1 - \omega_{m-1}^p) \bullet_m + (1 - \omega_m^p) \bullet_{m+1} \\ &= \dots \\ &= \left( \prod_{j=1}^m \omega_j^p \right) \bullet_1 + \sum_{j=2}^m \left( \prod_{k=j}^m \omega_k^p \right) (1 - \omega_{j-1}^p) \bullet_j + (1 - \omega_m^p) \bullet_{m+1}, \end{aligned} \tag{8}$$

where  $\bullet_{1,2,\dots,m,m+1}$  denotes the resulting material constant interpolated by  $m + 1$  base materials, and  $\bullet_1, \bullet_j$ , and  $\bullet_{m+1}$  are the 1-st,  $j$ th, and  $m+1$ -th base material constants, respectively. Readers can also refer to Appendix A.1 for some example cases of Eq. (9). However, when the primal problem is formulated within the finite strain framework, and when the voids (fictitious domain) are assumed to be one of the base materials, the appearance of voids (fictitious domains) significantly reduces the computational stability of the global Newton–Raphson computation. This is mainly because the Young’s modulus of the fictitious domains is set much smaller than those of the domains filled with actual materials. Also, the fictitious domain may exhibit unrealistic plastic deformation that is unpleasant in terms of both physical and numerical aspects. Accordingly, the mesh distortion or displacement oscillation is easily caused by the bad condition number of the global tangent matrix.

In this study, the primal problem is modified by introducing the interpolation scheme for fictitious domain [40,41] to maintain computational stability. Specifically, the 1-st- $m$ -th materials follow the SIMP-based interpolation function in Eq. (9), i.e.,

$$\bullet_{1,2,\dots,m} = \left( \prod_{j=1}^{m-1} \omega_j^p \right) \bullet_1 + \sum_{j=2}^{m-1} \left( \prod_{k=j}^{m-1} \omega_k^p \right) (1 - \omega_{j-1}^p) \bullet_j + (1 - \omega_{m-1}^p) \bullet_m. \tag{9}$$

Then, assuming that the void corresponds to the  $m + 1$ -th material, the energy density functional of the actual material  $\Psi^{\text{act}}$  and a fictitious energy density functional representing the void  $\Psi^{\text{fic}}$  are interpolated by the “last” design variable  $\omega_m$  to determine the resulting energy density functional  $\Psi$  as follows:

$$\Psi = \omega_m^p \Psi^{\text{act}} + (1 - \omega_m^p) \Psi^{\text{fic}} = \omega_m^p \underbrace{(\Psi^e + \Psi^p + \Psi^m)}_{\text{See Eqs. (2)~(4)}} + (1 - \omega_m^p) \Psi^{\text{fic}}. \tag{10}$$

Notably, all material parameters of the 1-st- $m$ -th materials, i.e.,  $E, \nu, \gamma_0, h, \gamma_\infty, s_y, p_p, q_p, R^e$ , and  $R^p$ , follow the interpolation rule in Eq. (9). Also,  $\Psi^{\text{fic}}$  is supposed to take the linearly elastic component only as follows:

$$\Psi^{\text{fic}}(\epsilon) = \frac{1}{2} \kappa_m \text{tr}[\epsilon]^2 + \mu_m \epsilon_{\text{dev}} : \epsilon_{\text{dev}} \quad \text{with } \epsilon = \frac{\mathbf{F} + \mathbf{F}^T}{2} - \mathbf{1}, \tag{11}$$

in which  $\kappa_m$  and  $\mu_m$  are the bulk and shear moduli of the fictitious domain, respectively, and  $\epsilon$  denotes the small strain tensor. It is worth mentioning that because the linearly elastic material is assumed for fictitious domains, the problem of reduced computational stability pointed out above can be alleviated.

Reflecting the modified energy density function in Eq. (10) to the primal problem, the governing equations are rewritten as

$$\left. \begin{aligned} \nabla \cdot (\omega_m^p \mathbf{P} + (1 - \omega_m^p) \boldsymbol{\sigma}^f) + \omega_m^p \mathbf{B} &= \mathbf{0} \text{ in } B_0, \\ (\omega_m^p \mathbf{P} + (1 - \omega_m^p) \boldsymbol{\sigma}^f) \cdot \mathbf{N} &= \bar{\mathbf{T}} \text{ on } \partial B_0^N, \quad \mathbf{u} = \bar{\mathbf{u}} \text{ on } \partial B_0^D \\ \omega_m^p \left( \|\boldsymbol{\tau}_{\text{dev}}\| - R \sqrt{\frac{2}{3}} (\gamma_0 + r^p) \right) &= 0 \text{ in } B_0 \\ \omega_m^p \left( \mathbf{n} - \frac{\boldsymbol{\tau}_{\text{dev}}}{\|\boldsymbol{\tau}_{\text{dev}}\|} \right) &= \mathbf{0} \text{ in } B_0 \\ \omega_m^p (p_p (\bar{\alpha} - \alpha) - q_p \nabla^2 \bar{\alpha}) &= 0 \text{ in } B_0, \quad \omega_m^p q_p \nabla \bar{\alpha} \cdot \mathbf{N} = 0 \text{ on } \partial B_0 \end{aligned} \right\} \forall t, \tag{12}$$

where  $\boldsymbol{\sigma}^f = \partial_{\mathbf{F}} \Psi^{\text{fic}} = \kappa_m \text{tr}[\epsilon] \mathbf{1} + 2\mu_m \epsilon_{\text{dev}}$  denotes the fictitious stress tensor. Here, recalling the fact that the body force cannot be defined in the fictitious domain, the following relationship has been adopted in Eq. (12):

$$\mathbf{B}_{1,2,\dots,m,m+1} = \omega_m^p \underbrace{\mathbf{B}_{1,2,\dots,m}}_{=: \mathbf{B}} + (1 - \omega_m^p) \underbrace{\mathbf{B}_{m+1}}_{=0} = \omega_m^p \mathbf{B}. \tag{13}$$

Also, the traction force  $\mathbf{T}$  on the Dirichlet boundary is rewritten as

$$\mathbf{T} = (\omega_m^p \mathbf{P} + (1 - \omega_m^p) \boldsymbol{\sigma}^f) \cdot \mathbf{N}. \tag{14}$$

It is worth noting that in the fictitious domain ( $\omega_m = 0$ ), the above setup results in the following governing equations of the linear elasticity problem:

$$\nabla \cdot \boldsymbol{\sigma}^f = \mathbf{0} \text{ in } B_0, \quad \boldsymbol{\sigma}^f \cdot \mathbf{N} = \bar{\mathbf{T}} \text{ on } \partial B_0^N, \quad \mathbf{u} = \bar{\mathbf{u}} \text{ on } \partial B_0^D \quad \forall t. \tag{15}$$

### 2.3. Optimization problem

Taking the design variables  $\{\omega_1, \omega_2, \dots, \omega_{m-1}, \omega_m\}$  into account, the following objective function  $\mathcal{F}$  is defined for arbitrary design objectives to realize:

$$\begin{aligned} & \mathcal{F}(\omega_1, \omega_2, \dots, \omega_{m-1}, \omega_m) \\ &= \int_t \left[ \int_{B_0} f_{B_0}(\mathbf{u}, \mathbf{F}, \gamma^p, \mathbf{n}, \bar{\alpha}, \nabla \bar{\alpha}, \omega_1, \dots, \omega_m) \text{dV} + \int_{\partial B_0} f_{\partial B_0}(\mathbf{u}, \mathbf{T}, \bar{\alpha}, \omega_1, \dots, \omega_m) \text{dA} \right] \text{dt}, \end{aligned} \tag{16}$$

where  $f_{B_0}$  and  $f_{\partial B_0}$  denote the objective density functions inside the body and on the surface, respectively. To avoid losing the generality of the optimization problem as much as possible,  $f_{B_0}$  and  $f_{\partial B_0}$  are written in abstract forms and assumed to accommodate

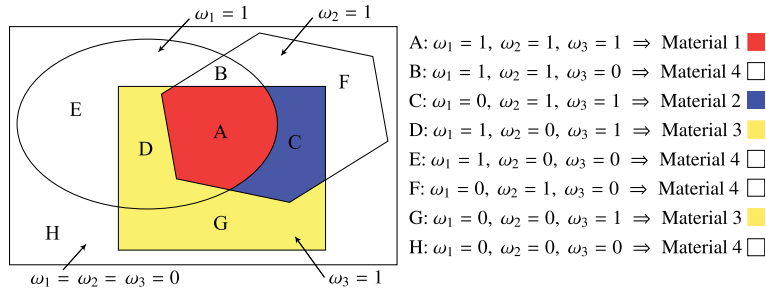


Fig. 2. Relationship between three design variables and four material placements. ( $m = 3$ ).

multiple objectives. Also, it is worth mentioning that  $f_{\partial B_0}$  does not rely on  $\nabla \bar{\alpha}$  since the Dirichlet boundary is not defined for the micromorphic plastic field. Then, the optimization problem is defined as follows:

$$\begin{aligned} & \text{Maximize}_{\forall \omega_1, \omega_2, \dots, \omega_{m-1}, \omega_m \in D_0} \mathcal{F}(\omega_1, \omega_2, \dots, \omega_{m-1}, \omega_m) \\ & \text{subject to Eq. (12) and } \bar{V}_1 \leq 0, \bar{V}_2 \leq 0, \dots, \bar{V}_{m-1} \leq 0, \text{ and } \bar{V}_m \leq 0, \end{aligned} \tag{17}$$

in which the plastic deformation state (plastic loading/reloading states) is assumed. Here,  $\bar{V}_1 \leq 0, \bar{V}_2 \leq 0, \dots, \bar{V}_{m-1} \leq 0,$  and  $\bar{V}_m \leq 0$  are the volume constraints, and the left-hand side of each inequality is defined as

$$\bar{V}_i = V_i - V_{i,\max}, \quad (i = 1, 2, \dots, m - 1, m), \tag{18}$$

where  $V_i$  and  $V_{i,\max}$  denote the actual volume and allowable volume of the  $i$ th material, respectively, and  $D_0$  is the design domain. It is worth mentioning that the actual volume of  $i$ th material is calculated by

$$V_i = \int_{D_0} \left( \prod_{k=i}^m \omega_k - \prod_{k=i-1}^m \omega_k \right) dV \tag{19}$$

when the SIMP-based interpolation function in Eq. (9) is used for interpolating material parameters; see Fig. 2 for better understanding. An additional explanation is prepared in Appendix A.2. Also, the algorithmic treatment for volume constraints will be explained in Section 3.3.

### 2.4. Adjoint problem

Recalling the method of Lagrange multipliers (or adjoint method), the optimization problem in Eq. (17) can be rewritten by an equivalent form (Lagrangian) as follows:

$$\begin{aligned} \tilde{\mathcal{F}} = & \int_t \left[ \int_{B_0} f_{B_0} dV + \int_{\partial B_0} f_{\partial B_0} dA \right. \\ & + \int_{B_0} \mathbf{H} : (\omega_m^p \mathbf{P} + (1 - \omega_m^p) \boldsymbol{\sigma}^f) dV - \int_{B_0} \mathbf{w} \cdot \omega_m^p \mathbf{B} dV - \int_{\partial B_0^N} \mathbf{w} \cdot \bar{\mathbf{T}} dA - \int_{\partial B_0^D} \mathbf{w} \cdot \mathbf{T} dA \\ & - \int_{B_0} \eta^p \left( \omega_m^p \left( \|\boldsymbol{\tau}_{\text{dev}}\| - R \sqrt{\frac{2}{3}} (y_0 + r^p) \right) \right) dV - \int_{B_0} \boldsymbol{\pi} : \left( \omega_m^p \left( \mathbf{n} - \frac{\boldsymbol{\tau}_{\text{dev}}}{\|\boldsymbol{\tau}_{\text{dev}}\|} \right) \right) dV \\ & \left. + \int_{B_0} (\omega_m^p (p_p \bar{\beta} (\bar{\alpha} - \alpha) + q_p \nabla \bar{\beta} \cdot \nabla \bar{\alpha})) dV \right] dt - \boldsymbol{\theta} \cdot \bar{\mathbf{V}}, \end{aligned} \tag{20}$$

in which four adjoint variables,  $\mathbf{w}, \eta^p, \boldsymbol{\pi},$  and  $\bar{\beta}$  have been introduced, and  $\mathbf{H} := \nabla \mathbf{w}$  denotes the adjoint deformation gradient tensor. Also,  $\bar{\mathbf{V}} = [\bar{V}_1, \bar{V}_2, \dots, \bar{V}_{m-1}, \bar{V}_m]$  is an array of Eq. (19), and  $\boldsymbol{\theta} = [\theta_1, \theta_2, \dots, \theta_{m-1}, \theta_m]$  is the array of the corresponding penalty parameters, for which the following manipulation is possible:

$$\boldsymbol{\theta} \cdot \bar{\mathbf{V}} = \sum_{l=1}^m \theta_l \bar{V}_l = \sum_{l=1}^m \theta_l V_l - \sum_{l=1}^m \theta_l V_{l,\max} = \sum_{l=1}^m \theta_l \int_{D_0} \left( \prod_{k=l}^m \omega_k - \prod_{k=l-1}^m \omega_k \right) dV - \sum_{l=1}^m \theta_l V_{l,\max}. \tag{21}$$

Subsequently, the first variation of the Lagrangian in Eq. (20) yields

$$\delta \tilde{\mathcal{F}} = \left( \sum_{i=1}^m \delta_{\omega_i} \tilde{\mathcal{F}} \right) + (\delta_{\mathbf{u}} \tilde{\mathcal{F}} + \delta_{\eta^p} \tilde{\mathcal{F}} + \delta_{\boldsymbol{\pi}} \tilde{\mathcal{F}} + \delta_{\bar{\alpha}} \tilde{\mathcal{F}}). \tag{22}$$

Here, the four components in the second bracket are written as, respectively,

$$\begin{aligned} \delta_u \tilde{F} = & \int_t \left[ \int_{B_0} \left( \frac{\partial f_{B_0}}{\partial \mathbf{u}} \cdot \delta \mathbf{u} + \frac{\partial f_{B_0}}{\partial \mathbf{F}} : \delta \mathbf{F} \right) dV + \int_{\partial B_0^N} \frac{\partial f_{\partial B_0^N}}{\partial \mathbf{u}} \cdot \delta \mathbf{u} dA + \int_{\partial B_0^D} \frac{\partial f_{\partial B_0^D}}{\partial \mathbf{T}} \cdot \delta \mathbf{T} dA \right. \\ & + \int_{B_0} \mathbf{H} : \left( \omega_m^p \frac{\partial \mathbf{P}}{\partial \mathbf{F}} + (1 - \omega_m^p) \frac{\partial \boldsymbol{\sigma}^f}{\partial \mathbf{F}} \right) : \delta \mathbf{F} dV - \int_{\partial B_0^D} \boldsymbol{\omega} \cdot \delta \mathbf{T} dA \\ & \left. - \int_{B_0} \eta^p \omega_m^p \frac{\partial \|\boldsymbol{\tau}_{\text{dev}}\|}{\partial \mathbf{F}} : \delta \mathbf{F} dV + \int_{B_0} \boldsymbol{\pi} : \omega_m^p \frac{\partial}{\partial \mathbf{F}} \frac{\boldsymbol{\tau}_{\text{dev}}}{\|\boldsymbol{\tau}_{\text{dev}}\|} : \delta \mathbf{F} dV \right] dt, \end{aligned} \tag{23}$$

$$\begin{aligned} \delta_{\gamma^p} \tilde{F} = & \int_t \left[ \int_{B_0} \frac{\partial f_{B_0}}{\partial \gamma^p} \delta \gamma^p dV + \int_{B_0} \mathbf{H} : \omega_m^p \frac{\partial \mathbf{P}}{\partial \gamma^p} \delta \gamma^p dV \right. \\ & - \int_{B_0} \eta^p \omega_m^p \left( \frac{\partial \|\boldsymbol{\tau}_{\text{dev}}\|}{\partial \gamma^p} - \sqrt{\frac{2}{3}} \left( \frac{\partial R}{\partial \gamma^p} (y_0 + r^p) + R \frac{\partial r^p}{\partial \gamma^p} \right) \right) \delta \gamma^p dV \\ & \left. + \int_{B_0} \boldsymbol{\pi} : \omega_m^p \frac{\partial}{\partial \gamma^p} \frac{\boldsymbol{\tau}_{\text{dev}}}{\|\boldsymbol{\tau}_{\text{dev}}\|} \delta \gamma^p dV - \int_{B_0} \omega_m^p p_p \bar{\beta} \frac{\partial \alpha}{\partial \gamma^p} \delta \gamma^p dV \right] dt, \end{aligned} \tag{24}$$

$$\begin{aligned} \delta_{\mathbf{n}} \tilde{F} = & \int_t \left[ \int_{B_0} \frac{\partial f_{B_0}}{\partial \mathbf{n}} : \delta \mathbf{n} dV + \int_{B_0} \mathbf{H} : \omega_m^p \frac{\partial \mathbf{P}}{\partial \mathbf{n}} : \delta \mathbf{n} dV \right. \\ & \left. - \int_{B_0} \eta^p \omega_m^p \frac{\partial \|\boldsymbol{\tau}_{\text{dev}}\|}{\partial \mathbf{n}} : \delta \mathbf{n} dV - \int_{B_0} \boldsymbol{\pi} : \omega_m^p \left( \mathbf{1} \otimes \mathbf{1} - \frac{\partial}{\partial \mathbf{n}} \frac{\boldsymbol{\tau}_{\text{dev}}}{\|\boldsymbol{\tau}_{\text{dev}}\|} \right) : \delta \mathbf{n} dV \right] dt, \end{aligned} \tag{25}$$

and

$$\begin{aligned} \delta_{\bar{\alpha}} \tilde{F} = & \int_t \left[ \int_{B_0} \left( \frac{\partial f_{B_0}}{\partial \bar{\alpha}} \delta \bar{\alpha} + \frac{\partial f_{B_0}}{\partial \nabla \bar{\alpha}} \cdot \nabla \delta \bar{\alpha} \right) dV + \int_{\partial B_0^N} \frac{\partial f_{\partial B_0^N}}{\partial \bar{\alpha}} \delta \bar{\alpha} dA + \int_{\partial B_0^D} \frac{\partial f_{\partial B_0^D}}{\partial \bar{\alpha}} \delta \bar{\alpha} dA \right. \\ & \left. - \int_{\partial B_0^D} \boldsymbol{\omega} \cdot \frac{\partial \mathbf{T}}{\partial \bar{\alpha}} \delta \bar{\alpha} dA + \int_{B_0} \eta^p \omega_m^p R \sqrt{\frac{2}{3}} \frac{\partial r^p}{\partial \bar{\alpha}} \delta \bar{\alpha} dV + \int_{B_0} \omega_m^p (p_p \bar{\beta} \delta \bar{\alpha} + q_p \nabla \bar{\beta} \cdot \nabla \delta \bar{\alpha}) dV \right] dt, \end{aligned} \tag{26}$$

in which the following relationship has been adopted for the sake of strict representation:

$$\int_{\partial B_0} f_{\partial B_0} dA = \int_{\partial B_0^N} f_{\partial B_0^N} dA + \int_{\partial B_0^D} f_{\partial B_0^D} dA. \tag{27}$$

Here,  $\otimes$  in Eq. (25) denotes the dyadic-up product operator, i.e.,  $(\mathbf{1} \otimes \mathbf{1})_{ijkl} = \delta_{ik} \delta_{jl}$ . Accordingly, the governing equations of the adjoint problem are obtained by forcing  $\delta_u \tilde{F}$ ,  $\delta_{\gamma^p} \tilde{F}$ ,  $\delta_{\mathbf{n}} \tilde{F}$ , and  $\delta_{\bar{\alpha}} \tilde{F}$  to be zero as follows:

$$\left. \begin{aligned} & \frac{\partial f_{B_0}}{\partial \mathbf{u}} - \nabla \cdot \left( \frac{\partial f_{B_0}}{\partial \mathbf{F}} + \mathbf{H} : \left( \omega_m^p \frac{\partial \mathbf{P}}{\partial \mathbf{F}} + (1 - \omega_m^p) \frac{\partial \boldsymbol{\sigma}^f}{\partial \mathbf{F}} \right) \right. \\ & \quad \left. - \eta^p \omega_m^p \frac{\partial \|\boldsymbol{\tau}_{\text{dev}}\|}{\partial \mathbf{F}} + \boldsymbol{\pi} : \omega_m^p \frac{\partial}{\partial \mathbf{F}} \frac{\boldsymbol{\tau}_{\text{dev}}}{\|\boldsymbol{\tau}_{\text{dev}}\|} \right) = \mathbf{0} \text{ in } B_0 \\ & \frac{\partial f_{\partial B_0^N}}{\partial \mathbf{u}} + \left( \frac{\partial f_{B_0}}{\partial \mathbf{F}} + \mathbf{H} : \left( \omega_m^p \frac{\partial \mathbf{P}}{\partial \mathbf{F}} + (1 - \omega_m^p) \frac{\partial \boldsymbol{\sigma}^f}{\partial \mathbf{F}} \right) \right. \\ & \quad \left. - \eta^p \omega_m^p \frac{\partial \|\boldsymbol{\tau}_{\text{dev}}\|}{\partial \mathbf{F}} + \boldsymbol{\pi} : \omega_m^p \frac{\partial}{\partial \mathbf{F}} \frac{\boldsymbol{\tau}_{\text{dev}}}{\|\boldsymbol{\tau}_{\text{dev}}\|} \right) \cdot \mathbf{N} = \mathbf{0} \text{ on } \partial B_0^N \\ & \frac{\partial f_{\partial B_0^D}}{\partial \mathbf{T}} - \boldsymbol{\omega} = \mathbf{0} \text{ on } \partial B_0^D \\ & \frac{\partial f_{B_0}}{\partial \gamma^p} + \mathbf{H} : \omega_m^p \frac{\partial \mathbf{P}}{\partial \gamma^p} - \eta^p \omega_m^p \left( \frac{\partial \|\boldsymbol{\tau}_{\text{dev}}\|}{\partial \gamma^p} - \sqrt{\frac{2}{3}} \left( \frac{\partial R}{\partial \gamma^p} (y_0 + r^p) + R \frac{\partial r^p}{\partial \gamma^p} \right) \right) \\ & \quad + \boldsymbol{\pi} : \omega_m^p \frac{\partial}{\partial \gamma^p} \frac{\boldsymbol{\tau}_{\text{dev}}}{\|\boldsymbol{\tau}_{\text{dev}}\|} - \omega_m^p p_p \bar{\beta} \frac{\partial \alpha}{\partial \gamma^p} = 0 \text{ in } B_0 \\ & \frac{\partial f_{B_0}}{\partial \mathbf{n}} + \mathbf{H} : \omega_m^p \frac{\partial \mathbf{P}}{\partial \mathbf{n}} - \eta^p \omega_m^p \frac{\partial \|\boldsymbol{\tau}_{\text{dev}}\|}{\partial \mathbf{n}} - \boldsymbol{\pi} : \omega_m^p \left( \mathbf{1} \otimes \mathbf{1} - \frac{\partial}{\partial \mathbf{n}} \frac{\boldsymbol{\tau}_{\text{dev}}}{\|\boldsymbol{\tau}_{\text{dev}}\|} \right) = \mathbf{0} \text{ in } B_0 \\ & \frac{\partial f_{B_0}}{\partial \bar{\alpha}} - \nabla \cdot \left( \frac{\partial f_{B_0}}{\partial \nabla \bar{\alpha}} + \eta^p \omega_m^p R \sqrt{\frac{2}{3}} \frac{\partial r^p}{\partial \bar{\alpha}} + \omega_m^p (p_p \bar{\beta} - q_p \nabla^2 \bar{\beta}) \right) = 0 \text{ in } B_0 \\ & \frac{\partial f_{\partial B_0^N}}{\partial \bar{\alpha}} + \frac{\partial f_{B_0}}{\partial \nabla \bar{\alpha}} \cdot \mathbf{N} + \omega_m^p q_p \nabla \bar{\beta} \cdot \mathbf{N} = 0 \text{ on } \partial B_0^N \\ & \frac{\partial f_{\partial B_0^D}}{\partial \bar{\alpha}} - \boldsymbol{\omega} \cdot \frac{\partial \mathbf{T}}{\partial \bar{\alpha}} + \frac{\partial f_{B_0}}{\partial \nabla \bar{\alpha}} \cdot \mathbf{N} + \omega_m^p q_p \nabla \bar{\beta} \cdot \mathbf{N} = 0 \text{ on } \partial B_0^D \end{aligned} \right\} \forall t. \tag{28}$$

2.5. Sensitivity

Reflecting the above formulation in Section 2.4, the first variation of the Lagrangian  $\tilde{\mathcal{F}}$  in Eq. (22) is simplified as

$$\delta\tilde{\mathcal{F}} = \left( \sum_{i=1}^m \delta\omega_i \tilde{\mathcal{F}} \right) = \delta\omega_1 \tilde{\mathcal{F}} + \delta\omega_2 \tilde{\mathcal{F}} + \dots + \delta\omega_{m-1} \tilde{\mathcal{F}} + \delta\omega_m \tilde{\mathcal{F}}, \quad (29)$$

where

for  $i = 1, 2, \dots, m - 1$

$$\begin{aligned} \delta\omega_i \tilde{\mathcal{F}} = & \int_t \left[ \int_{D_0} \frac{\partial f_{B_0}}{\partial \omega_i} \delta\omega_i dV + \int_{\partial D_0^N} \frac{\partial f_{\partial B_0^N}}{\partial \omega_i} \delta\omega_i dA + \int_{\partial D_0^D} \frac{\partial f_{\partial B_0^D}}{\partial \omega_i} \delta\omega_i dA \right. \\ & + \int_{D_0} \mathbf{H} : \omega_m^p \frac{\partial \mathbf{P}}{\partial \omega_i} \delta\omega_i dV - \int_{D_0} \mathbf{w} \cdot \omega_m^p \frac{\partial \mathbf{B}}{\partial \omega_i} \delta\omega_i dV \\ & - \int_{\partial D_0^N} \mathbf{w} \cdot \frac{\partial \tilde{\mathbf{T}}}{\partial \omega_i} \delta\omega_i dA - \int_{\partial D_0^D} \mathbf{w} \cdot \omega_m^p \frac{\partial \mathbf{P}}{\partial \omega_i} \cdot \mathbf{N} \delta\omega_i dA \\ & - \int_{D_0} \eta^p \omega_m^p \left( \frac{\partial \|\boldsymbol{\tau}_{\text{dev}}\|}{\partial \omega_i} - \sqrt{\frac{2}{3}} \left( \frac{\partial R}{\partial \omega_i} (y_0 + r^p) + R \left( \frac{\partial y_0}{\partial \omega_i} + \frac{\partial r^p}{\partial \omega_i} \right) \right) \right) \delta\omega_i dV \\ & \left. + \int_{D_0} \omega_m^p \left( \frac{\partial p_p}{\partial \omega_i} \bar{\beta} (\bar{\alpha} - \alpha) + \frac{\partial q_p}{\partial \omega_i} \nabla \bar{\beta} \cdot \nabla \bar{\alpha} \right) \delta\omega_i dV \right] dt - \sum_{l=1}^i (\theta_l - \theta_{l+1}) \int_{D_0} \frac{1}{\omega_i} \prod_{k=1}^m \omega_k \delta\omega_i dV, \end{aligned} \quad (30)$$

for  $i = m$

$$\begin{aligned} \delta\omega_m \tilde{\mathcal{F}} = & \int_t \left[ \int_{D_0} \frac{\partial f_{B_0}}{\partial \omega_m} \delta\omega_m dV + \int_{\partial D_0^N} \frac{\partial f_{\partial B_0^N}}{\partial \omega_m} \delta\omega_m dA + \int_{\partial D_0^D} \frac{\partial f_{\partial B_0^D}}{\partial \omega_m} \delta\omega_m dA \right. \\ & + \int_{D_0} \mathbf{H} : \frac{\partial \omega_m^p}{\partial \omega_m} (\mathbf{P} - \boldsymbol{\sigma}^f) \delta\omega_m dV - \int_{D_0} \mathbf{w} \cdot \frac{\partial \omega_m^p}{\partial \omega_m} \mathbf{B} \delta\omega_m dV \\ & - \int_{\partial D_0^N} \mathbf{w} \cdot \frac{\partial \tilde{\mathbf{T}}}{\partial \omega_m} \delta\omega_m dA - \int_{\partial D_0^D} \mathbf{w} \cdot \frac{\partial \omega_m^p}{\partial \omega_m} (\mathbf{P} - \boldsymbol{\sigma}^f) \cdot \mathbf{N} \delta\omega_m dA \\ & \left. + \int_{D_0} \frac{\partial \omega_m^p}{\partial \omega_m} (p_p \bar{\beta} (\bar{\alpha} - \alpha) + q_p \nabla \bar{\beta} \cdot \nabla \bar{\alpha}) \delta\omega_m dV \right] dt - \sum_{l=1}^m (\theta_l - \theta_{l+1}) \int_{D_0} \frac{1}{\omega_m} \prod_{k=1}^m \omega_k \delta\omega_m dV. \end{aligned}$$

Here, the manipulation in Appendix A.3 has been performed for the volume constraints. It is noted that the overlapping boundaries, i.e.,  $\partial D_0^N = \partial B_0^N \cap \partial D_0$  and  $\partial D_0^D = \partial B_0^D \cap \partial D_0$ , are allowed in Eq. (30) for ensuring generality. Accordingly, the sensitivity for the multi-material topology optimization yields

$$\begin{aligned} s_{D_0,i} = & \bar{s}_{D_0,i} - \sum_{l=1}^i (\theta_l - \theta_{l+1}) \frac{1}{\omega_i} \prod_{k=1}^m \omega_k \text{ in } D_0 \\ \text{with } \bar{s}_{D_0,i} = & \begin{cases} \int_t \left[ \frac{\partial f_{B_0}}{\partial \omega_i} + \omega_m^p \left( \mathbf{H} : \frac{\partial \mathbf{P}}{\partial \omega_i} - \mathbf{w} \cdot \frac{\partial \mathbf{B}}{\partial \omega_i} \right. \right. \\ \quad \left. \left. - \eta^p \left( \frac{\partial \|\boldsymbol{\tau}_{\text{dev}}\|}{\partial \omega_i} - \sqrt{\frac{2}{3}} \left( \frac{\partial R}{\partial \omega_i} (y_0 + r^p) + R \left( \frac{\partial y_0}{\partial \omega_i} + \frac{\partial r^p}{\partial \omega_i} \right) \right) \right) \right. \right. \\ \quad \left. \left. + \frac{\partial p_p}{\partial \omega_i} \bar{\beta} (\bar{\alpha} - \alpha) + \frac{\partial q_p}{\partial \omega_i} \nabla \bar{\beta} \cdot \nabla \bar{\alpha} \right) \right] dt \text{ for } i = 1, 2, \dots, m - 1 \\ \int_t \left[ \frac{\partial f_{B_0}}{\partial \omega_m} + \frac{\partial \omega_m^p}{\partial \omega_m} \left( \mathbf{H} : (\mathbf{P} - \boldsymbol{\sigma}^f) - \mathbf{w} \cdot \mathbf{B} + p_p \bar{\beta} (\bar{\alpha} - \alpha) + q_p \nabla \bar{\beta} \cdot \nabla \bar{\alpha} \right) \right] dt \text{ for } i = m, \end{cases} \quad (31) \\ s_{\partial D_0^N,i} = & \int_t \left[ \frac{\partial f_{\partial B_0^N}}{\partial \omega_i} - \mathbf{w} \cdot \frac{\partial \tilde{\mathbf{T}}}{\partial \omega_i} \right] dt \text{ on } \partial D_0^N, \\ s_{\partial D_0^D,i} = & \begin{cases} \int_t \left[ \frac{\partial f_{\partial B_0^D}}{\partial \omega_i} - \omega_m^p \mathbf{w} \cdot \frac{\partial \mathbf{P}}{\partial \omega_i} \cdot \mathbf{N} \right] dt \text{ for } i = 1, 2, \dots, m - 1 \\ \int_t \left[ \frac{\partial f_{\partial B_0^D}}{\partial \omega_m} - \frac{\partial \omega_m^p}{\partial \omega_m} \mathbf{w} \cdot (\mathbf{P} - \boldsymbol{\sigma}^f) \cdot \mathbf{N} \right] dt \text{ for } i = m \end{cases} \text{ on } \partial D_0^D. \end{aligned}$$

Additionally, the SIMP-based interpolation function in Eq. (9) can be divided as

$$\text{Eq. (9)} = \underbrace{\left( \prod_{j=1}^{m-1} \omega_j^p \right) \bullet_1}_{\text{Term A}} + \underbrace{\sum_{j=2}^{m-1} \left( \prod_{k=j}^{m-1} \omega_k^p \right) (1 - \omega_{j-1}^p) \bullet_j}_{\text{Term B}} + \underbrace{(1 - \omega_{m-1}^p) \bullet_m}_{\text{Term C}} \quad (32)$$

and the partial derivatives of these three terms with respect to all design variables are calculated as, respectively,

$$\frac{\partial(\text{Term A})}{\partial \omega_i} = \frac{\partial \omega_i^p}{\partial \omega_i} \left( \prod_{j=1, j \neq i}^{m-1} \omega_j^p \right) \bullet_1, \quad (33)$$

$$\frac{\partial(\text{Term B})}{\partial \omega_i} = \underbrace{\sum_{j=2}^{m-1} \left( \frac{\partial}{\partial \omega_i} \left( \prod_{k=j}^{m-1} \omega_k^p \right) \right) (1 - \omega_{j-1}^p) \bullet_j}_{\partial_{\omega_i}(\text{Term B1})} + \underbrace{\sum_{j=2}^{m-1} \left( \prod_{k=j}^{m-1} \omega_k^p \right) \left( \frac{\partial}{\partial \omega_i} (1 - \omega_{j-1}^p) \right) \bullet_j}_{\partial_{\omega_i}(\text{Term B2})}, \quad (34)$$

$$\frac{\partial(\text{Term B1})}{\partial \omega_i} = \sum_{j=2}^i \frac{\partial \omega_i^p}{\partial \omega_i} \left( \prod_{k=j, k \neq i}^{m-1} \omega_k^p \right) (1 - \omega_{j-1}^p) \bullet_j \quad \text{for } i \geq 2, \quad (34)$$

$$\frac{\partial(\text{Term B2})}{\partial \omega_i} = - \left( \prod_{k=i+1}^{m-1} \omega_k^p \right) \frac{\partial \omega_i^p}{\partial \omega_i} \bullet_{i+1} \quad \text{for } i = j - 1,$$

and

$$\frac{\partial(\text{Term C})}{\partial \omega_i} = - \frac{\partial \omega_i^p}{\partial \omega_i} \bullet_{i+1} \quad \text{for } i = m - 1. \quad (35)$$

## 2.6. Reaction–diffusion equation-based design variable update method

Suppose that the sensitivity in Eq. (31) is proportional to the time evolution of design variables. Then, following Otomori et al. [42], we employ the following reaction–diffusion equations for updating  $m$  design variables:

$$\left. \begin{aligned} &\text{for } i = 1, 2, \dots, m - 1, m \\ &\left. \begin{aligned} \dot{\omega}_i &= C_{D_0, i^s} D_{0, i} + l_d^2 \nabla^2 \omega_i \text{ in } D_0 \\ l_d^2 \nabla \omega_i \cdot \mathbf{N} &= C_{\partial D_0^N, i^s} \partial D_0^N \bullet_i \text{ on } \partial D_0^N \\ l_d^2 \nabla \omega_i \cdot \mathbf{N} &= C_{\partial D_0^D, i^s} \partial D_0^D \bullet_i \text{ on } \partial D_0^D \end{aligned} \right\} \forall i, \end{aligned} \quad (36)$$

where  $l_d^2$  is the diffusion coefficient, and  $C_{D_0, i^s}$ ,  $C_{\partial D_0^N, i^s}$ , and  $C_{\partial D_0^D, i^s}$  are normalization factors.

## 3. Discretization

This section is devoted to the discretization of the primal problem, adjoint problem, and design variable update, which follows the standard finite element (FE) context. In the end, the overall optimization algorithm is explained. The linear finite element is employed for spatial discretization, and the backward difference method is applied for temporal discretization.

### 3.1. Discretization of the primal problem

Conventionally, the displacement vector  $\mathbf{u}$  and nonlocal plastic hardening variable  $\bar{\alpha}$  are defined as nodal variables, whereas the plastic multiplier  $\gamma^p$  and flow tensor  $\mathbf{n}$  are treated as internal state variables. Following this setting, the weak forms of the displacement and micromorphic plastic fields in Eq. (12)<sub>1,2,4</sub> yield

$$\begin{aligned} &\int_{B_0} \left( (\omega_m^p \mathbf{P} + (1 - \omega_m^p) \boldsymbol{\sigma}^f) : \frac{\partial \delta \mathbf{u}}{\partial \mathbf{X}} - \omega_m^p \mathbf{B} \cdot \delta \mathbf{u} \right) dV - \int_{\partial B_0^N} \bar{\mathbf{T}} \cdot \delta \mathbf{u} dA = 0 \quad \forall \delta \mathbf{u}, \\ &\int_{B_0} \left( \omega_m^p p_p (\bar{\alpha} - \alpha) \delta \bar{\alpha} + \omega_m^p q_p \frac{\partial \bar{\alpha}}{\partial \mathbf{X}} \cdot \frac{\partial \delta \bar{\alpha}}{\partial \mathbf{X}} \right) dV = 0 \quad \forall \delta \bar{\alpha}. \end{aligned} \quad (37)$$

Considering the standard finite element approximation using the shape function  $N^I$ , the finite element discretization of the left-hand side of Eq. (37) and its linearization lead to the following node-level global residual vectors and tangent matrices:

$$\begin{aligned}
 \mathcal{R}_{u_i,n}^I &= -\mathbf{A} \sum_{e=1}^{n_{\text{ele}}} \left\{ \int_{B_{0,e}} \left( (\omega_m^{hp} P_{ia,n}^h + (1 - \omega_m^{hp}) \sigma_{ia,n}^{fh}) \frac{\partial N^I}{\partial X_a} - \omega_m^{hp} B_i^h N^I \right) dV - \int_{\partial B_{0,e}^N} \bar{T}_{i,n}^h N^I dA \right\}, \\
 \mathcal{R}_{\bar{\alpha},n}^I &= -\mathbf{A} \sum_{e=1}^{n_{\text{ele}}} \left\{ \int_{B_{0,e}} \left( \omega_m^{hp} p_p^h (\bar{\alpha}_n^h - \alpha_n^h) N^I + \omega_m^{hp} q_p^h \frac{\partial \bar{\alpha}_n^h}{\partial X_a} \frac{\partial N^I}{\partial X_a} \right) dV \right\}, \\
 \mathcal{K}_{u_i u_j, n}^{IJ} &= \mathbf{A} \sum_{e=1}^{n_{\text{ele}}} \int_{B_{0,e}} \frac{\partial N^I}{\partial X_a} \left( \omega_m^{hp} \left( \frac{\partial P_{ia,n}^h}{\partial F_{jb}} + \frac{\partial P_{ia,n}^h}{\partial \gamma^p} \frac{\partial \gamma_n^{ph}}{\partial F_{jb}} + \frac{\partial P_{ia,n}^h}{\partial n_{cd}} \frac{\partial n_{cd,n}^h}{\partial F_{jb}} \right) + (1 - \omega_m^{hp}) \frac{\partial \sigma_{ia,n}^{fh}}{\partial F_{jb}} \right) \frac{\partial N^J}{\partial X_b} dV, \\
 \mathcal{K}_{\bar{\alpha} \bar{\alpha}, n}^{IJ} &= \mathbf{A} \sum_{e=1}^{n_{\text{ele}}} \int_{B_{0,e}} \frac{\partial N^I}{\partial X_a} \omega_m^{hp} \left( \frac{\partial P_{ia,n}^h}{\partial \gamma^p} \frac{\partial \gamma_n^{ph}}{\partial \bar{\alpha}} + \frac{\partial P_{ia,n}^h}{\partial n_{cd}} \frac{\partial n_{cd,n}^h}{\partial \bar{\alpha}} \right) N^J dV, \\
 \mathcal{K}_{\bar{\alpha} u_j, n}^{IJ} &= \mathbf{A} \sum_{e=1}^{n_{\text{ele}}} \int_{B_{0,e}} N^I \left( -\omega_m^{hp} p_p^h \frac{\partial \alpha_n^h}{\partial \gamma^p} \frac{\partial \gamma_n^{ph}}{\partial F_{jb}} \right) \frac{\partial N^J}{\partial X_b} dV, \\
 \mathcal{K}_{\bar{\alpha} \bar{\alpha}, n}^{IJ} &= \mathbf{A} \sum_{e=1}^{n_{\text{ele}}} \int_{B_{0,e}} \left( \omega_m^{hp} p_p^h N^I \left( 1 - \frac{\partial \alpha_n^h}{\partial \gamma^p} \frac{\partial \gamma_n^{ph}}{\partial \bar{\alpha}} \right) N^J + \omega_m^{hp} q_p^h \frac{\partial N^I}{\partial X_a} \frac{\partial N^J}{\partial X_a} \right) dV,
 \end{aligned} \tag{38}$$

where  $\mathbf{A}$  is the finite element assembling operator,  $n_{\text{ele}}$  is the total number of finite elements, and  $\bullet^h$  denotes the approximation of  $\bullet$ . Here, the subscripts for scalars, vectors, and tensors are written in the following order: those describing variables, those corresponding to spatial dimensions, and those related to time steps. Also, the time interval is denoted by  $\Delta t_n = t_n - t_{n-1}$ , and the quantity at the time step  $t_n$  and its increment are denoted by  $\bullet_n$  and  $\Delta \bullet_n$ , respectively.

On the other hand, to solve Eq. (12)<sub>2,3</sub> for the plastic multiplier  $\gamma^p$  and flow tensor  $\mathbf{n}$ , the integration point-level local residual vectors and tangent matrices are written as

$$\begin{aligned}
 \mathcal{R}_{\gamma^p, n}^g &= - \left( \|\boldsymbol{\tau}_{\text{dev},n}^h\| - \sqrt{\frac{2}{3}} R_n^h (y_0^h + t_n^{ph}) \right), \\
 \mathcal{R}_{\mathbf{n}_{ij}, n}^g &= - \left( \mathbf{n}_{ij,n}^h - \frac{\boldsymbol{\tau}_{\text{dev},ij,n}^h}{\|\boldsymbol{\tau}_{\text{dev},n}^h\|} \right), \\
 \mathcal{K}_{\gamma^p \gamma^p, n}^g &= \frac{\partial \|\boldsymbol{\tau}_{\text{dev},n}^h\|}{\partial \gamma^p} - \sqrt{\frac{2}{3}} \left( \frac{\partial R_n^h}{\partial \gamma^p} (y_0^h + t_n^{ph}) + R_n^h \frac{\partial t_n^{ph}}{\partial \gamma^p} \right), \quad \mathcal{K}_{\gamma^p \mathbf{n}_{kl}, n}^g = \frac{\partial \|\boldsymbol{\tau}_{\text{dev},n}^h\|}{\partial \mathbf{n}_{kl,n}}, \\
 \mathcal{K}_{\mathbf{n}_{ij} \gamma^p, n}^g &= - \frac{\partial}{\partial \gamma^p} \frac{\boldsymbol{\tau}_{\text{dev},ij,n}^h}{\|\boldsymbol{\tau}_{\text{dev},n}^h\|}, \quad \mathcal{K}_{\mathbf{n}_{ij} \mathbf{n}_{kl}, n}^g = \delta_{ik} \delta_{jl} - \frac{\partial}{\partial \mathbf{n}_{kl}} \frac{\boldsymbol{\tau}_{\text{dev},ij,n}^h}{\|\boldsymbol{\tau}_{\text{dev},n}^h\|}.
 \end{aligned} \tag{39}$$

Some components derived in the above discretization are detailed in Appendix B.1.

It is noted that the subloading surface model behaves differently from the conventional plastic model, as summarized in Fig. 3. As shown in Fig. 3(a), the deformation state of the subloading surface model consists of four parts. Specifically, recalling the yield criteria in Eq. (5), the four parts are distinguished by the following rules:

$$\begin{aligned}
 \text{Part A} & \quad \left\{ \begin{array}{l} \Phi_{\text{sub},n}^{\text{p,tr}} < 0 \text{ and } \Phi_{\text{ela},n}^{\text{p,tr}} < 0, 0 \leq R_n \leq R^e, \\ \text{elastic loading} \quad R_n = \sqrt{\frac{3}{2}} \frac{\|\boldsymbol{\tau}_{\text{dev},n}\|}{y_0}, \end{array} \right. \\
 \text{Part B} & \quad \left\{ \begin{array}{l} \Phi_{\text{sub},n}^{\text{p,tr}} > 0 \text{ and } \Phi_{\text{ela},n}^{\text{p,tr}} > 0, R^e \leq R_n \leq 1, \\ \text{plastic loading} \quad R_n = R^e + \frac{2}{\pi} (1 - R^e) \arccos \left( \cos \left( \frac{\pi}{2} \frac{\langle R_{n-1} - R^e \rangle}{1 - R^e} \right) \exp \left( -\frac{\pi}{2} \frac{R^p}{1 - R^e} \gamma_n^p \Delta t_n \right) \right), \end{array} \right. \\
 \text{Part C} & \quad \left\{ \begin{array}{l} \Phi_{\text{sub},n}^{\text{p,tr}} < 0 \text{ or } \Phi_{\text{ela},n}^{\text{p,tr}} < 0, 0 \leq R_n \leq 1, \\ \text{elastic unloading} \quad R_n = \sqrt{\frac{3}{2}} \frac{\|\boldsymbol{\tau}_{\text{dev},n}\|}{y_0 + t_n^p}, \end{array} \right. \\
 \text{Part D} & \quad \left\{ \begin{array}{l} \Phi_{\text{sub},n}^{\text{p,tr}} > 0 \text{ and } \Phi_{\text{ela},n}^{\text{p,tr}} > 0, R^e \leq R_n \leq 1, \\ \text{plastic reloading} \quad R_n = R^e + \frac{2}{\pi} (1 - R^e) \arccos \left( \cos \left( \frac{\pi}{2} \frac{\langle R_{n-1} - R^e \rangle}{1 - R^e} \right) \exp \left( -\frac{\pi}{2} \frac{R^p}{1 - R^e} \gamma_n^p \Delta t_n \right) \right), \end{array} \right.
 \end{aligned} \tag{40}$$

where the superscript “tr” denotes the trial stress state at each Newton–Raphson iteration. Particularly, enjoying the evolution of the normal-yield ratio  $R$ , the deformation process gradually shifts from the purely elastic deformation to the plastic deformation that exhibits hardening behavior; see the blue-colored line in Fig. 3(a). Here, the slope of the stress–strain curve is a continuous function after the initial plastic yield. Also, unlike the conventional plastic model, the plastic deformation evolves in the cyclic loadings even

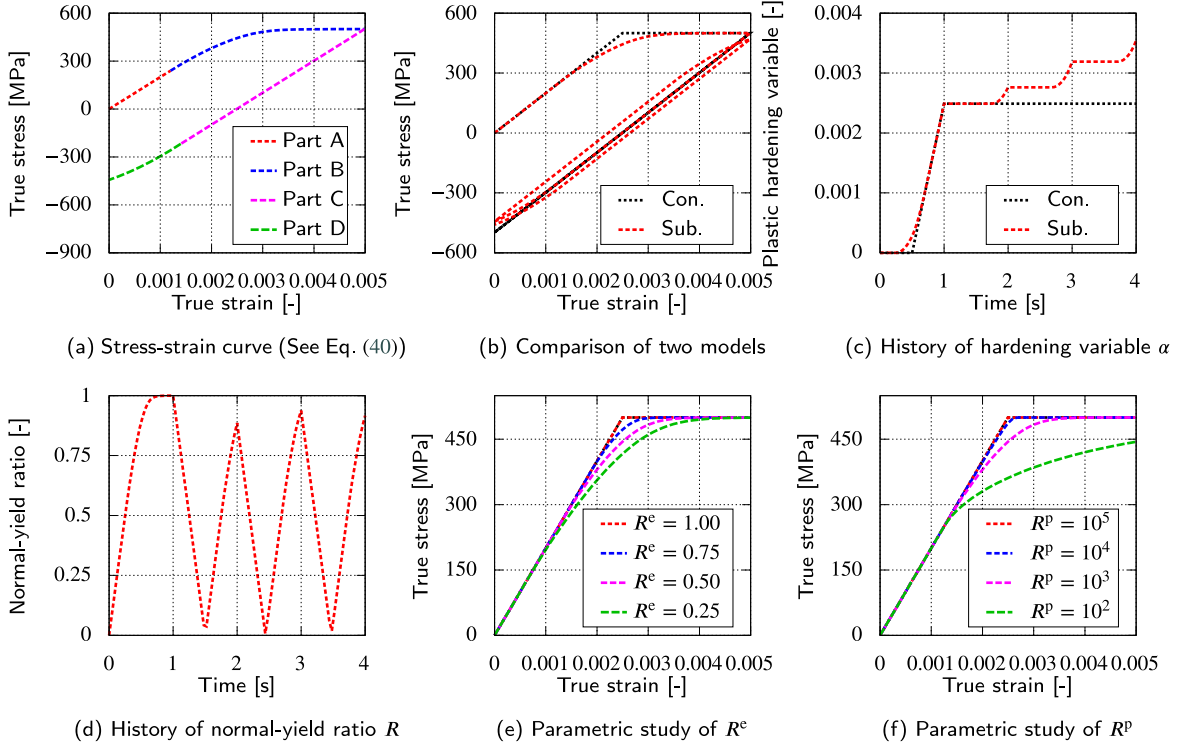


Fig. 3. Detailed elastoplastic responses of conventional plastic model (Con.) and subloading surface model (Sub.).

if the kinematic hardening is not introduced; see Figs. 3(b) and (c). This is because the normal-yield ratio increases and decreases along with plastic loading and elastic unloading, respectively; see Fig. 3(d).

In addition, Figs. 3(e) and (f) show the stress-strain relationships of changing the values of the normal-yield threshold  $R^e$  and normal-yield saturation parameter  $R^p$ . As can be seen from Fig. 3(e),  $R^e$  determines the range of the transition of deformation states, and a larger value of  $R^e$  shortens the range, making it recover to the conventional plastic model. Also, from Fig. 3(f), one finds that  $R^p$  changes the saturation behavior of the transition of deformation states, and giving a larger value of  $R^p$  recovers to the conventional plastic model. Notably, by introducing the normal-yield ratio  $R$ , the stress-strain relationship around the original plastic yield point becomes smooth, which is beneficial for a stable elastoplastic topology optimization process. Also, the case with  $R^e = 1.00$  or  $R^p \rightarrow \infty$  corresponds to the response of the conventional plastic model. The detailed investigations are provided in Section 4.1.

### 3.2. Discretization of the adjoint problem

Similar to the primal problem, the adjoint displacement vector  $\mathbf{w}$  and adjoint nonlocal plastic hardening variable  $\bar{\beta}$  are defined as nodal variables, whereas the adjoint plastic multiplier  $\eta^p$  and adjoint flow tensor  $\boldsymbol{\pi}$  are treated as internal state variables. Then, the weak forms for the adjoint displacement and adjoint micromorphic plastic fields in Eq. (28)<sub>1-3,6-8</sub> become

$$\begin{aligned}
 & \int_{B_0} \left( \frac{\partial f_{B_0}}{\partial \mathbf{F}} + \mathbf{H} : \left( \omega_m^p \frac{\partial \mathbf{P}}{\partial \mathbf{F}} + (1 - \omega_m^p) \frac{\partial \boldsymbol{\sigma}^f}{\partial \mathbf{F}} \right) - \eta^p \omega_m^p \frac{\partial \|\boldsymbol{\tau}_{\text{dev}}\|}{\partial \mathbf{F}} + \boldsymbol{\pi} : \omega_m^p \frac{\partial}{\partial \mathbf{F}} \frac{\boldsymbol{\tau}_{\text{dev}}}{\|\boldsymbol{\tau}_{\text{dev}}\|} \right) : \frac{\partial \delta \mathbf{w}}{\partial \mathbf{X}} dV \\
 & + \int_{B_0} \frac{\partial f_{B_0}}{\partial \mathbf{u}} \cdot \delta \mathbf{w} dV + \int_{\partial B_0^N} \frac{\partial f_{\partial B_0^N}}{\partial \mathbf{u}} \cdot \delta \mathbf{w} dA = 0 \quad \forall \delta \mathbf{w}, \\
 & \int_{B_0} \left( \frac{\partial f_{B_0}}{\partial \bar{\alpha}} \delta \bar{\beta} + \frac{\partial f_{B_0}}{\partial \nabla \bar{\alpha}} \cdot \frac{\partial \delta \bar{\beta}}{\partial \mathbf{X}} + \eta^p \omega_m^p R \sqrt{\frac{2}{3}} \frac{\partial r^p}{\partial \bar{\alpha}} \delta \bar{\beta} + \omega_m^p \left( p_p \bar{\beta} \delta \bar{\beta} + q_p \frac{\partial \bar{\beta}}{\partial \mathbf{X}} \cdot \frac{\partial \delta \bar{\beta}}{\partial \mathbf{X}} \right) \right) dV \\
 & + \int_{\partial B_0^N} \frac{\partial f_{\partial B_0^N}}{\partial \bar{\alpha}} \delta \bar{\beta} dA + \int_{\partial B_0^D} \left( \frac{\partial f_{\partial B_0^D}}{\partial \bar{\alpha}} - \mathbf{w} \cdot \frac{\partial \boldsymbol{\Gamma}}{\partial \bar{\alpha}} \right) \delta \bar{\beta} dA = 0 \quad \forall \delta \bar{\beta}.
 \end{aligned} \tag{41}$$

Using the same shape function  $N^I$ , the node-level global residual vectors and tangent matrices of the adjoint problem are expressed as

$$\begin{aligned}
 \mathcal{R}_{w_i,n}^I &= -\mathbf{A}_{e=1}^{n_{ele}} \left[ \int_{B_{0,e}} \left( \frac{\partial f_{B_{0,n}}^h}{\partial F_{ia}} + H_{cd,n}^h \left( \omega_m^{hp} \frac{\partial P_{cd,n}^h}{\partial F_{ia}} + (1 - \omega_m^{hp}) \frac{\partial \sigma_{cd,n}^{fh}}{\partial F_{ia}} \right) \right. \right. \\
 &\quad \left. \left. - \eta_n^{ph} \omega_m^{hp} \frac{\partial \|\tau_{dev,n}^h\|}{\partial F_{ia}} + \pi_{cd,n}^h \omega_m^{hp} \frac{\partial}{\partial F_{ia}} \frac{\tau_{dev,cd,n}^h}{\|\tau_{dev,n}^h\|} \right) \frac{\partial N^I}{\partial X_a} dV \right. \\
 &\quad \left. + \int_{B_{0,e}} \frac{\partial f_{B_{0,n}}^h}{\partial u_i} N^I dV + \int_{\partial B_{0,e}^N} \frac{\partial f_{B_{0,n}}^h}{\partial u_i} N^I dA \right], \\
 \mathcal{R}_{\beta,n}^I &= -\mathbf{A}_{e=1}^{n_{ele}} \left[ \int_{B_{0,e}} \left( \frac{\partial f_{B_{0,n}}^h}{\partial \bar{\alpha}} N^I + \frac{\partial f_{B_{0,n}}^h}{\partial \nabla \bar{\alpha}} \frac{\partial N^I}{\partial X_a} \right. \right. \\
 &\quad \left. \left. + \eta_n^{ph} \omega_m^{hp} R_n^h \sqrt{\frac{2}{3}} \frac{\partial r_n^{ph}}{\partial \bar{\alpha}} N^I + \omega_m^{hp} \left( p_p^h \bar{\beta}^h N^I + q_p^h \frac{\partial \bar{\beta}^h}{\partial X_a} \frac{\partial N^I}{\partial X_a} \right) \right) dV \right. \\
 &\quad \left. + \int_{\partial B_{0,e}^N} \frac{\partial f_{B_{0,n}}^h}{\partial \bar{\alpha}} N^I dA + \int_{\partial B_{0,e}^D} \left( \frac{\partial f_{B_{0,n}}^h}{\partial \bar{\alpha}} - u_{a,n}^h \frac{\partial T_{a,n}^h}{\partial \bar{\alpha}} \right) N^I dA \right], \\
 \mathcal{K}_{w_i w_j,n}^{IJ} &= \mathbf{A}_{e=1}^{n_{ele}} \int_{B_{0,e}} \frac{\partial N^I}{\partial X_a} \left( \omega_m^{hp} \frac{\partial P_{jb,n}^h}{\partial F_{ia}} + (1 - \omega_m^{hp}) \frac{\partial \sigma_{jb,n}^{fh}}{\partial F_{ia}} \right. \\
 &\quad \left. - \frac{\partial \eta_n^{ph}}{\partial H_{jb}} \omega_m^{hp} \frac{\partial \|\tau_{dev,n}^h\|}{\partial F_{ia}} + \frac{\partial \pi_{cd,n}^h}{\partial H_{jb}} \omega_m^{hp} \frac{\partial}{\partial F_{ia}} \frac{\tau_{dev,cd,n}^h}{\|\tau_{dev,n}^h\|} \right) \frac{\partial N^J}{\partial X_b} dV, \\
 \mathcal{K}_{w_i \beta,n}^{IJ} &= \mathbf{A}_{e=1}^{n_{ele}} \int_{B_{0,e}} \frac{\partial N^I}{\partial X_a} \left( -\frac{\partial \eta_n^{ph}}{\partial \bar{\beta}} \omega_m^{hp} \frac{\partial \|\tau_{dev,n}^h\|}{\partial F_{ia}} + \frac{\partial \pi_{cd,n}^h}{\partial \bar{\beta}} \omega_m^{hp} \frac{\partial}{\partial F_{ia}} \frac{\tau_{dev,cd,n}^h}{\|\tau_{dev,n}^h\|} \right) N^J dV, \\
 \mathcal{K}_{\beta w_j,n}^{IJ} &= \mathbf{A}_{e=1}^{n_{ele}} \int_{B_{0,e}} N^I \left( \frac{\partial \eta_n^{ph}}{\partial H_{jb}} \omega_m^{hp} R_n^h \sqrt{\frac{2}{3}} \frac{\partial r_n^{ph}}{\partial \bar{\alpha}} \right) \frac{\partial N^J}{\partial X_b} dV, \\
 \mathcal{K}_{\beta \beta,n}^{IJ} &= \mathbf{A}_{e=1}^{n_{ele}} \int_{B_{0,e}} \left( N^I \frac{\partial \eta_n^{ph}}{\partial \bar{\beta}} \omega_m^{hp} R_n^h \sqrt{\frac{2}{3}} \frac{\partial r_n^{ph}}{\partial \bar{\alpha}} N^J + \omega_m^{hp} \left( p_p^h N^I N^J + q_p^h \frac{\partial N^I}{\partial X_a} \frac{\partial N^J}{\partial X_a} \right) \right) dV.
 \end{aligned} \tag{42}$$

Meanwhile, to solve Eq. (28)<sub>4,5</sub> for the adjoint plastic multiplier  $\eta^p$  and adjoint flow tensor  $\pi$ , the following integration point-level local residual vectors and tangent matrices are written as

$$\begin{aligned}
 \mathcal{R}_{\eta^p,n}^g &= - \left( \frac{\partial f_{B_{0,n}}^h}{\partial \gamma^p} + H_{ab,n}^h \omega_m^{hp} \frac{\partial P_{ab,n}^h}{\partial \gamma^p} - \eta_n^{ph} \omega_m^{hp} \left( \frac{\partial \|\tau_{dev,n}^h\|}{\partial \gamma^p} - \sqrt{\frac{2}{3}} \left( \frac{\partial R_n^h}{\partial \gamma^p} (y_0^h + r_n^{ph}) + R_n^h \frac{\partial r_n^{ph}}{\partial \gamma^p} \right) \right) \right. \\
 &\quad \left. + \pi_{ab,n}^h \omega_m^{hp} \frac{\partial}{\partial \gamma^p} \frac{\tau_{dev,ab,n}^h}{\|\tau_{dev,n}^h\|} - \omega_m^{hp} p_p^h \bar{\beta}^h \frac{\partial \alpha_n^h}{\partial \gamma^p} \right), \\
 \mathcal{R}_{\pi_{ij},n}^g &= - \left( \frac{\partial f_{B_{0,n}}^h}{\partial n_{ij}} + H_{ab,n}^h \omega_m^{hp} \frac{\partial P_{ab,n}^h}{\partial n_{ij}} - \eta_n^{ph} \omega_m^{hp} \frac{\partial \|\tau_{dev,n}^h\|}{\partial n_{ij}} - \pi_{ab,n}^h \omega_m^{hp} \left( \delta_{ai} \delta_{bj} - \frac{\partial}{\partial n_{ij}} \frac{\tau_{dev,ab,n}^h}{\|\tau_{dev,n}^h\|} \right) \right), \\
 \mathcal{K}_{\eta^p \eta^p,n}^g &= -\omega_m^{hp} \left( \frac{\partial \|\tau_{dev,n}^h\|}{\partial \gamma^p} - \sqrt{\frac{2}{3}} \left( \frac{\partial R_n^h}{\partial \gamma^p} (y_0^h + r_n^{ph}) + R_n^h \frac{\partial r_n^{ph}}{\partial \gamma^p} \right) \right), \quad \mathcal{K}_{\eta^p \pi_{kl},n}^g = \omega_m^{hp} \frac{\partial}{\partial \gamma^p} \frac{\tau_{dev,kl,n}^h}{\|\tau_{dev,n}^h\|}, \\
 \mathcal{K}_{\pi_{ij} \eta^p,n}^g &= -\omega_m^{hp} \frac{\partial \|\tau_{dev,n}^h\|}{\partial n_{ij}}, \quad \mathcal{K}_{\pi_{ij} \pi_{kl},n}^g = -\omega_m^{hp} \left( \delta_{ki} \delta_{lj} - \frac{\partial}{\partial n_{ij}} \frac{\tau_{dev,kl,n}^h}{\|\tau_{dev,n}^h\|} \right).
 \end{aligned} \tag{43}$$

Some of the detailed components of the above discretization are presented in [Appendix B.2](#).

It is worth mentioning that while the above Eqs. (42) and (43), in the adjoint problem can be straightforwardly solved, these can be rewritten to improve computational efficiency: some derivatives appearing in the above equations need not be computed.

To be specific, since the local adjoint problem is linear,  $\eta_n^p$  and  $\pi_n$  can be directly calculated from Eq. (43)<sub>1,2</sub> as

$$\tilde{\xi}_n = \tilde{W}_n \cdot \underbrace{\mathcal{K}_{\text{local},n}^{\text{adjoint}}}_{\text{Eq. (77)}}^{-1} \text{ with } \tilde{\xi}_n = \begin{bmatrix} \eta_n^{\text{ph}} \\ \pi_{11,n}^h \\ \pi_{22,n}^h \\ \pi_{33,n}^h \\ \pi_{23,n}^h \\ \pi_{13,n}^h \\ \pi_{12,n}^h \end{bmatrix} \text{ and } \tilde{W}_n = - \begin{bmatrix} \frac{\partial f_{B_0,n}^h}{\partial \gamma^p} + H_{ab,n}^h \omega_m^{hp} \frac{\partial P_{ab,n}^h}{\partial \gamma^p} - \omega_m^{hp} p_p^h \tilde{\beta}_n^h \frac{\partial \alpha_n^h}{\partial \gamma^p} \\ \frac{\partial f_{B_0,n}^h}{\partial n_{11}} + H_{ab,n}^h \omega_m^{hp} \frac{\partial P_{ab,n}^h}{\partial n_{11}} \\ \frac{\partial f_{B_0,n}^h}{\partial n_{22}} + H_{ab,n}^h \omega_m^{hp} \frac{\partial P_{ab,n}^h}{\partial n_{22}} \\ \frac{\partial f_{B_0,n}^h}{\partial n_{33}} + H_{ab,n}^h \omega_m^{hp} \frac{\partial P_{ab,n}^h}{\partial n_{33}} \\ \frac{\partial f_{B_0,n}^h}{\partial n_{23}} + 2H_{ab,n}^h \omega_m^{hp} \frac{\partial P_{ab,n}^h}{\partial n_{23}} \\ \frac{\partial f_{B_0,n}^h}{\partial n_{13}} + 2H_{ab,n}^h \omega_m^{hp} \frac{\partial P_{ab,n}^h}{\partial n_{13}} \\ \frac{\partial f_{B_0,n}^h}{\partial n_{12}} + 2H_{ab,n}^h \omega_m^{hp} \frac{\partial P_{ab,n}^h}{\partial n_{12}} \end{bmatrix}. \quad (44)$$

Accordingly, the substitutions of Eqs. (44), (65), and (70) into (42) yield

$$\begin{aligned} \mathcal{R}_{w_i,n}^I &= -\mathbf{A}_{e=1}^{n_{\text{ele}}} \left[ \int_{B_{0,e}} \left( \left( \frac{\partial f_{B_0,n}^h}{\partial F_{ia}} + \frac{\partial f_{B_0,n}^h}{\partial \gamma^p} \frac{\partial \gamma_n^{\text{ph}}}{\partial F_{ia}} + \frac{\partial f_{B_0,n}^h}{\partial n_{ef}} \frac{\partial n_{ef,n}^h}{\partial F_{ia}} \right. \right. \right. \\ &\quad \left. \left. + H_{cd,n}^h \left( \omega_m^{hp} \left( \frac{\partial P_{cd,n}^h}{\partial F_{ia}} + \frac{\partial P_{cd,n}^h}{\partial \gamma^p} \frac{\partial \gamma_n^{\text{ph}}}{\partial F_{ia}} + \frac{\partial P_{cd,n}^h}{\partial n_{ef}} \frac{\partial n_{ef,n}^h}{\partial F_{ia}} \right) + (1 - \omega_m^{hp}) \frac{\partial \sigma_{cd,n}^{\text{fh}}}{\partial F_{ia}} \right) \right. \right. \\ &\quad \left. \left. - \omega_m^{hp} p_p^h \tilde{\beta}_n^h \frac{\partial \alpha_n^h}{\partial \gamma^p} \frac{\partial \gamma_n^{\text{ph}}}{\partial F_{ia}} \right) \frac{\partial N^I}{\partial X_a} \right] dV + \int_{B_{0,e}} \frac{\partial f_{B_0,n}^h}{\partial u_i} N^I dV + \int_{\partial B_{0,e}^N} \frac{\partial f_{\partial B_{0,e}^N,n}^h}{\partial u_i} N^I dA, \\ \mathcal{R}_{\tilde{\beta}_n}^I &= -\mathbf{A}_{e=1}^{n_{\text{ele}}} \left[ \int_{B_{0,e}} \left( \left( \frac{\partial f_{B_0,n}^h}{\partial \tilde{\alpha}} + \frac{\partial f_{B_0,n}^h}{\partial \gamma^p} \frac{\partial \gamma_n^{\text{ph}}}{\partial \tilde{\alpha}} + \frac{\partial f_{B_0,n}^h}{\partial n_{ef}} \frac{\partial n_{ef,n}^h}{\partial \tilde{\alpha}} \right) N^I + \frac{\partial f_{B_0,n}^h}{\partial \nabla \tilde{\alpha}_a} \frac{\partial N^I}{\partial X_a} \right. \right. \\ &\quad \left. \left. + H_{cd,n}^h \omega_m^{hp} \left( \frac{\partial P_{cd,n}^h}{\partial \gamma^p} \frac{\partial \gamma_n^{\text{ph}}}{\partial \tilde{\alpha}} + \frac{\partial P_{cd,n}^h}{\partial n_{ef}} \frac{\partial n_{ef,n}^h}{\partial \tilde{\alpha}} \right) N^I + \omega_m^{hp} p_p^h \tilde{\beta}_n^h \left( 1 - \frac{\partial \alpha_n^h}{\partial \gamma^p} \frac{\partial \gamma_n^{\text{ph}}}{\partial \tilde{\alpha}} \right) N^I \right. \right. \\ &\quad \left. \left. + \omega_m^{hp} q_p^h \frac{\partial \tilde{\beta}_n^h}{\partial X_a} \frac{\partial N^I}{\partial X_a} \right) dV + \int_{\partial B_{0,e}^N} \frac{\partial f_{\partial B_{0,e}^N,n}^h}{\partial \tilde{\alpha}} N^I dA + \int_{\partial B_{0,e}^D} \left( \frac{\partial f_{\partial B_{0,e}^D,n}^h}{\partial \tilde{\alpha}} - w_{a,n}^h \frac{\partial T_{a,n}^h}{\partial \tilde{\alpha}} \right) N^I dA \right], \\ \mathcal{K}_{w_i w_j,n}^{IJ} &= \mathbf{A}_{e=1}^{n_{\text{ele}}} \int_{B_{0,e}} \frac{\partial N^I}{\partial X_a} \left( \omega_m^{hp} \left( \frac{\partial P_{jb,n}^h}{\partial F_{ia}} + \frac{\partial P_{jb,n}^h}{\partial \gamma^p} \frac{\partial \gamma_n^{\text{ph}}}{\partial F_{ia}} + \frac{\partial P_{jb,n}^h}{\partial n_{ef}} \frac{\partial n_{ef,n}^h}{\partial F_{ia}} \right) + (1 - \omega_m^{hp}) \frac{\partial \sigma_{jb,n}^{\text{fh}}}{\partial F_{ia}} \right) \frac{\partial N^J}{\partial X_b} dV, \\ \mathcal{K}_{w_i \tilde{\beta}_n}^{IJ} &= \mathbf{A}_{e=1}^{n_{\text{ele}}} \int_{B_{0,e}} \frac{\partial N^I}{\partial X_a} \left( -\omega_m^{hp} p_p^h \frac{\partial \alpha_n^h}{\partial \gamma^p} \frac{\partial \gamma_n^{\text{ph}}}{\partial F_{ia}} \right) N^J dV, \\ \mathcal{K}_{\tilde{\beta}_n w_j,n}^{IJ} &= \mathbf{A}_{e=1}^{n_{\text{ele}}} \int_{B_{0,e}} N^I \omega_m^{hp} \left( \frac{\partial P_{jb,n}^h}{\partial \gamma^p} \frac{\partial \gamma_n^{\text{ph}}}{\partial \tilde{\alpha}} + \frac{\partial P_{jb,n}^h}{\partial n_{ef}} \frac{\partial n_{ef,n}^h}{\partial \tilde{\alpha}} \right) \frac{\partial N^J}{\partial X_b} dV, \\ \mathcal{K}_{\tilde{\beta}_n \tilde{\beta}_n}^{IJ} &= \mathbf{A}_{e=1}^{n_{\text{ele}}} \int_{B_{0,e}} \left( \omega_m^{hp} p_p^h N^I \left( 1 - \frac{\partial \alpha_n^h}{\partial \gamma^p} \frac{\partial \gamma_n^{\text{ph}}}{\partial \tilde{\alpha}} \right) N^J + \omega_m^{hp} q_p^h \frac{\partial N^I}{\partial X_a} \frac{\partial N^J}{\partial X_a} \right) dV. \end{aligned} \quad (45)$$

It should be noted that the above equations do not involve the derivatives  $\partial_H \eta_n^p$ ,  $\partial_H \pi_n$ ,  $\partial_{\tilde{\beta}_n} \eta_n^p$ , and  $\partial_{\tilde{\beta}_n} \pi_n$  as required in Eq. (42). That is, calculating additional vectors and tensors for the adjoint problem are unnecessary, except for  $w$  and  $\tilde{\beta}$ . Also, the tangent matrix of the adjoint problem is the transpose of the tangent matrix of the primal problem, and this relationship is a well-known mathematical fact. Therefore, the derivations presented so far are presumed to be correct.

### 3.3. Discretization of the design variable update method

The weak forms for the reaction–diffusion equations in Eq. (36) can be written as

$$\begin{aligned} & \text{for } i = 1, 2, \dots, m-1, m \\ & \int_{D_0} \left( \dot{\omega}_i \delta \omega_i + l_d^2 \frac{\partial \omega_i}{\partial \mathbf{X}} \cdot \frac{\partial \delta \omega_i}{\partial \mathbf{X}} - C_{D_0, i} s_{D_0, i} \delta \omega_i \right) dV \\ & - \int_{\partial D_0^N} C_{\partial D_0^N, i} s_{\partial D_0^N, i} \delta \omega_i dA - \int_{\partial D_0^D} C_{\partial D_0^D, i} s_{\partial D_0^D, i} \delta \omega_i dA = 0. \end{aligned} \tag{46}$$

For the temporal discretization of the optimization problem, the pseudo time  $\tilde{t}$  is introduced, and a quantity at the pseudo time step  $\tilde{t}_{\bar{n}}$  and its increment are denoted by  $\bullet_{\bar{n}}$  and  $\Delta \bullet_{\bar{n}}$ , respectively, with  $\Delta \tilde{t}_{\bar{n}} = \tilde{t}_{\bar{n}} - \tilde{t}_{\bar{n}-1}$  being the pseudo time interval. Notably, the pseudo time interval  $\Delta \tilde{t}_{\bar{n}}$  is an input parameter in actual optimization calculations, and its value cannot be set too large. From our experience,  $0.01 \leq \Delta \tilde{t}_{\bar{n}} \leq 0.1$  can realize a relatively stable optimization process for elastoplastic problems. This is because  $C_{\partial D_0^N, i} s_{\partial D_0^N, i}$  in Eq. (46) usually has the value in the range of  $-1 \sim +1$ , and thus, the maximum value of  $|C_{\partial D_0^N, i} s_{\partial D_0^N, i} \Delta \tilde{t}_{\bar{n}}|$  can be limited within  $0.01 \sim 0.1$ . Thereby, the material configuration is not dramatically changed in one design iteration, avoiding the divergence of the optimization process.

Also, in this study, the design variables  $\{\omega_1, \omega_2, \dots, \omega_{m-1}, \omega_m\}$  are defined as nodal variables, i.e.,  $\{\omega_1^I, \omega_2^I, \dots, \omega_{m-1}^I, \omega_m^I\}$ . Then, by applying standard FE approximation in space and backward Euler scheme in time to the left-hand side of Eq. (46), the following node-level global residual vectors and tangent matrices for the optimization problem are obtained:

$$\begin{aligned} & \text{for } i = 1, 2, \dots, m-1, m \\ & \mathcal{R}_{\omega_i, n}^I = - \mathbf{A}_{e=1}^{n_{ele}} \left[ \int_{D_{0,e}^h} \left( \frac{\omega_{i, \bar{n}+1}^h - \omega_{i, \bar{n}}^h}{\Delta \tilde{t}_{\bar{n}}} N^I + l_d^2 \frac{\partial \omega_{i, \bar{n}+1}^h}{\partial X_a} \frac{\partial N^I}{\partial X_a} - C_{D_0, i, \bar{n}} s_{D_0, i, \bar{n}}^h N^I \right) dV \right. \\ & \quad \left. - \int_{\partial D_{0,e}^{N_h}} C_{\partial D_0^N, i, \bar{n}} s_{\partial D_0^N, i, \bar{n}}^h N^I dA - \int_{\partial D_{0,e}^{D_h}} C_{\partial D_0^D, i, \bar{n}} s_{\partial D_0^D, i, \bar{n}}^h N^I dA \right], \\ & \mathcal{K}_{\omega_i \omega_i, n}^{IJ} = \mathbf{A}_{e=1}^{n_{ele}} \int_{D_{0,e}^h} \left( \frac{N^I N^J}{\Delta \tilde{t}_{\bar{n}}} + l_d^2 \frac{\partial N^I}{\partial X_a} \frac{\partial N^J}{\partial X_a} \right) dV, \end{aligned} \tag{47}$$

where

$$\begin{aligned} s_{D_0, i, \bar{n}}^h &= \left( \sum_{n=1}^{N_{step}} \Delta s_{D_0, i, \bar{n}, n}^h \right) - \sum_{l=1}^i (\theta_{l, \bar{n}} - \theta_{l+1, \bar{n}}) \frac{1}{\omega_{i, \bar{n}}} \prod_{k=1}^m \omega_{k, \bar{n}} \text{ in } D_0, \\ \text{with } \Delta s_{D_0, i, \bar{n}, n}^h &= \begin{cases} \left[ \frac{\partial f_{B_0, \bar{n}, n}^h}{\partial \omega_i} + \omega_{m, \bar{n}}^{hp} \left( H_{ab, \bar{n}, n}^h \frac{\partial P_{ab, \bar{n}, n}^h}{\partial \omega_i} - u_{a, \bar{n}, n}^h \frac{\partial B_{a, \bar{n}}^h}{\partial \omega_i} \right. \right. \\ \quad \left. \left. - n_{\bar{n}, n}^{ph} \left( \frac{\partial \|\tau_{dev, \bar{n}, n}^h\|}{\partial \omega_i} - \sqrt{\frac{2}{3}} \left( \frac{\partial R_{\bar{n}, n}^h}{\partial \omega_i} (j_{0, \bar{n}}^h + r_{\bar{n}, n}^{ph}) + R_{\bar{n}, n}^h \left( \frac{\partial y_{0, \bar{n}}^h}{\partial \omega_i} + \frac{\partial r_{\bar{n}, n}^{ph}}{\partial \omega_i} \right) \right) \right) \right] \\ \quad + \frac{\partial p_{p, \bar{n}}^h}{\partial \omega_i} \bar{\beta}_{\bar{n}, n}^h (\bar{\alpha}_{\bar{n}, n}^h - \alpha_{\bar{n}, n}^h) + \frac{\partial q_{p, \bar{n}}^h}{\partial \omega_i} \frac{\partial \bar{\beta}_{\bar{n}, n}^h}{\partial X_a} \frac{\partial \bar{\alpha}_{\bar{n}, n}^h}{\partial X_a} \Big] \Delta t_n \text{ for } i = 1, 2, \dots, m-1 \\ \left[ \frac{\partial f_{B_0, \bar{n}, n}^h}{\partial \omega_m} + \frac{\partial \omega_{m, \bar{n}}^{hp}}{\partial \omega_m} \left( H_{ab, \bar{n}, n}^h (P_{ab, \bar{n}, n}^h - \sigma_{ab, \bar{n}, n}^{fh}) - u_{a, \bar{n}, n}^h B_{a, \bar{n}}^h \right. \right. \\ \quad \left. \left. + p_{p, \bar{n}}^h \bar{\beta}_{\bar{n}, n}^h (\bar{\alpha}_{\bar{n}, n}^h - \alpha_{\bar{n}, n}^h) + q_{p, \bar{n}}^h \frac{\partial \bar{\beta}_{\bar{n}, n}^h}{\partial X_a} \frac{\partial \bar{\alpha}_{\bar{n}, n}^h}{\partial X_a} \right) \right] \Delta t_n \text{ for } i = m, \end{cases} \tag{48} \\ s_{\partial D_0^N, i, \bar{n}}^h &= \sum_{n=1}^{N_{step}} \Delta s_{\partial D_0^N, i, \bar{n}, n}^h \text{ on } \partial D_0^N \quad \text{with } \Delta s_{\partial D_0^N, i, \bar{n}, n}^h = \left[ \frac{\partial f_{\partial B_0^N, \bar{n}, n}^h}{\partial \omega_i} - u_{a, \bar{n}, n}^h \frac{\partial \bar{T}_{a, \bar{n}, n}^h}{\partial \omega_i} \right] \Delta t_n, \\ s_{\partial D_0^D, i, \bar{n}}^h &= \sum_{n=1}^{N_{step}} \Delta s_{\partial D_0^D, i, \bar{n}, n}^h \text{ on } \partial D_0^D \\ \text{with } \Delta s_{\partial D_0^D, i, \bar{n}, n}^h &= \begin{cases} \left[ \frac{\partial f_{\partial B_0^D, \bar{n}, n}^h}{\partial \omega_i} - \omega_{m, \bar{n}}^{hp} u_{a, \bar{n}, n}^h \frac{\partial P_{ab, \bar{n}, n}^h}{\partial \omega_i} N_b^h \right] \Delta t_n \text{ for } i = 1, 2, \dots, m-1 \\ \left[ \frac{\partial f_{\partial B_0^D, \bar{n}, n}^h}{\partial \omega_m} - \frac{\partial \omega_{m, \bar{n}}^{hp}}{\partial \omega_m} u_{a, \bar{n}, n}^h (P_{ab, \bar{n}, n}^h - \sigma_{ab, \bar{n}, n}^{fh}) N_b^h \right] \Delta t_n \text{ for } i = m. \end{cases} \end{aligned}$$

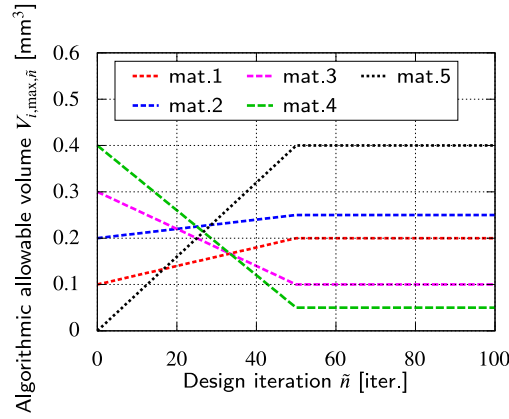


Fig. 4. Relationship between algorithmic allowable volumes and design iteration for five materials. (Also, refer to Eq. (50)).

Here,  $N_{\text{step}}$  denotes the total time steps of the primal and adjoint problems. It should be emphasized that the subscript  $i$  in the above equations is not an index of tensor components but an ID of the design variable under consideration. Also, it is worth mentioning that the semi-implicit method is employed to update the design variables. That is, the sensitivity is fixed at  $\tilde{t} = \tilde{t}_{\tilde{n}}$ , and only the design variable  $\omega_{i,\tilde{n}+1}$  is the unknown. Accordingly, the derivatives,  $\partial_{\omega_i} s_{D_0,i,\tilde{n}}^h$  and  $\partial_{\omega_j} s_{D_0,i,\tilde{n}}^h$  ( $j \neq i$ ), do not appear, and the coupled problem of  $m$  design variables has a global tangent matrix with only diagonal terms.

On the other hand, the following algorithmic process is adopted for multi-material volume constraints:

for  $i = 1, 2, \dots, m - 1, m$

$$\bar{V}_{i,\tilde{n}} = \int_{D_0} \underbrace{\left( \prod_{k=i}^m \omega_{k,\tilde{n}} - \prod_{k=i-1}^m \omega_{k,\tilde{n}} \right)}_{V_{i,\tilde{n}}} dV - \underbrace{\left( V_{i,\text{max}} + (V_{i,\text{ini}} - V_{i,\text{max}}) \max \left[ 0, 1 - \frac{\tilde{n}}{\tilde{n}_{\text{vol}}} \right] \right)}_{V_{i,\text{max},\tilde{n}}}, \quad (49)$$

where  $V_{i,\text{ini}}$  and  $V_{i,\text{max}}$  denote the initial and actual allowable volumes for the  $i$ th material, respectively, and  $\tilde{n}_{\text{vol}}$  is the number of design iterations to reduce the allowable volume from  $V_{i,\text{ini}}$  to  $V_{i,\text{max}}$ . Suppose the design domain  $D_0$  has the total volume of 1 mm<sup>3</sup> and five materials construct the domain ( $m + 1 = 5$ ), and the following allowable volumes are given:

$$\begin{aligned} V_{1,\text{ini}} + V_{2,\text{ini}} + V_{3,\text{ini}} + V_{4,\text{ini}} + V_{5,\text{ini}} &= 0.10 + 0.20 + 0.30 + 0.40 + 0.00, \\ V_{1,\text{max}} + V_{2,\text{max}} + V_{3,\text{max}} + V_{4,\text{max}} + V_{5,\text{max}} &= 0.20 + 0.25 + 0.10 + 0.05 + 0.40. \end{aligned} \quad (50)$$

The relationships between the algorithmic allowable volumes  $V_{i,\text{max},\tilde{n}}$  and the design iteration  $\tilde{n}$  are presented in Fig. 4, where  $\tilde{n}_{\text{vol}} = 50$  is given.

Meanwhile, following Otomori et al. [42], the penalty parameters  $\theta_{i,\tilde{n}}$  are calculated as follows:

for  $i = 1, 2, \dots, m - 1, m$

$$\theta_{i,\tilde{n}} = \underbrace{\bar{\theta}_{i,\tilde{n}}}_{=\theta_{i,\tilde{n}} \text{ in Eq. (88)}} \exp \left( s_v \frac{\bar{V}_{i,\tilde{n}}}{V_{i,\text{max},\tilde{n}}} \right), \quad (51)$$

where  $s_v$  denotes the saturation parameter to determine the exponential penalty function. Here,  $\bar{\theta}_{i,\tilde{n}}$  in Eq. (51) are the solutions of the system of  $m$  linear equations, which is derived in Appendix B.3. Also, it is worth mentioning that the multipliers  $\theta_{i,\tilde{n}}$  work as the average sensitivity of the design domain at the design iteration  $\tilde{n}$ , which is compared with the local sensitivity  $\bar{s}_{D_0,i,\tilde{n}}$  to determine if the design variable  $\omega_{i,\tilde{n}+1}$  increases or decreases. Additionally, the normalization factor  $C_{D_0,i,\tilde{n}}$  in Eq. (47) is calculated by Eq. (89).

### 3.4. Optimization algorithm

Algorithm 1 presents the overall optimization algorithm to address MMTO, which has been enhanced from the optimization algorithm employed in our previous studies [33,35]. The pseudo-time steps (design iterations) construct the outermost loop in the optimization process. At every pseudo-time step (design iteration)  $\tilde{n}$ , the SIMP-based interpolation function in Eq. (9) is used to update the material properties.

Subsequently, the nonlinear primal and linear adjoint problems are solved in the loop of the actual-time steps. To be specific, the internal state variables and nodal variables are solved by the local and global Newton–Raphson schemes, respectively. In the meantime, at each incremental step (time step), the increment of sensitivity is calculated at every integration point. At the end of

**Algorithm 1** Optimization algorithm

---

```

1: while The convergence criterion in Eq. (52) is not satisfied do
2:    $\tilde{n} = \tilde{n} + 1$  ( $\tilde{n}$  denotes the current design iteration (pseudo-time step))
3:   Create the material distribution of  $\tilde{n}$ -th design iteration by Eq. (9) with  $\{\omega_{1,\tilde{n}}^I, \omega_{2,\tilde{n}}^I, \dots, \omega_{m-1,\tilde{n}}^I, \omega_{m,\tilde{n}}^I\}$ 
4:   for incremental step (time step)  $n$  ( $\leq N_{\text{step}}$ ) do
5:      $n = n + 1$  ( $n$  denotes the current actual-time step)
6:     for Newton–Raphson loop do
7:        $k = k + 1$  ( $k$  denotes the current global Newton–Raphson iteration)
8:       for Finite element assembling do
9:         Solve Eq. (39) and Eq. (43) to determine  $\{\gamma_n^{\text{ph}}, \mathbf{n}_n^h, \eta_n^{\text{ph}}, \boldsymbol{\pi}_n^h\}$  at every integration point
10:        Calculate the increments of the sensitivity in Eq. (48)
11:      end for
12:      Solve Eq. (38) and Eq. (45) to determine  $\{u_n^I, \bar{\alpha}_n^I, \mathbf{w}_n^I, \bar{\beta}_n^I\}$  at every node
13:      If the Newton–Raphson scheme is converged: exit
14:    end for
15:  end for
16:  Solve Eq. (36) for determining  $\{\omega_{1,\tilde{n}+1}^I, \omega_{2,\tilde{n}+1}^I, \dots, \omega_{m-1,\tilde{n}+1}^I, \omega_{m,\tilde{n}+1}^I\}$ 
17:  If the convergence criterion in Eq. (52) is satisfied: exit
18: end while

```

---

every design iteration,  $m$  reaction–diffusion equations are solved to update  $m$  design variables. Then, the following relative error is also calculated to check if the optimization is converged or not:

$$\begin{cases} \text{IF error}_{\tilde{n}} > \text{TOL} : \text{Not converged} \\ \text{IF error}_{\tilde{n}} \leq \text{TOL} : \text{Converged} \end{cases} \quad (52)$$

with  $\text{error}_{\tilde{n}} = \frac{\|\Delta\omega_{\tilde{n}}\|}{\sqrt{n_{\text{node}}}}$  and  $\Delta\omega_{i,\tilde{n}}^I = \omega_{i,\tilde{n}+1}^I - \omega_{i,\tilde{n}}^I$  ( $i = 1, 2, \dots, m-1, m$ ).

For convenience, we call  $\text{error}_{\tilde{n}}$  “optimization error” hereafter.

#### 4. Numerical examples

In this section, two numerical examples are prepared to demonstrate the capability of the proposed method. To this end, the following objective function is adopted:

$$\mathcal{F} = \int_t \left[ - \int_{B_0} \omega_m^p \mathbf{B} \cdot \mathbf{u} \, dV - \int_{\partial B_0^N} \bar{\mathbf{T}} \cdot \mathbf{u} \, dA + \int_{\partial B_0^D} \mathbf{T} \cdot \bar{\mathbf{u}} \, dA \right] dt, \quad (53)$$

which corresponds to the conventional stiffness maximization problem. Particularly, Example 1 and Example 2 have different objectives to show the ability of the proposed method.

Example 1 discusses the computational stability of the optimization process using the conventional plastic model and the subloading surface model. Single-material topology optimization for a cantilever beam is studied, in which the difficulty in convergence due to the conventional plastic model is demonstrated, and the benefit of the subloading surface model on the stable optimization process is revealed afterward.

Example 2 aims to study unconventional multi-material topology optimization for a wedge specimen, say displacement magnitude-dependent MMTO. The uniqueness of this example is the underlying optimization concept for stiffness maximization problems. Specifically, Young’s modulus and Poisson’s ratios are identical for all base materials, and the material distribution and arrangement are determined by referring to the different degrees of plastic hardening behavior.

For all numerical examples,  $p = 3$  is chosen for the SIMP-based interpolation function in Eq. (9). Also, the condition  $y_{0,i}/y_{0,i+1} = p_{p,i}/p_{p,i+1} = q_{p,i}/q_{p,i+1}$  ( $i = 1, 2, \dots, m-1$ ) is postulated to maintain the even contributions of the penalty and diffusive terms in Eqs. (12)<sub>4</sub>, (28)<sub>6–8</sub> for micromorphic regularization; refer to Han et al. [35] for details. Additionally, the material parameters for the ersatz material are set to  $E_{m+1} = 10^{-3}E_1$  and  $\nu_{m+1} = \nu_1$ . The body force and prescribed traction force vectors,  $\mathbf{B}$  and  $\bar{\mathbf{T}}$ , respectively, are neglected in the following numerical examples.

**Remark 1.** In the following numerical examples, the benefit of employing nonlocal plasticity to address the mesh-dependency problem is not discussed since this issue is not the main concern of this study. Readers can refer to Han et al. [35] for the detailed investigation of nonlocal plasticity in elastoplastic topology optimization.

**Table 2**  
Material and optimization parameters for Example 1.

Material parameter*		Value	Unit
Young's modulus	$E_1$	200 000	[MPa]
Poisson's ratio	$\nu_1$	0.3	[-]
Initial yield stress	$\gamma_{0,1}$	500	[MPa]
Linear hardening parameter	$h_1$	100, 1000, 10000, 100000	[MPa]
Normal-yield threshold	$R_1^c$	0.3, 0.5, 0.7	[-]
Normal-yield saturation parameter	$R_1^p$	300, 500, 700	[-]
Penalty parameter	$p_{p,1}$	10 000	[MPa]
Diffusion parameter	$q_{p,1}$	72 000	[MPa mm <sup>2</sup> ]

Optimization parameter		Value	Unit
Allowance volume	$V_{1,max}$	0.50	[-]
Saturation parameter	$s_v$	10	[-]
Iteration number	$\tilde{n}_{vol}$	50	[iter.]
Pseudo-time increment	$\Delta \tilde{t}_i$	0.05	[s]
Diffusion coefficient	$l_d^2$	4 <sup>2</sup>	[mm <sup>2</sup> ]
Convergence tolerance	TOL <sub>c</sub>	10 <sup>-4</sup>	[-]

**Table 3**  
Optimization cases for Example 1.

Case*	$R_1^c$ [-]	$R_1^p$ [-]	$h_1$ [MPa]
<b>Section 4.1.1</b>			
Case h10 <sup>2</sup> -con	-	-	100
Case h10 <sup>3</sup> -con	-	-	1000
Case h10 <sup>4</sup> -con	-	-	10 000
Case h10 <sup>5</sup> -con	-	-	100 000
<b>Section 4.1.2</b>			
Case h10 <sup>2</sup> -sub**	0.5	500	100
Case h10 <sup>3</sup> -sub	0.5	500	1000
Case h10 <sup>4</sup> -sub	0.5	500	10 000
Case h10 <sup>5</sup> -sub	0.5	500	100 000
<b>Section 4.1.3</b>			
Case Re03	0.3	500	100
Case Re05**	0.5	500	100
Case Re07	0.7	500	100
<b>Section 4.1.4</b>			
Case Rp300	0.5	300	100
Case Rp500**	0.5	500	100
Case Rp700	0.5	700	100

\* The letters beginning with “h” mean the value of the plastic hardening variable (accumulated plastic strain). The part “Re” or “Rp” presents what parametric studies are under consideration. The letters “con” and “sub” correspond to the conventional plastic model and subloading surface model.

\*\* Case Re05 and Case Rp500 are identical to Case h10<sup>2</sup>-sub.

#### 4.1. Example 1: Single-material topology optimization for a cantilever beam

As illustrated in Fig. 5, the first example considers a cantilever beam-like 2D structure subjected to a vertical deformation of 10 mm, and the single-material topology optimization (topology optimization of ersatz and actual materials) is demonstrated. That is, only the interpolation of the nonlocal elastoplastic material and linearly elastic material is considered by referring to Eq. (10). Thus, unrealistic plastic deformation does not occur in the void regions. Also, the linear plastic hardening is assumed for the elastoplastic response. The material and optimization parameters are listed in Table 2. Here, the diffusion coefficient  $l_d = 4$  mm is given since we have confirmed that if the value is almost the same as the mesh size (4 mm), the obtained optimal design can properly reflect the mesh size. If a larger value is given, the optimal design becomes what can be obtained by coarser mesh, whereas a smaller value leads to a noisy material distribution; also see Otomori et al. [42] and Han et al. [35] for the parametric studies of the diffusion coefficient  $l_d$ . Also, given a sufficiently small convergence criterion  $TOL_c = 10^{-4}$ , it does not regard the optimization as converged for an averaged absolute error of 0.01 % of design variables; see Han et al. [33] for details. This is beneficial for finding the underlying problem of the conventional plastic model in what follows. Additionally, different values of the linear hardening parameter, normal-yield threshold, and normal-yield saturation parameter are provided so that a parametric study can be made, for which the optimization cases are presented in Table 3.

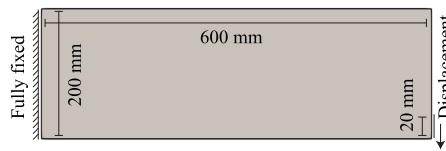


Fig. 5. Target design domain of Example 1: Geometry and boundary conditions (Meshsize: 4 mm).

#### 4.1.1. Difficulty in convergence for conventional plastic model

First, we demonstrate the difficulty in convergence of the optimization process when using the conventional plastic model. Here, the conventional plastic model can be created by giving  $R_1^c = 1.0$  or  $R_1^p \rightarrow \infty$  in the subloading surface model and used for the first four cases in Table 3; also see the fifth and sixth panels in Fig. 3. Fig. 6(a) shows the optimization error versus design iteration for these cases with different values of the linear plastic hardening parameter  $h_1$ . As can be seen from this figure, all four cases do not converge until two thousand design iterations. Specifically, the optimization error gradually decreases initially but oscillates afterward. To quantify the oscillation behavior, the following oscillation factor is defined:

$$O_{\text{factor}, \bar{n}+1} = \begin{cases} O_{\text{factor}, \bar{n}} + 1 & \text{if } (\text{error}_{\bar{n}+1} - \text{error}_{\bar{n}}) (\text{error}_{\bar{n}} - \text{error}_{\bar{n}-1}) \geq 0 \\ O_{\text{factor}, \bar{n}} - 1 & \text{otherwise,} \end{cases} \quad (54)$$

which is set to increase by one if the optimization error increases or decreases two consecutive times. In other words, the larger the oscillation of the optimization error is, the smaller the value of the oscillation factor is; the optimization case with larger oscillations yields a downward curve to the right. Fig. 6(b) shows the oscillation factor versus design iteration of these four cases. It can be seen from this figure that the value of the oscillation factor decreases as the design iteration increases. Indeed, by giving a larger convergence tolerance, e.g.,  $\text{TOL} = 10^{-2}$ , the optimization process can converge even if the oscillatory tendency of the optimization error is confirmed. However, recalling the definition of the optimization error in Eq. (52),  $\text{TOL} = 10^{-2}$  allows 1% averaged absolute error for design variables  $\Delta\omega^f$ . As can be seen from Figs. 6(c) and (d), this large convergence tolerance also allows that the maximum absolute error of the design variable  $|\Delta\omega^f|_{\max}$  changes more than  $|\Delta\omega^f|_{\max} > 0.1$  and allow that the relative error of the objective function  $|\Delta F|$  changes more than 0.1% between two consecutive design iterations. In short, it ignores changes of the design variable (or material distribution) that are not so small. In this study, we do not regard this situation to be a converged state and only allow 0.01% averaged absolute error ( $\text{TOL} = 10^{-4}$ ).

This oscillatory tendency of the optimization error is due to the repeated changes in the deformation state; see Fig. 7 that shows the distributions of deformation state during the design iterations  $\bar{n} = 2001 \sim 2006$  for Case h10<sup>2</sup>-con. Here, the blue- and red-colored regions in the bottom snapshot exhibit elastic and plastic deformations, respectively. As shown in this figure, the circled regions show alternating deformation states, and such a trend is found in several locations within the design region. Additionally, the oscillations in the deformation state and the resulting oscillation in the optimization error can be explained by reference to the material Jacobian of the primal problem because it is used to determine the adjoint variables in the adjoint problem. In the following, we attempt to explain this.

To simplify the discussion, we consider the following one-directional setup considering linear plastic hardening:

$$\begin{aligned} \text{Material Jacobian in elastic deformation state: } & \left. \frac{\partial\sigma}{\partial\varepsilon} \right|_e = \frac{\partial E_1 \varepsilon}{\partial\varepsilon} = E_1, \\ \text{Material Jacobian in plastic deformation state: } & \left. \frac{\partial\sigma}{\partial\varepsilon} \right|_p = \frac{\partial E_1 (\varepsilon - \varepsilon^p)}{\partial\varepsilon} = \frac{E_1 h_1}{E_1 + h_1}. \end{aligned} \quad (55)$$

Here, assuming the Young's modulus and initial yield stress as above, the values of the material Jacobian in the plastic deformation state are  $E_1 h_1 / (E_1 + h_1) = 99.95, 995.02, 9523.81, 66666.67$  MPa with  $h_1 = 100, 1000, 10000, 100000$  MPa, respectively. In the conventional plastic model, the material Jacobian changes dramatically around the plastic yield point, which is believed to significantly reduce the convergence tendency of the optimization process. For instance, a typical story leading to oscillation in the optimization error can be summarized in the following five events:

1. Supposing that the location  $X$  exhibits elastic deformation at design iteration  $\bar{n}$ , the material Jacobian is relatively large (Eq. (55)<sub>1</sub>), and thus relatively smaller adjoint variables are computed.
2. Roughly speaking, if the adjoint variables are relatively small, the resulting sensitivity becomes small. Accordingly, the design variable  $\omega_{1, \bar{n}+1}$  at  $X$  tends to decrease, i.e.,  $\Delta\omega_{1, \bar{n}} < 0$ .
3. Once the design variable  $\omega_{1, \bar{n}+1}$  becomes small, the region around  $X$  becomes softer than the previous design iteration  $\bar{n}$ . This tendency can lead to a large local deformation (or strain) at  $X$  at design iteration  $\bar{n} + 1$ .
4. The large local deformation leads to plastic yielding at  $X$ , which results in relatively small material Jacobian, and accordingly, relatively large adjoint variables to be computed.
5. Contrary to the 2nd event, relatively larger adjoint variables lead to a larger value of sensitivity, and then the design variable  $\omega_{1, \bar{n}+2}$  at  $X$  increases, i.e.,  $\Delta\omega_{1, \bar{n}+1} > 0$ . Eventually, the situation goes back to the 1st event.

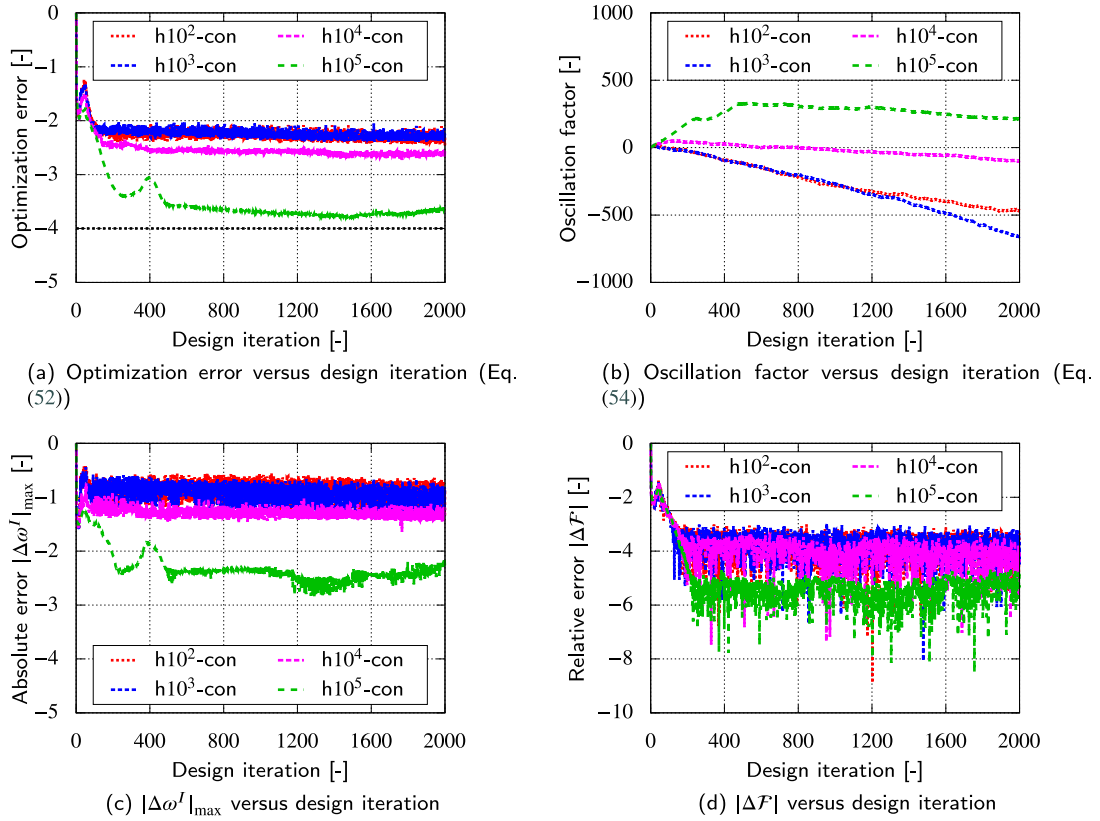


Fig. 6. Optimization error, oscillation factor, maximum absolute error of the design variable  $|\Delta\omega^f|_{\max}$ , relative error of the objective function  $|\Delta\mathcal{F}|$  versus design iteration for Example 1: Conventional plastic model. The black-colored line in (a) denotes the convergence tolerance “TOL”. (For interpretation of the references to color in this figure legend, the reader is referred to the web version of this article.)

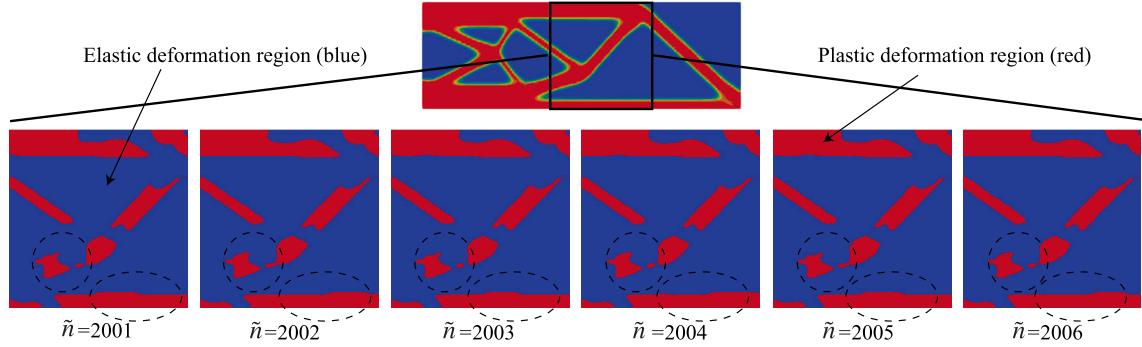


Fig. 7. Oscillation of deformation states: Case c- $h10^2$ -con. The blue-/red-colored region exhibits elastic/plastic deformation.

It is worth mentioning that a larger value of linear hardening parameter  $h$  is likely to mitigate the oscillation of the optimization error to some extent. In fact, for the current four cases, as the value of the linear hardening parameter  $h$  increases, the oscillation trend of the optimization error is alleviated; compare the magenta- and green-colored curves with the red- and blue-colored curves in Fig. 6(b).

#### 4.1.2. Stabilization of optimization process with subloading surface model

Hereafter, the subloading surface model is used in the primal problem for elastoplastic topology optimization. To this end, the normal-yield threshold  $R_1^c$  and normal-yield saturation parameter  $R_1^p$  are set to 0.5 and 500, respectively. Fig. 8 shows the histories of the optimization error, oscillation factor, maximum absolute error of the design variable  $|\Delta\omega^f|_{\max}$ , and relative error of the objective function  $|\Delta\mathcal{F}|$  with respect to the design iterations and the reaction force–displacement curves for the second four cases in Table 3

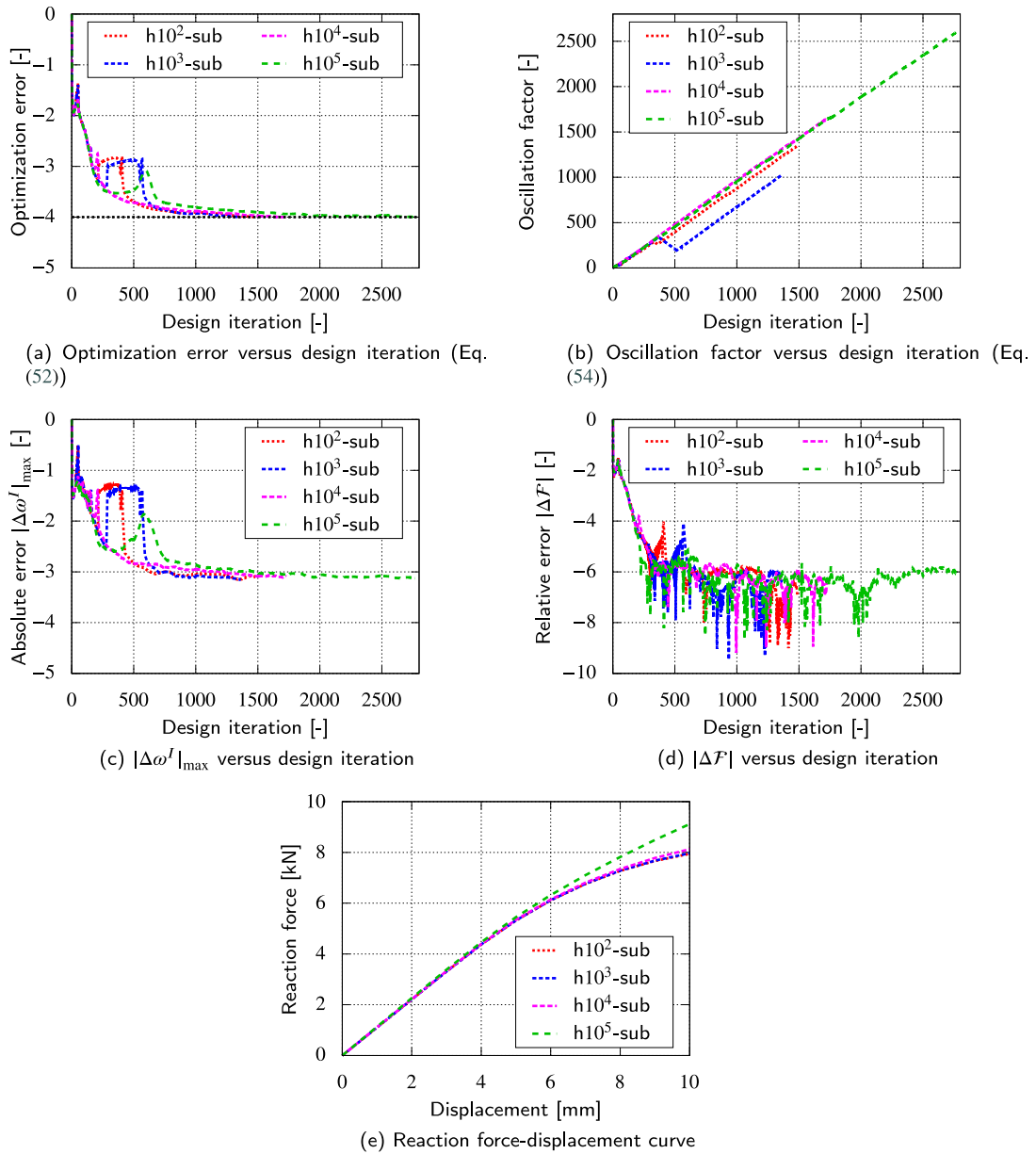


Fig. 8. Optimization error versus design iteration, oscillation factor versus design iteration, maximum absolute error of the design variable  $|\Delta\omega^I|_{\max}$  versus design iteration, relative error of the objective function  $|\Delta\mathcal{F}|$  versus design iteration, and reaction force–displacement curve for Example 1: Subloading surface model. The black-colored line in (a) denotes the convergence tolerance “TOL”. (For interpretation of the references to color in this figure legend, the reader is referred to the web version of this article.)

with different values of the linear plastic hardening parameter  $h_1$ . Readers interested in the history of the objective function can refer to Fig. 34(a) in Appendix C. As can be seen from panels (a) and (b) of Fig. 8, the optimization error does not oscillate, and all of these four cases successfully converge over a wide range of plastic hardening responses, i.e.,  $h_1 = 10^2 \sim 10^5$  MPa. Also, from the figure (c), only a small value (i.e., 0.001) of the maximum absolute error of the design variable  $|\Delta\omega^I|_{\max}$  is found. In addition, the relative error of the objective function  $|\Delta\mathcal{F}|$  is almost less than 0.001% ( $|\Delta\mathcal{F}| \approx 10^{-6}$ ) for all the four cases; see figure (d). As shown in Fig. 3, the success is due to the fact that the subloading surface model does not have a definite yielding point that significantly changes the material Jacobian of the primal problem and that its material Jacobian continuously changes during the transition from the elastic to plastic deformation state. Therefore, incorporating the subloading surface model into the elastoplastic topology optimization framework is essential to ensure stability.

On the other hand, Fig. 9 presents the optimal designs with distributions of deformation states, nonlocal plastic hardening variable, and normal-yield rate. Here, the optimal design obtained from the linear elastic topology optimization is presented as

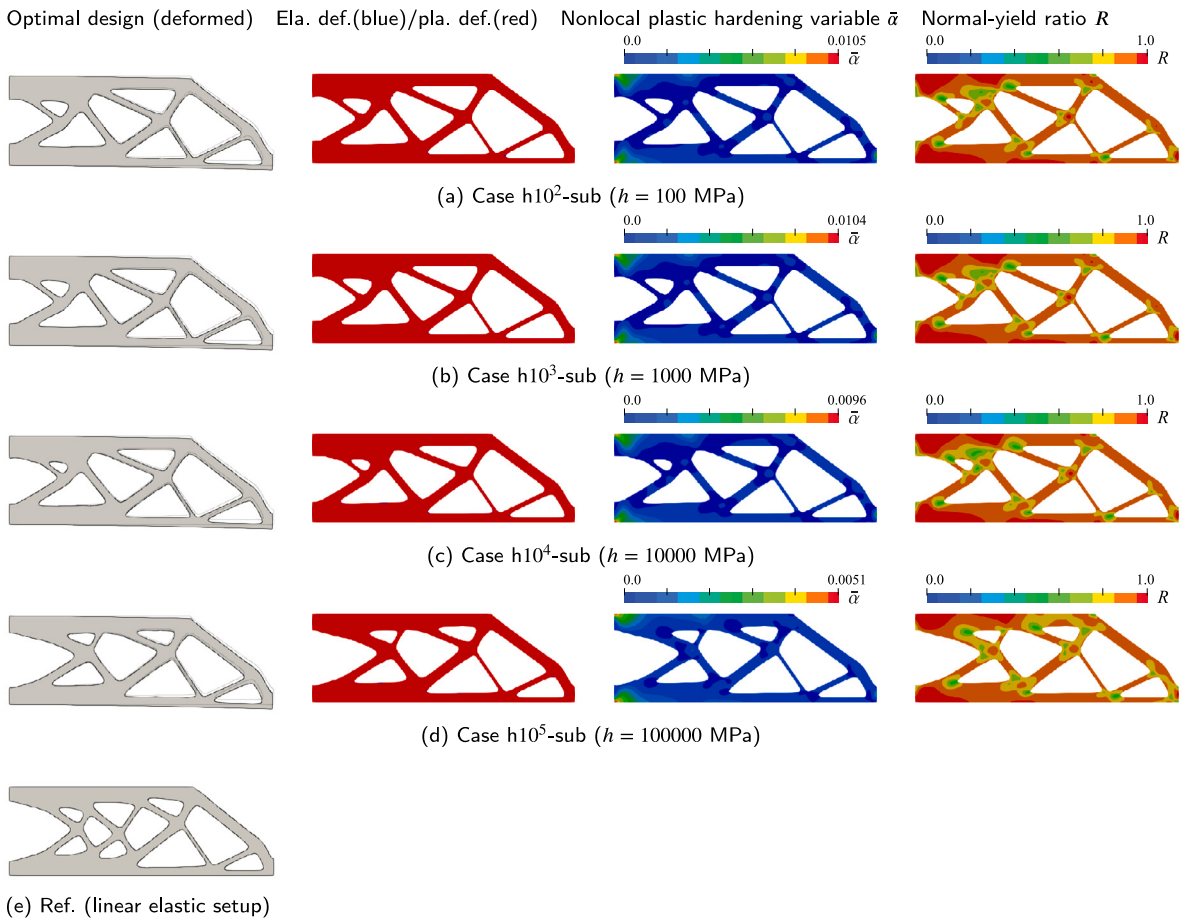


Fig. 9. Optimization results for Example 1: Subloading surface model. The region having  $\omega_1 \geq 0.5$  is displayed, and voids are not shown. Deformed configurations are also shown for all optimal designs.

a reference solution in panel (e). As can be seen from these figures, the optimal design in all cases exhibits plastic deformation throughout its entire region; see the second figure in each panel. Also, setting  $h_1$  larger allows for a milder accumulation of the nonlocal plastic hardening variable (plastic strain); compare the third figure in each panel of Fig. 9 and the reaction force–displacement curves in Fig. 8(e). Additionally, it can be confirmed from the fourth figure in each panel that the region of high stress concentration exhibits the material-specific plastic deformation associated with hardening ( $R \approx 1$ ). Furthermore, due to the geometrical nonlinearity considering finite strain and material nonlinearity in plasticity, the optimal designs in the current four cases do not resemble the reference solution; the current four cases tend to have thicker members than the reference solution. This is likely because the optimization process tries to avoid buckling, which causes undesirable plastic deformation and significantly reduces the stiffness of the cantilever.

**Remark 2.** This study derives the governing equations of the adjoint problem by considering the local plastic evolution is exclusively determined by the magnitude  $\gamma^p$  and direction  $\mathbf{n}$ . Thereby, as explained in Section 3.4, the primal and adjoint problems are solved in the same time direction from  $t = 0$  to  $t = T$ . It should be noted that this approach leads to small relative errors between the analytical and approximated sensitivities; one comparison is presented in Fig. 33 in Appendix C. Regarding this issue, Han et al. [60] recently made analytical and numerical investigations, and thus detailed explanation is not provided here.

#### 4.1.3. Parametric study on normal-yield threshold

As shown in Fig. 3(e), the normal-yield threshold  $R^c$  determines the range of the transition of deformation states. Thus, a parameter study of  $R_1^c$  with topology optimization is conducted in this subsection. The normal-yield saturation parameter  $R_1^p$  is set to 500, and the plastic hardening parameter  $h_1$  is set to 100 MPa. Fig. 10 shows the optimization error versus design iteration and the reaction force–displacement curves for the third three cases in Table 3 with different values of  $R_1^c$ , i.e., Cases Re03, Re05, and Re07.

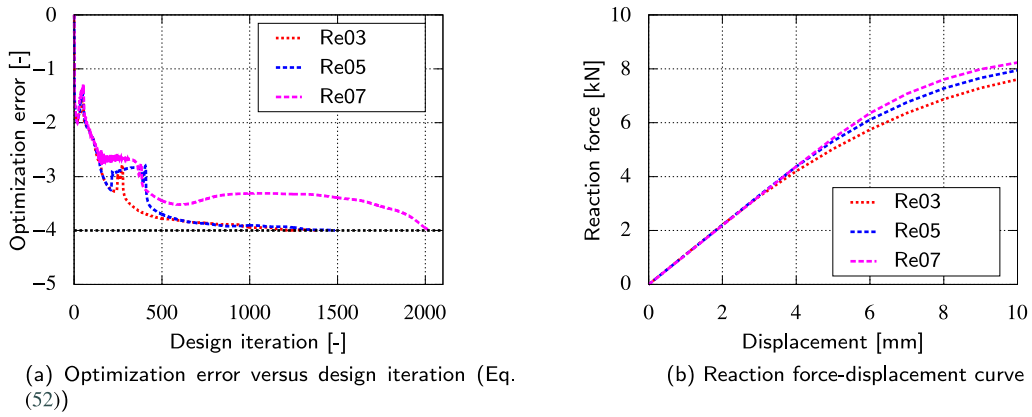


Fig. 10. Optimization error versus design iteration and reaction force–displacement curve for Example 1: Parametric study of the normal-yield threshold  $R_1^c$ . The black-colored line in (a) denotes the convergence tolerance “TOL”. (For interpretation of the references to color in this figure legend, the reader is referred to the web version of this article.)

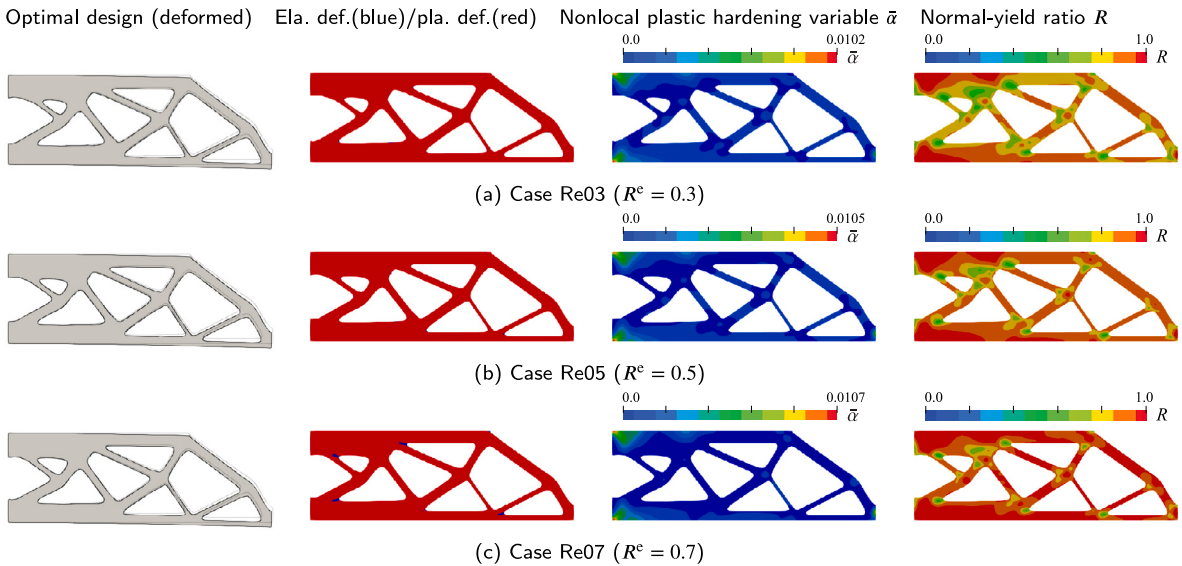


Fig. 11. Optimization results for Example 1: Parametric study of the normal-yield threshold  $R_1^c$ . The region having  $\omega_1 \geq 0.5$  is displayed, and voids are not shown. Deformed configurations are also shown for all optimal designs.

As shown in Fig. 10(a), oscillation is only observed at the beginning of the evolution of optimization error versus design iteration in Case Re07 but not in the remaining two cases. These responses are reasonable since the normal-yield threshold  $R_1^c$  determines the transition range from the complete elastic to plastic states; a small value of  $R_1^c$  leads to a wide transition range. That is, Case Re07 has the narrowest transition range, which may lead to oscillation to some extent. Also, it is found from the reaction force–displacement curves in Fig. 10(b) that the smaller the value of the normal yield threshold  $R_1^c$  is, the smaller the stiffness is. Additionally, for reference, the histories of the objective function for the current three cases are shown in Fig. 34(b) in Appendix C.

Meanwhile, Fig. 11 presents the optimal designs with distributions of deformation states, nonlocal plastic hardening variable, and normal-yield ratio for these three cases. As can be seen from the second figure in each panel, plastic deformation occurs in most regions, but in Case Re07, slight elastic deformation is also visible. Also, from the third figure, it is found that when the normal-yield threshold  $R_1^c$  is large, the accumulation of plastic strain that corresponds to the nonlocal hardening variable becomes significant for the same amount of deformation. This trend, on the other hand, affects the evolution of the normal-yield ratio  $R$ . In other words, the larger  $R_1^c$  is, the faster the evolution of plastic deformation becomes; see the fourth figure in each panel.

4.1.4. Parametric study on normal-yield saturation parameter

A parametric study of the normal-yield saturation parameter  $R^p$  is conducted. As demonstrated in Fig. 3(f),  $R^p$  changes the saturation behavior of the transition of deformation states, and giving a larger value of  $R^p$  recovers to the conventional plastic

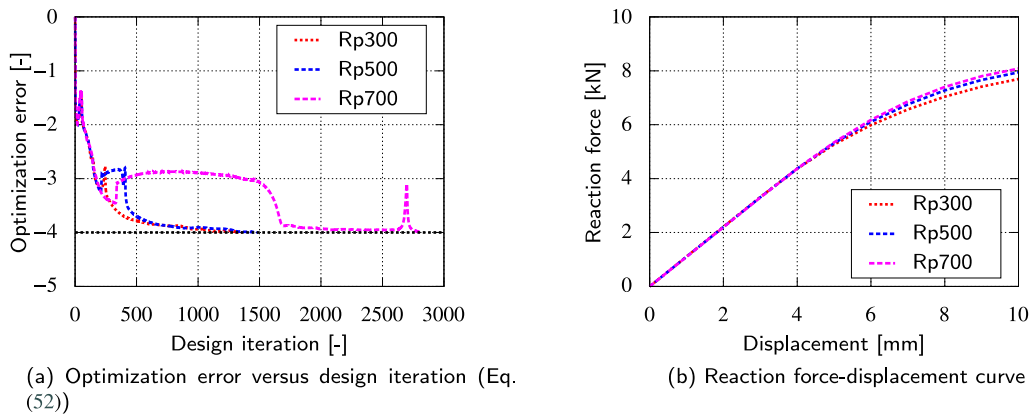


Fig. 12. Optimization error versus design iteration and reaction force–displacement curve for Example 1: Parametric study of the normal-yield saturation parameter  $R^p$ . The black-colored line in (a) denotes the convergence tolerance “TOL”.

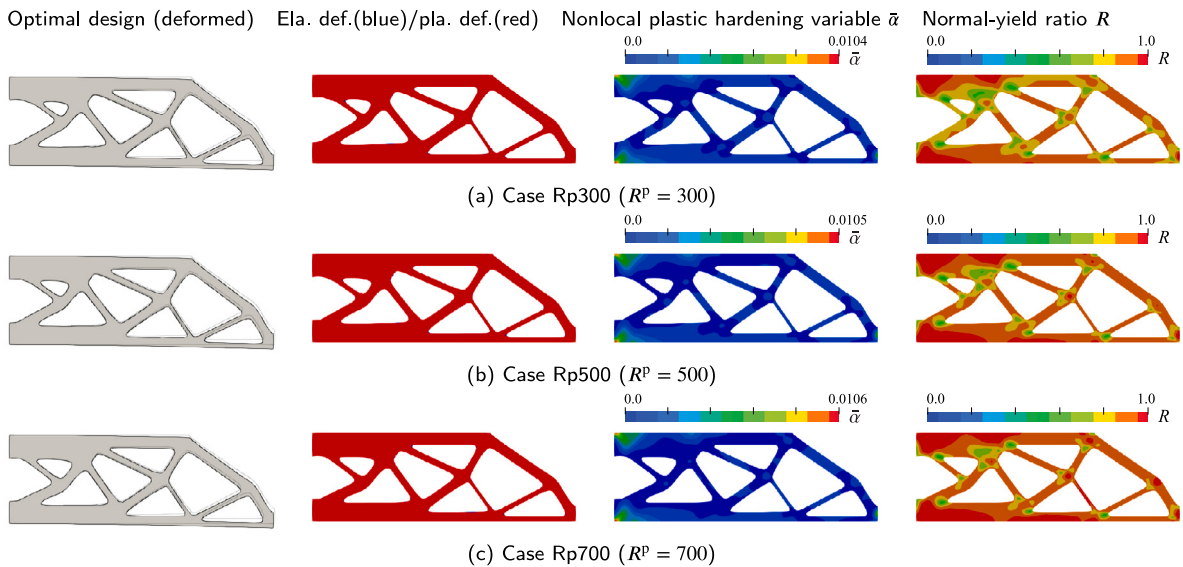


Fig. 13. Optimization results for Example 1: Parametric study of the normal-yield saturation parameter  $R^p$ . The region having  $\omega_1 \geq 0.5$  is displayed, and voids are not shown. Deformed configurations are also shown for all optimal designs.

model. The normal-yield threshold  $R_1^c$  is set to 0.5, and the plastic hardening parameter  $h_1$  is set to 100 MPa. Fig. 12 presents the optimization error versus design iteration and the reaction force–displacement curves for the last three cases in Table 3 with different values of  $R_1^p$ , i.e., Cases Rp300, Rp500, and Rp700.

Broadly speaking, a similar discussion to the previous parametric study can be made. That is, thanks to the characteristic of the subloading surface model, i.e., the smooth transition range between the complete elastic to plastic states, the optimization errors of the current three cases reach the tolerance “TOL”. without severe oscillations; see Fig. 12(a). On the other hand, the value of the normal-yield saturation parameter  $R_1^p$  affects the plastic hardening behavior, in which the stress increases during the elastic–plastic transition. However, since the normal-yield threshold is fixed, the transition range does not change, and the transition only speeds up when the normal-yield saturation parameter  $R_1^p$  is set to a large value; see Fig. 12(b) and also refer to Fig. 3(f). This trend can also be seen from Fig. 13, which shows the optimal designs with distributions of deformation states, nonlocal plastic hardening variable, and normal-yield ratio for the current five cases. In fact, it is found that when the normal-yield saturation parameter  $R_1^p$  is large, the accumulation of plastic strain that corresponds to the nonlocal hardening variable and the evolution of the normal-yield ratio is accelerated. For reference, the histories of the objective function for the current three cases are shown in Fig. 34(c) in Appendix C.

#### 4.2. Example 2: Multi-material topology optimization for a wedge specimen

The second example is for multi-material topology optimization (MMTO: topology optimization of one ersatz and  $m$  actual materials), for which a wedge-shaped specimen is subject to vertical deformation, as shown in Fig. 14. Different magnitudes of the

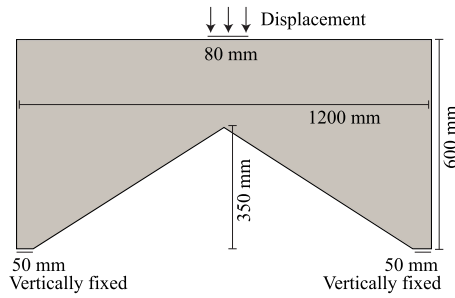


Fig. 14. Target design domain for Example 2: Geometry and boundary conditions (Meshsize: 6 mm).

Table 4  
Common material and optimization parameters for Example 2.

Material parameter		Value	Unit
Young's modulus	$E$	200 000	[MPa]
Poisson's ratio	$\nu$	0.3	[-]
Normal-yield threshold	$R^e$	0.5	[-]
Normal-yield saturation parameter	$R^p$	500	[-]
Optimization parameter		Value	Unit
Saturation parameter	$s_v$	10	[-]
Iteration number	$\bar{n}_{vol}$	50	[iter.]
Pseudo-time increment	$\Delta \bar{t}_{\beta}$	0.05	[s]
Diffusion coefficient	$l_{dl}^2$	6 <sup>2</sup>	[mm <sup>2</sup> ]
Convergence tolerance	TOL	10 <sup>-4</sup>	[-]

Table 5  
Plastic material parameters and allowance volume for Example 2: One-material topology optimization.

Parameter		Value	Unit
Initial yield stress	$y_{0,1}$	500	[MPa]
Linear hardening parameter	$h_1$	500	[MPa]
Nonlinear hardening parameter	$y_{\infty,1}$	1000	[MPa]
Saturation parameter	$s_{y,1}$	10	[-]
Penalty parameter	$l_{p,1}$	10 000	[MPa]
Diffusion parameter	$q_{p,1}$	72 000	[MPa mm <sup>2</sup> ]
Allowance volume	$V_{1,max}$	0.40	[-]

vertical deformation are given to the specimen, i.e., 5 mm, 20 mm, 35 mm, and 50 mm, in order to see the effects of geometrical and material nonlinearities on the optimal design. The common material and optimization parameters are listed in Table 4. Note that the Young's modulus and Poisson's ratios are the same for all actual materials, and the optimal designs are only determined by changing plastic material parameters. Thus, even if the stiffness maximization problem is discussed in this example, the optimization problem is different from conventional ones obtained only using elastic materials.

For convenience, the optimization cases discussed in this example are named by the following rule: "X" and "YY" of Case X-YY represent the number of actual materials and the magnitude of the prescribed displacement, respectively. For instance, Case 2-35 considers two actual materials and a prescribed displacement of 35 mm, respectively.

**Remark 3.** Indeed, larger displacement loadings, e.g., 65 mm, 80 mm, are possible, but the defects of materials should be newly taken into account by referring to damage evaluation criteria such as continuum damage models [61,62]. This is because several actual metallic materials exhibit material deterioration from  $\alpha \approx 0.1$ . Also, buckling behavior may appear due to low-density elements in the optimization process, and additional stabilization techniques [63,64] should be employed. Since the current magnitudes of deformation (5 mm~50 mm) can demonstrate the plastic deformation-dependent (or plastic strain-dependent) optimal designs, the afore-suggested issues are placed in our future studies.

#### 4.2.1. One-material topology optimization

Before tackling MMTO, one-material topology optimization is presented to show that the subloading surface model does not cause oscillations of the optimization error even for the structure targeted here. The plastic material parameters and allowance volume are listed in Table 5, and the stress-strain curve of the material is shown in Fig. 15. As can be seen, the stress-strain curve does not have a distinct yielding point to switch the deformation states from complete elastic to plastic ones, which is beneficial for the adjoint problem, as demonstrated in the previous example.

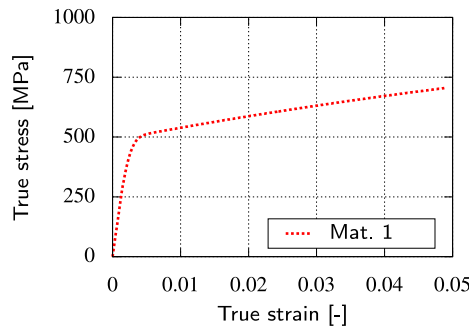
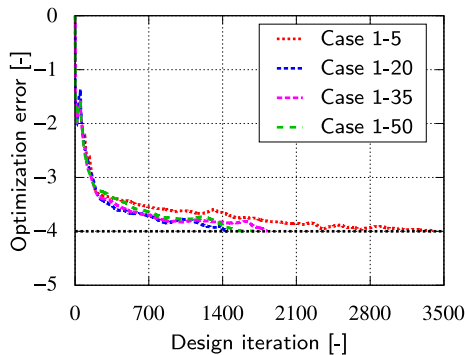
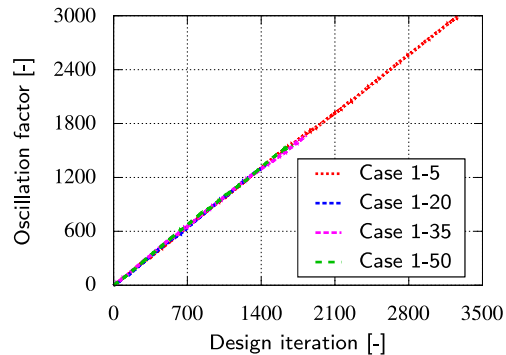


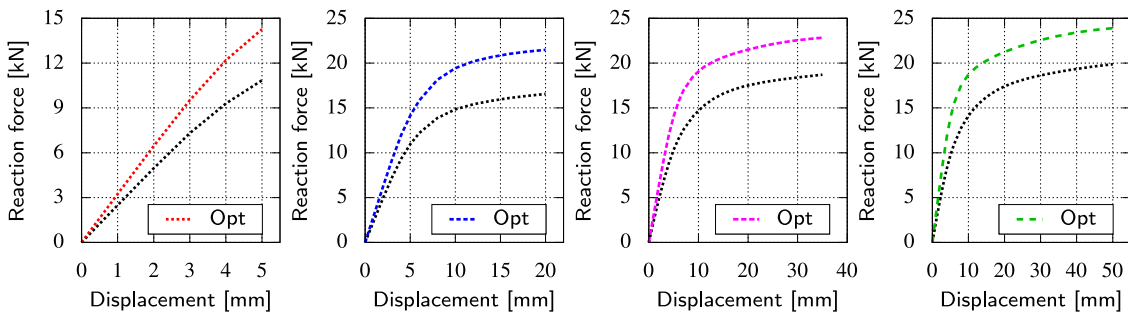
Fig. 15. True stress–true strain curve of base material for Example 2: One-material topology optimization.



(a) Optimization error versus design iteration (Eq. (52))



(b) Oscillation factor versus design iteration (Eq. (54))



(c) Reaction force–displacement curve (The black-colored dashed line is from the 50-th design iteration, and four panels are Case 1-5, Case 1-20, Case 1-35, and Case 1-50 from left to right.)

Fig. 16. Optimization error versus design iteration, oscillation factor versus design iteration, and reaction force–displacement curve for Example 2: One-material topology optimization. The black-colored line in (a) denotes the convergence tolerance “TOL”.

Figs. 16(a) and 16(b) show the optimization error and oscillation factor versus design iteration, respectively, of Case 1-5, Case 1-20, Case 1-35, and Case 1-50, where oscillation in optimization error is not observed. Also, the reaction force–displacement curves of the optimized design iteration are improved compared with those of the 50-th design iteration, at which the actual allowance volume is imposed; see Fig. 16(c).

Additionally, Fig. 17 shows the optimization results of the current four cases, where panel (e) is the reference solution obtained from the purely elastic setup. For reference, the non-binarized distribution of the design variable is shown in Fig. 37 in Appendix C. As can be seen from the middle figure in each panel of Fig. 17, plastic deformation occurs in all regions of the specimen in the remaining three cases except Case 1-5. In other words, the optimal designs are strongly affected by both geometric and material nonlinearities. In fact, as the prescribed deformation increases, the optimal design becomes less similar to the reference solution.

#### 4.2.2. Two-material topology optimization

Here, we address two-material topology optimization. The plastic material parameters and allowance volumes are presented in Table 6, and the stress–plastic hardening curves of base materials are shown in Fig. 18. As can be seen from the curves, the initial

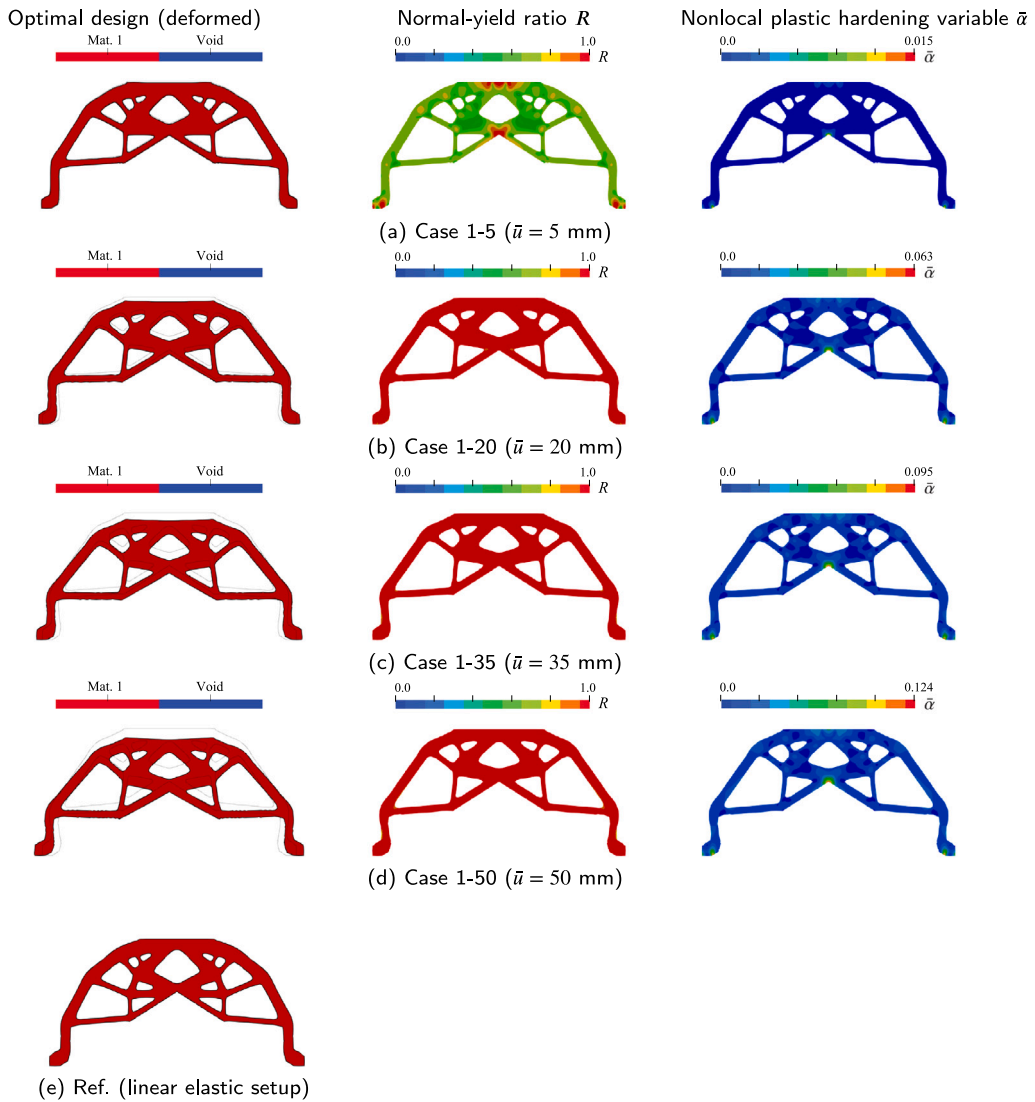


Fig. 17. Optimization results for Example 2: One-material topology optimization. The region having  $\omega_1 \geq 0.5$  is displayed, and voids are not shown. Deformed configurations are also shown for all optimal designs.

Table 6

Plastic material parameters and allowance volume for Example 2: Two-material topology optimization.

Parameter		Value	Unit
Initial yield stress	$Y_{0,1}, Y_{0,2}$	500, 200	[MPa]
Linear hardening parameter	$h_1, h_2$	500, 200	[MPa]
Nonlinear hardening parameter	$Y_{\infty,1}, Y_{\infty,2}$	1000, 3000	[MPa]
Saturation parameter	$s_{y,1}, s_{y,2}$	10, 10	[-]
Penalty parameter	$P_{p,1}, P_{p,2}$	10000, 4000	[MPa]
Diffusion parameter	$q_{p,1}, q_{p,2}$	72000, 28800	[MPa mm <sup>2</sup> ]
Allowance volume	$V_{1,max}, V_{2,max}$	0.20, 0.20	[-]

yield stress of Material 2 is less than that of Material 1, but Material 2 exhibits a stronger plastic hardening behavior. Accordingly, before and after the intersection (p1) of the two curves in Fig. 18, the preferred material should vary in terms of the stiffness maximization problem. That is if the plastic deformation at a certain location is small or large, Material 1 or Material 2 would be selectively placed, meaning that the switching criterion is (p1).

Figs. 19 and 20 present the reaction force–displacement curves and the optimization results of Case 2-5, Case 2-20, Case 2-35, and Case 2-50, respectively. For reference, the optimization error and oscillation factor versus design iteration are shown in Fig.

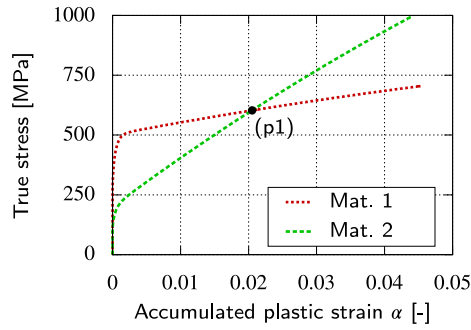


Fig. 18. True stress–accumulated plastic strain curve of base materials for Example 2: Two-material topology optimization.

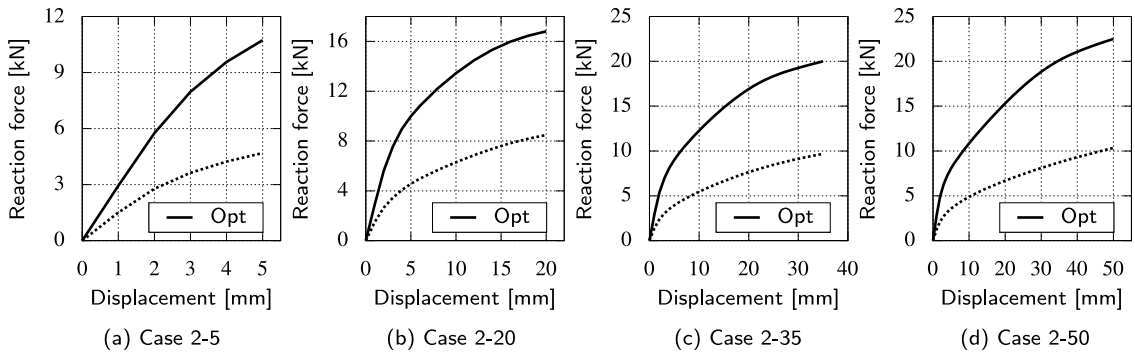


Fig. 19. Reaction force–displacement curve for Example 2: Two-material topology optimization. The black-colored dashed line in each panel is from the 50-th design iteration. (For interpretation of the references to color in this figure legend, the reader is referred to the web version of this article.)

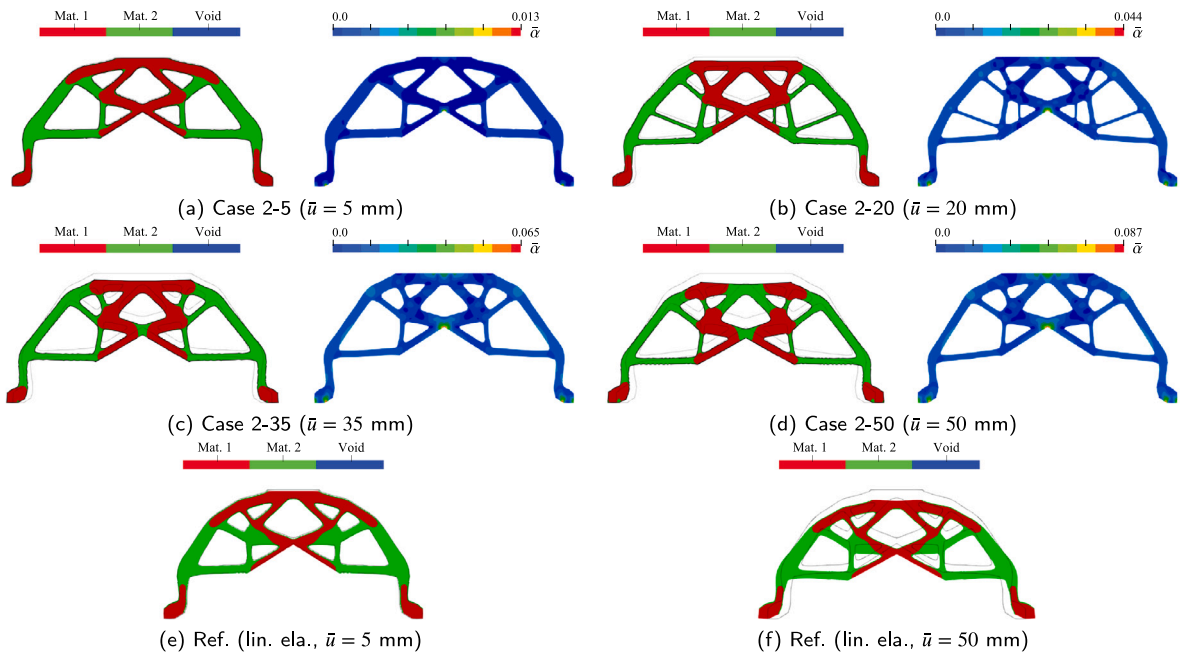


Fig. 20. Optimization results for Example 2: Two-material topology optimization. The left and right figures denote the distributions of the base materials and nonlocal plastic hardening variable. The region having  $\omega_2 \geq 0.5$  is displayed, and voids are not shown. Deformed configurations are also shown for all optimal designs.

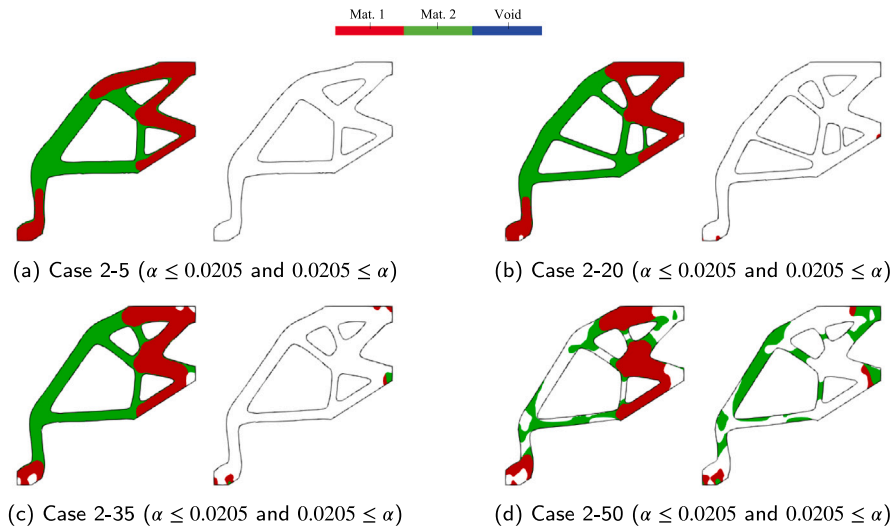


Fig. 21. Material distributions depending on the magnitude of the accumulated plastic strain  $\alpha$  for Example 2: Two-material topology optimization. Only half of each specimen is displayed. Also, see Fig. 18.

Table 7  
Plastic material parameters and allowance volume for Example 2: Three-material topology optimization.

Parameter		Value	Unit
Initial yield stress	$y_{0,1}, y_{0,2}, y_{0,3}$	500, 350, 200	[MPa]
Linear hardening parameter	$h_1, h_2, h_3$	500, 350, 200	[MPa]
Nonlinear hardening parameter	$y_{\infty,1}, y_{\infty,2}, y_{\infty,3}$	1000, 850, 3000	[MPa]
Saturation parameter	$s_{y,1}, s_{y,2}, s_{y,3}$	10, 10, 10	[-]
Penalty parameter	$p_{p,1}, p_{p,2}, p_{p,3}$	10000, 7000, 4000	[MPa]
Diffusion parameter	$q_{p,1}, q_{p,2}, q_{p,3}$	72000, 50400, 28800	[MPa mm <sup>2</sup> ]
Allowance volume	$V_{1,max}, V_{2,max}, V_{3,max}$	0.133, 0.133, 0.133	[-]

35(a) and Fig. 36(a) in Appendix C, respectively. As can be seen from Fig. 19, for all cases, the reaction force–displacement curves of the optimized design iteration are improved compared to those at the 50-th design iteration, at which the actual volume constraint is imposed by Eq. (49). Also, different optimal designs are obtained depending on the magnitude of the prescribed displacement; see the left figure in each panel of Fig. 20. For reference, the non-binarized distributions of the design variables,  $\omega_1$  and  $\omega_2$ , are shown in Fig. 38 in Appendix C. It should be noted that the material arrangement follows the material behavior in Fig. 18, and Material 2 is placed where large plastic deformation occurs as the prescribed displacement increases; e.g., see (d) in Fig. 20. This trend cannot be realized by the conventional elastic MMTO, for which Figs. 20(e) and (f) show the optimal designs. Here, only the linear elastic deformation is considered, and the Young’s modulus of Material 2 is half the value of the Young’s modulus of Material 1. As shown in these figures, Material 1 is placed where the stress concentration occurs regardless of the deformation magnitude. Notably, even if the finite strain elastic MMTO is conducted, Material 1 is still placed where the stress concentration occurs.

For further investigations, Fig. 21 is presented to show the material arrangement depending on the magnitude of plastic deformation. As can be seen from Fig. 18, the true stress of Material 2 becomes larger than that of Material 1 for the range approximately  $\alpha > 0.0205$ . Thus, in terms of the stiffness maximization problem, Material 2 should be selected for regions exhibiting stronger stress concentrations. This trend is indeed confirmed. That is, Material 2 is placed where the plastic hardening variable (accumulated plastic strain)  $\alpha$  is greater than 0.0205; see the right figure in each panel of Fig. 21. Also, this trend becomes more distinct along with the increase of the prescribed displacement. In fact, the middle part of the specimen is totally filled with Material 2 in Case 2-50.

#### 4.2.3. Three-material topology optimization

Subsequently, one material is added. That is, three-material topology optimization is discussed. The plastic material parameters and allowance volumes are summarized in Table 7, and the stress–strain curves of the base materials are shown in Fig. 22. This is a setting where the original and preferred materials are swapped at two points, (p2) and (p3), regarding the stiffness maximization problem. Specifically, when  $\alpha$  is smaller than 0.0098, the preferred material order is “Material 1, Material 2, and Material 3”. In the range  $0.0098 \leq \alpha \leq 0.0205$ , the order is “Material 1, Material 3, and Material 2”, and in the range  $0.0205 \leq \alpha$ , the order is “Material 3, Material 1, and Material 2”.

Fig. 23 shows the reaction force–displacement curves of Cases 3-5, 3-20, 3-35, and 3-50. As can be seen, the stiffness of the specimen is improved for all cases. For reference, the optimization error and oscillation factor for the design iterations are shown

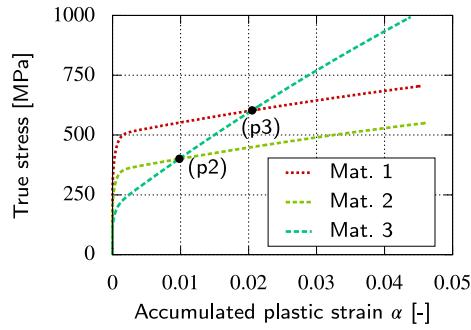


Fig. 22. True stress–accumulated plastic strain curve of base materials for Example 2: Three-material topology optimization.

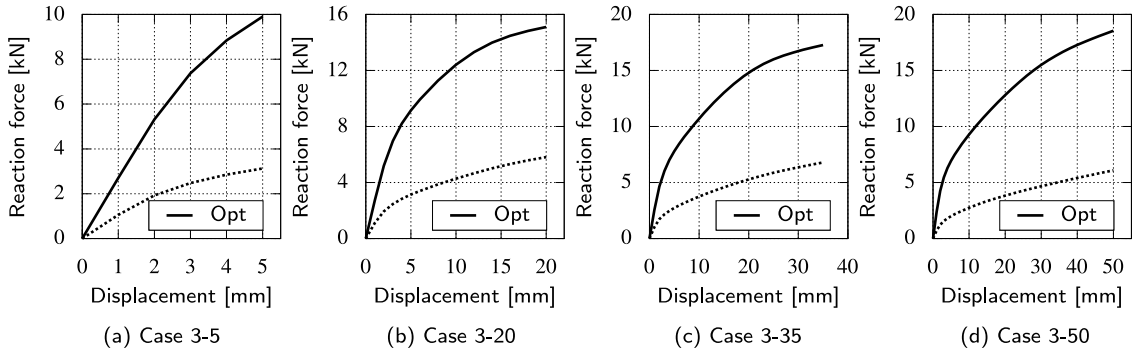


Fig. 23. Reaction force–displacement curve for Example 2: Three-material topology optimization. The black-colored dashed line in each panel is from the 50-th design iteration. (For interpretation of the references to color in this figure legend, the reader is referred to the web version of this article.)

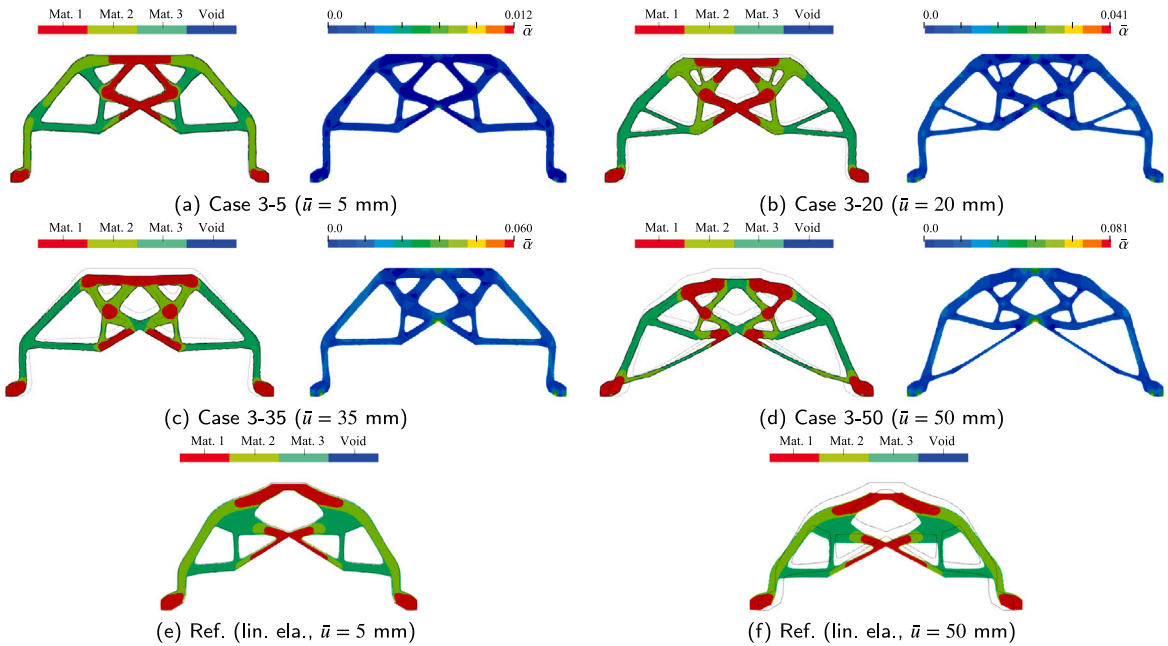


Fig. 24. Optimization results for Example 2: Three-material topology optimization. The left and right figures denote the distributions of the base materials and nonlocal plastic hardening variable. The region having  $\omega_3 \geq 0.5$  is displayed, and voids are not shown. Deformed configurations are also shown for all optimal designs.

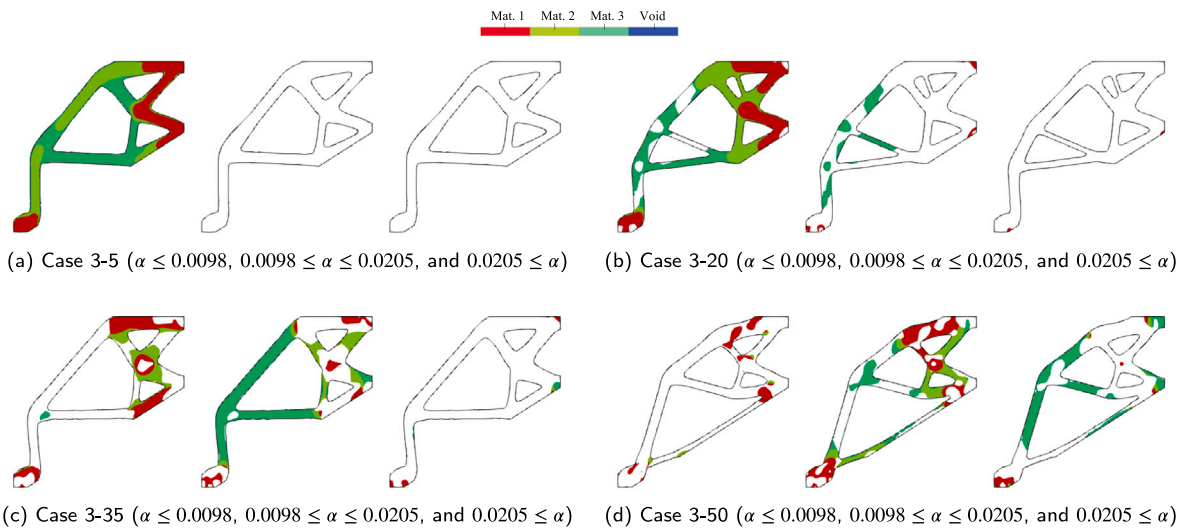


Fig. 25. Material distributions depending on the magnitude of plastic hardening variable  $\alpha$  for Example 2: Three-material topology optimization. Only half of each specimen is displayed. Also, see Fig. 22.

Table 8

Plastic material parameters and allowance volume for Example 2: Four-material topology optimization.

Parameter		Value	Unit
Initial yield stress	$Y_{0,1}, Y_{0,2}, Y_{0,3}, Y_{0,4}$	500, 400, 300, 200	[MPa]
Linear hardening parameter	$h_1, h_2, h_3, h_4$	500, 400, 300, 200	[MPa]
Nonlinear hardening parameter	$Y_{\infty,1}, Y_{\infty,2}, Y_{\infty,3}, Y_{\infty,4}$	1000, 900, 800, 3000	[MPa]
Saturation parameter	$S_{y,1}, S_{y,2}, S_{y,3}, S_{y,4}$	10, 10, 10, 10	[-]
Penalty parameter	$p_{p,1}, p_{p,2}, p_{p,3}, p_{p,4}$	10000, 8000, 6000, 4000	[MPa]
Diffusion parameter	$q_{p,1}, q_{p,2}, q_{p,3}, q_{p,4}$	72000, 57600, 43200, 28800	[MPa mm <sup>2</sup> ]
Allowance volume	$V_{1,max}, V_{2,max}, V_{3,max}, V_{4,max}$	0.1, 0.1, 0.1, 0.1	[-]

in Figs. 35(b) and 36(b) in Appendix C, respectively. On the other hand, Fig. 24 shows the optimization results of these four cases, in which figures (e) and (f) show the reference solutions obtained from the linear elastic MMTO with  $E_2 = 2/3E_1$  and  $E_3 = 1/3E_1$ . As can be seen, different optimal topologies are obtained for the proposed elastoplastic MMTO, whereas the optimal designs do not change with different displacement magnitudes for the linear elastic MMTO. In addition to the geometry of the optimal structure, the material distribution is also strongly affected by the accumulation of plastic strain. To be specific, Material 3 is placed in regions that exhibit large plastic deformation. To support this investigation, Fig. 25 is useful for understanding of the material arrangements determined by the magnitude of plastic deformation. For reference, the non-binarized distributions of the design variables  $\omega_1 \sim \omega_3$  are presented in Fig. 39. As explained in Section 4.2.3, in the conventional elastic MMTO, a material having a large Young’s modulus is placed where the stress concentration occurs to address the stiffness maximization problem. Hence, the material distribution does not change by the deformation magnitude. In contrast, in the proposed elastoplastic MMTO, the plastic hardening properties are referred to in the stiffness maximization problem. Thus, the optimal structure is unique on the imposed deformation magnitude.

#### 4.2.4. Four-material topology optimization

Finally, one additional material is added, and four-material topology optimization is discussed. The plastic material parameters and allowance volumes are presented in Table 8, and the stress–strain curves of the base materials, optimization error–design iteration curves, and reaction force–displacement curves are shown in Fig. 26. As can be seen, this is a setting where the original and preferred materials are swapped at three points, (p4), (p5), and (p6), in the figure in terms of the stiffness maximization problem. For instance, the preferred material order is “Material 1, Material 4, Material 2, and Material 3” between the points (p5) and (p6).

Fig. 27 shows the reaction force–displacement curves of Cases 4-5, 4-20, 4-35, and 4-50. As can be seen, the peak reaction forces are improved for all cases. For reference, the convergence trends of these cases are shown in Figs. 35(c) and 36(c) in Appendix C. The obtained optimal topologies are shown in Fig. 28 along with the distributions of the base materials and nonlocal plastic hardening variable, in which figures (e) and (f) show the reference solutions obtained from the linear elastic MMTO with  $E_2 = 3/4E_1$ ,  $E_3 = 2/4E_1$ , and  $E_4 = 1/4E_1$ . As in the previous examples, the material distribution varies with the magnitude of plastic deformation in terms of the stiffness maximization problem. This trend can be clearly observed from Fig. 29 that shows the material arrangements determined by the magnitude of plastic deformation. In particular, Material 4 tends to be placed where stress concentration occurs. However, it should be noted that this trend does not apply to the conventional elastic MMTO in figures (e) and (f) since the material

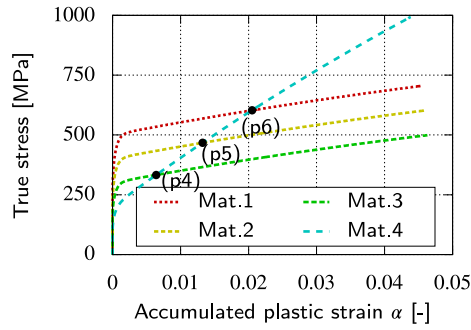


Fig. 26. True stress–accumulated plastic strain curve of base materials for Example 2: Four-material topology optimization.

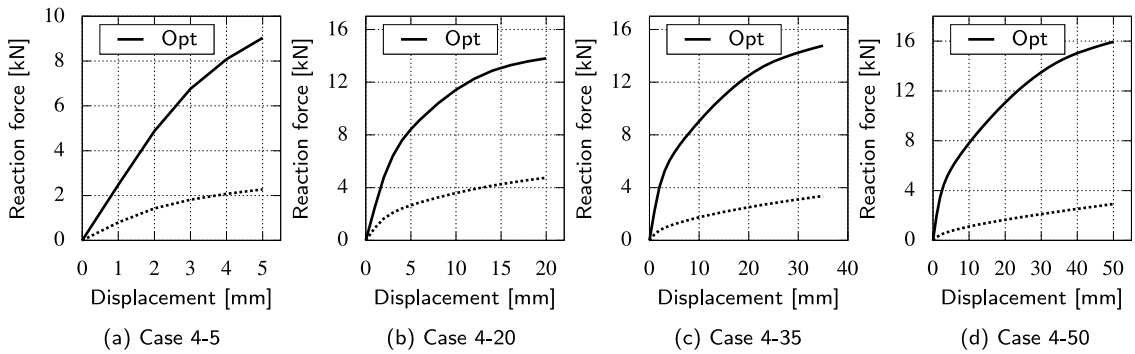


Fig. 27. Reaction force–displacement curve for Example 2: Four-material topology optimization. The black-colored dashed line in each panel is from the 50-th design iteration.

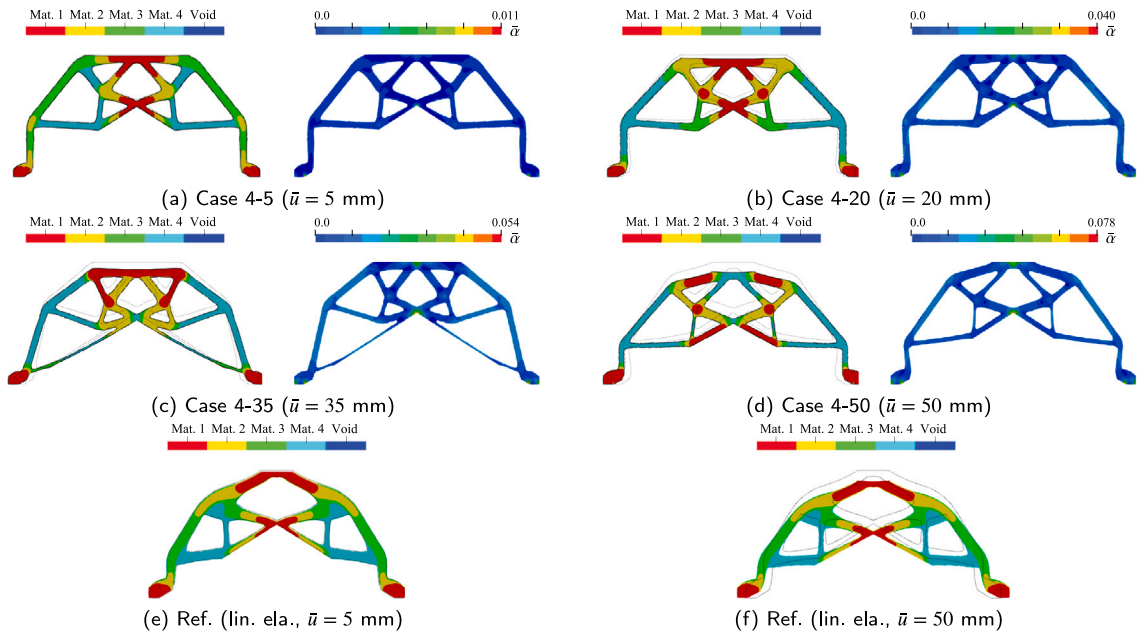


Fig. 28. Optimization results for Example 2: Four-material topology optimization. The left and right figures denote the distributions of the base materials and nonlocal plastic hardening variable. The region having  $\omega_3 \geq 0.5$  is displayed, and voids are not shown. Deformed configurations are also shown for all optimal designs.

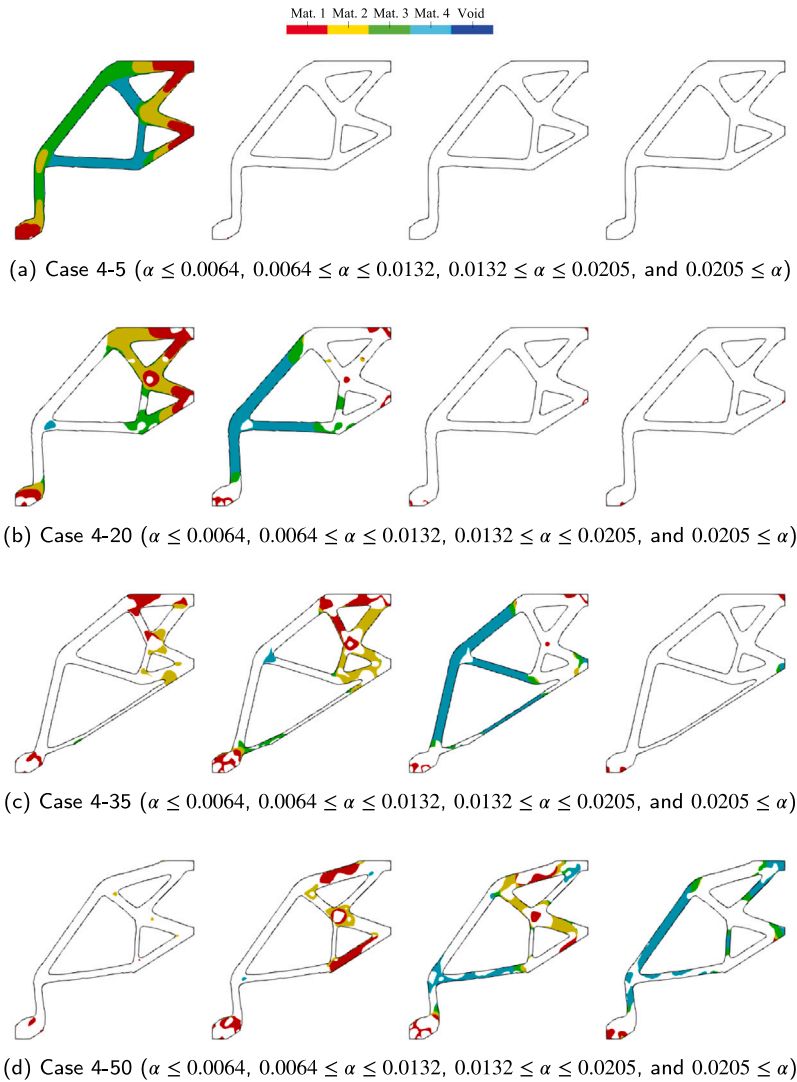


Fig. 29. Material distributions depending on the magnitude of plastic hardening variable  $\alpha$  for Example 2: Four-material topology optimization. Only half of each specimen is displayed. Also, see Fig. 26.

distributions are exclusively determined by the values of Young’s moduli of base materials, which are not related to the deformation magnitude.

Before closing this subsection, a few shortcomings of MMTO as formulated in this study should be mentioned. Comparing the optimal designs of Case 4-5 and Case 4-50 in Fig. 28, we notice that Case 4-50 has thinner members than Case 4-5. This is because the optimal design of Case 4-50 is more “grayscale” pronounced than in Case 4-5; see also Fig. 40 in Appendix C for reference. The main reason for the pronounced grayscale can be due to the SIMP-based interpolation method in Eq. (9). Precisely, the employed function is continuous and cannot represent discrete material distributions, even though the order “ $p$ ” in Eq. (9) works as penalization to avoid intermediate material densities. It should also be noted that the SIMP-based interpolation function has a “nested structure”. That is, the  $k$ th material is less likely to be selected than  $k + 1$ -th material since the material distribution is determined by the design variable  $\omega_k$ . On the other hand, it is also strongly affected by the design variables  $\{\omega_{k+1}, \omega_{k+2}, \dots, \omega_m\}$ . Accordingly, obtaining proper material distribution may not be guaranteed. For instance, when the accumulated plastic strain  $\alpha$  is larger than 0.0205, the appropriate material order should be Material 4, Material 1, Material 2, and Material 3. However, as can be seen in the last figure in Fig. 29(d), Material 2 and Material 3 have larger areas than Material 1. Nevertheless, such a discrepancy is common for SIMP-based interpolation, and a similar discussion can be found in the literature. Therefore, it is safe to conclude that

**Table 9**

Objective functions and numerical comparisons for Example 2. ObjX denotes the value of objective function obtained from X-th base material. ObjX/Obj indicates the ratio of ObjX to Obj as a percentage.

Disp. [mm]	Obj [J]	Obj1 [J]	Obj2 [J]	Obj3 [J]	Obj4 [J]	Obj1/Obj	Obj2/Obj	Obj3/Obj	Obj4/Obj
Case 2-5 ( $\bar{u} = 5$ )	130.3	143.7	97.7			110%	75%		
Case 2-50 ( $\bar{u} = 50$ )	24747.8	26066.1	25009.3			105%	101%		
Disp. [mm]	Obj [J]	Obj1 [J]	Obj2 [J]	Obj3 [J]	Obj4 [J]	Obj1/Obj	Obj2/Obj	Obj3/Obj	Obj4/Obj
Case 3-5 ( $\bar{u} = 5$ )	120.4	133.6	114.4	90.4		111%	95%	75%	
Case 3-50 ( $\bar{u} = 50$ )	20421.3	22041.3	16686.1	21109.5		108%	82%	103%	
Disp. [mm]	Obj [J]	Obj1 [J]	Obj2 [J]	Obj3 [J]	Obj4 [J]	Obj1/Obj	Obj2/Obj	Obj3/Obj	Obj4/Obj
Case 4-5 ( $\bar{u} = 5$ )	110.0	122.6	112.3	96.0	83.0	111%	102%	87%	75%
Case 4-50 ( $\bar{u} = 50$ )	17685.6	18913.7	15876.9	12787.4	18215.4	107%	90%	72%	103%

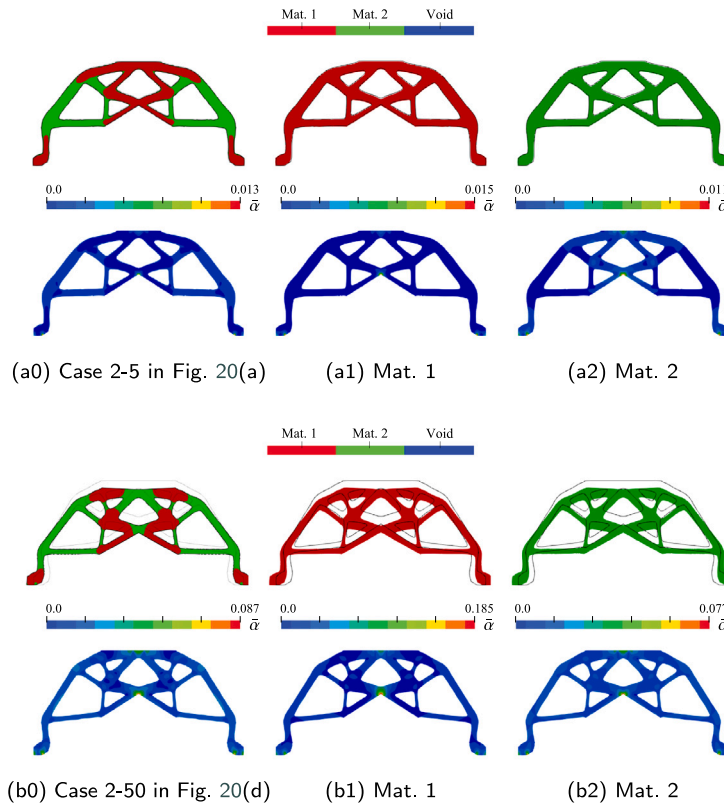


**Fig. 30.** Deformed configurations and distributions of the nonlocal plastic hardening variable of the optimal structures and structures made from base materials for Example 2: Two-material topology optimization in Section 4.2.2.

apart from the issues related to interpolation functions, the proposed framework is promising in terms of the MMTO considering finite strain nonlocal elastoplasticity.

**4.2.5. Discussion**

As discussed above, the proposed MMTO method can realize the optimal material configuration and distribution according to the magnitude of imposed displacement; see Figs. 21, 25, and 29. Before closing this numerical example, we furthermore provide overall discussions on the optimization results by referring to the smallest and largest deformation cases (5 mm and 50 mm).

Now, the optimal structures obtained from the two, three, and four-material topology optimizations are re-constructed by the base materials (Mat. 1~ Mat. 4). Then, the values of the objective functions are calculated given the prescribed deformations of 5 mm and 50 mm, and those values are summarized in Table 9. Here, “ObjX” denotes the objective function obtained from X-th base material, e.g., “Obj3 = 96.0 [J]” for Case 4-5 is calculated from the optimal shape of Case 4-5 in Fig. 28(d) that is, however, made from Mat. 3. Also, “ObjX/Obj” indicates the ratio of ObjX to Obj as a percentage. As shown in the table, for the cases with the small deformation (5 mm), since the yield stress is higher in the order of Mat. 1, Mat. 2, Mat. 3, and Mat. 4, the values of the objective function “ObjX” are also larger in that order; also refer to Figs. 18, 22, and 26. Therefore, it is desirable to use only Mat. 1

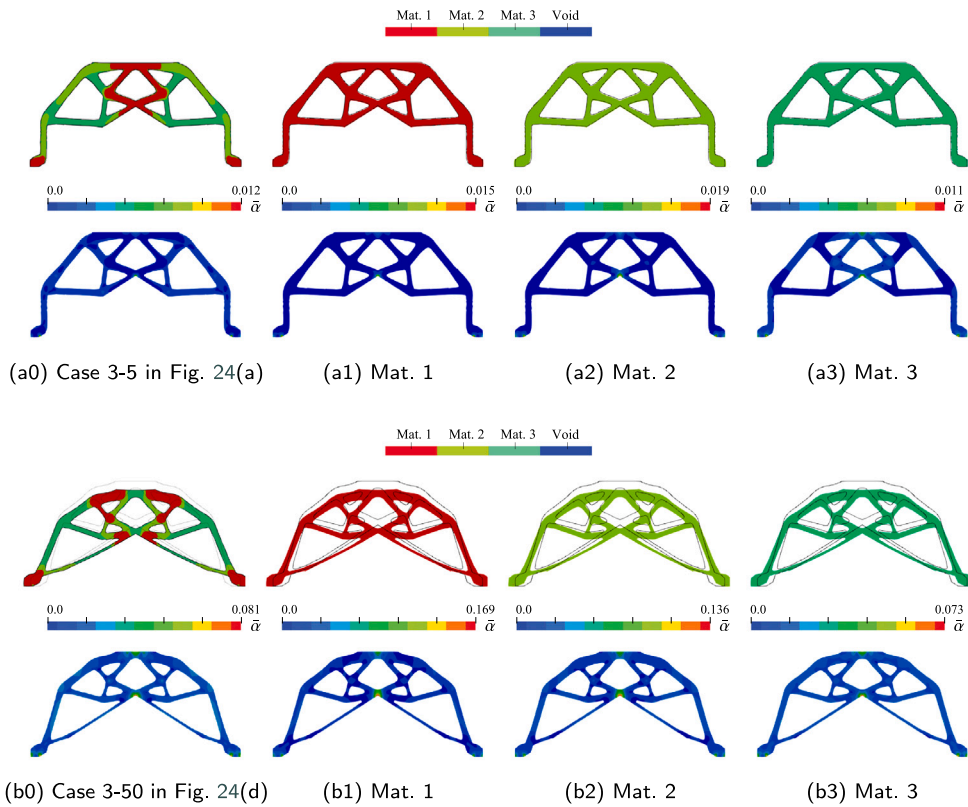


Fig. 31. Deformed configurations and distributions of the nonlocal plastic hardening variable of the optimal structures and structures made from base materials for Example 2: Three-material topology optimization in Section 4.2.3.

to manufacture the strongest wedge specimen, but in actual manufacturing, it is not always possible to use as much of one material as desired. Then, one advantage of MMTOs is that if we can combine several materials (e.g., strong and weak materials, expensive and cheap materials) to find the optimal shape, this situation may be avoided, and the resulting optimal structure may still fulfill the design objective. In fact, although only 1/2, 1/3, and 1/4 of Mat. 1 is used in the optimal designs, the values of “Obj1” in Table 9 for the cases with  $\bar{u} = 5$  mm are just slightly larger than the values of “Obj”, i.e., the optimal structure itself is not so weak, despite the use of weaker materials. However, it should be noted that the optimal structures obtained from MMTO are used here, and thus, the values of the objective function calculated for the structures represented by a single base material are not equal to those obtained when optimizing with a single material.

Meanwhile, as shown in Table 9, when the large deformation (50 mm) is considered, Mat. 2 in Case 2-50, Mat. 3 in Case 3-50, and Mat. 4 in Case 4-50 are no more the weakest material. This is because they exhibit the largest plastic hardening behavior among base materials in each MMTO in Sections 4.2.2, 4.2.3, and 4.2.4; also refer to Figs. 18, 22, and 26. In short, if they can be placed where high-stress concentrations occur, weakness of low yield stress is offset by its high plastic hardening behavior, and the best performance can be achieved. For a better understanding, Figs. 30–32 present deformed configurations and distributions of the nonlocal plastic hardening variable  $\bar{\alpha}$ . As can be seen from these figures, Mat. 2 in Case 2-50, Mat. 3 in Case 3-50, and Mat. 4 in Case 4-50 exhibit the smallest plastic accumulations among base materials, which implies the plastic dissipation rate ( $\nu_0 \dot{\alpha}$ ) is also the smallest. Also, it turns out that the magnitudes of the nonlocal plastic hardening variable  $\bar{\alpha}$  in the figures (b0) are closest to those in figure (b2) in Fig. 30, figure (b3) in Fig. 31, and figure (b4) in 32. This can be said to be a reasonable realization of stiffness optimization, i.e., finding a structure that resists external forces as much as possible. Notably, the optimal material configuration and distribution should change once the plastic dissipation problem is alternatively involved in the objective function; readers can refer to Han et al. [33,35] for several investigations within the single-design variable topology optimization. Since the current study is enough to explain the ability of the proposed elastoplastic MMTO, additional investigations will be included in our future studies.

## 5. Conclusion

This study has developed a new multi-material topology optimization (MMTO) formulation incorporated with finite strain nonlocal elastoplasticity. A distinctive novelty is the incorporation of the subloading surface model into the primal problem to achieve the gradual change from pure elastic deformation state to fully plastic deformation state. Also, the idea of interpolating

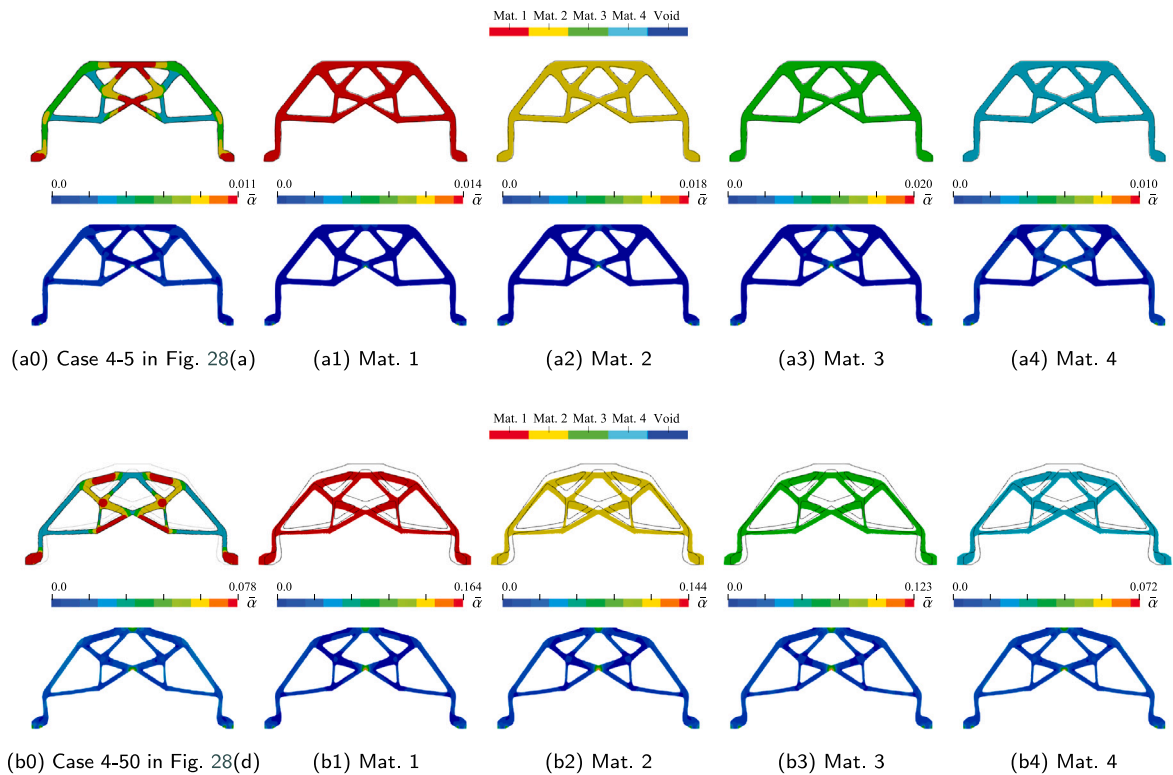


Fig. 32. Deformed configurations and distributions of the nonlocal plastic hardening variable of the optimal structures and structures made from base materials for Example 2: Four-material topology optimization in Section 4.2.4.

energy densities was employed to ensure computational stability and to avoid unrealistic plastic deformation occurring in voids (ersatz material). In addition, for the first time, the continuous adjoint method was formulated to derive the governing equations and sensitivity of the adjoint problem of MMTO considering elastoplasticity. Accordingly, the obtained equations do not depend on any discretization and are valid at any location in a continuum body, on its boundary, and at any moment. An arbitrary number of design variables was considered in the formulation, and by referring to the derived sensitivity, the multiple reaction–diffusion equations were introduced to update the material distribution and configuration. In the first numerical example, the capability of the subloading surface model is investigated. In particular, the stable optimization process is realized by employing the feature of the material Jacobians in the subloading surface model continuous functions. In the second numerical example, several topology optimization problems were solved for multiple materials with the same elasticity but different plastic material properties. In particular, we were able to illustrate that the distribution of base materials within the optimum structure changes with the magnitude of plastic deformation by setting the stresses in the base materials to switch between large and small during the hardening process. Note that although no example was given, the mesh-dependency problem has been solved by the application of nonlocal plasticity theory.

We conclude this paper with a discussion of future directions. First, for better MMTO, the material interpolation function should be reconsidered. To the best of the authors’ knowledge, if we have an interpolation method that does not have the “nested structure” like the employed SIMP-based function, even if the number of base materials increases, it is expected that the grayscale can be mitigated, and the proper material order can be achieved. Second, the idea of interpolating energy densities is extended to describe MMTO for different types of material combinations, such as rubbers, concretes, metals, and so on. This direction should be especially helpful when discussing the optimal geometry and location of fibers for composite materials or the optimal placement and amount of rebars for reinforced concrete. Third, if MMTO can take into account the damage of several base materials in a multi-material structure, it is expected that a new optimal design that controls or takes advantage of their fracture behavior will be realized. If this kind of optimization is established, the failure behavior of products can be “pre-designed” while keeping the desired capability, and thus, the industry can save a lot of resources for actual experiments to investigate the failure behavior. These topics are left for our future challenges.

## CRediT authorship contribution statement

**Jike Han:** Writing – review & editing, Writing – original draft, Visualization, Software, Methodology, Investigation, Formal analysis, Data curation, Conceptualization. **Yuki Yamakawa:** Writing – review & editing, Validation, Software, Methodology. **Kazuhiro Izui:** Writing – review & editing, Supervision, Resources, Project administration, Funding acquisition. **Shinji Nishiwaki:** Writing – review & editing, Supervision, Resources, Project administration, Investigation, Funding acquisition, Conceptualization. **Kenjiro Terada:** Writing – review & editing, Supervision, Software, Resources, Project administration, Methodology, Funding acquisition, Conceptualization.

## Declaration of competing interest

The authors declare that they have no known competing financial interests or personal relationships that could have appeared to influence the work reported in this paper.

## Acknowledgments

This work was supported by JSPS KAKENHI, Japan Grant Numbers JP22K18755 and JP25K17528. In this research work we used the supercomputer of ACCMS, Kyoto University.

## Appendix A. Supplemental information for the interpolation of multiple material parameters

### A.1. Examples of the SIMP-based interpolation function

Suppose one material parameter “•” is determined by  $m+1 = 2$ ,  $m+1 = 3$ , or  $m+1 = 4$  base material parameters, Eq. (9) recovers to

$$\begin{aligned} \bullet &= \bullet_{1,2} = \omega_1^p \bullet_1 + (1 - \omega_1^p) \bullet_2, \\ \bullet &= \bullet_{1,2,3} = \omega_2^p \bullet_{1,2} + (1 - \omega_2^p) \bullet_3 = \omega_2^p \omega_1^p \bullet_1 + \omega_2^p (1 - \omega_1^p) \bullet_2 + (1 - \omega_2^p) \bullet_3, \\ \bullet &= \bullet_{1,2,3,4} = \omega_3^p \bullet_{1,2,3} + (1 - \omega_3^p) \bullet_4 = \omega_3^p \omega_2^p \omega_1^p \bullet_1 + \omega_3^p \omega_2^p (1 - \omega_1^p) \bullet_2 + \omega_3^p (1 - \omega_2^p) \bullet_3 + (1 - \omega_3^p) \bullet_4. \end{aligned} \quad (56)$$

### A.2. Supplemental explanation for Fig. 2

As shown in Fig. 2, the domain filled with Material 1 is calculated by

$$V_1 = \int_{D_0} (\omega_1 \omega_2 \omega_3) dV. \quad (57)$$

On the other hand, the domain calculated by  $\int_{D_0} (\omega_2 \omega_3) dV$  covers both domains A and C, the former of which is  $V_1$ . Thus, the domain filled with Material 2 is calculated by

$$V_2 = \int_{D_0} (\omega_2 \omega_3) dV - V_1 = \int_{D_0} (\omega_2 \omega_3) dV - \int_{D_0} (\omega_1 \omega_2 \omega_3) dV. \quad (58)$$

Similarly, the domain filled with Material 3 is calculated by

$$V_3 = \int_{D_0} (\omega_3) dV - V_1 - V_2 = \int_{D_0} (\omega_3) dV - \int_{D_0} (\omega_2 \omega_3) dV. \quad (59)$$

In this way, Eq. (19) can be obtained inductively.

### A.3. Derivatives of the volume constraints with respect to design variables

The derivatives of the volume constraints for multiple materials in Eq. (21) with respect to design variable  $\omega_i$  with  $i = 1, 2, \dots, m-1, m$  are calculated as follows:

$$\begin{aligned}
 \delta\omega_i \boldsymbol{\theta} \cdot \bar{\mathbf{V}} &= \frac{\partial}{\partial\omega_i} \left( \sum_{l=1}^m \theta_l \int_{D_0} \left( \prod_{k=l}^m \omega_k - \prod_{k=l-1}^m \omega_k \right) dV \right) \delta\omega_i \\
 &= \frac{\partial}{\partial\omega_i} \left( \theta_1 \int_{D_0} \left( \prod_{k=1}^m \omega_k - \prod_{k=0}^m \omega_k \right) dV + \theta_2 \int_{D_0} \left( \prod_{k=2}^m \omega_k - \prod_{k=1}^m \omega_k \right) dV + \dots \right. \\
 &\quad \left. + \theta_{i-1} \int_{D_0} \left( \prod_{k=i-1}^m \omega_k - \prod_{k=i-2}^m \omega_k \right) dV \right. \\
 &\quad \left. + \theta_i \int_{D_0} \left( \prod_{k=i}^m \omega_k - \prod_{k=i-1}^m \omega_k \right) dV + \theta_{i+1} \int_{D_0} \left( \prod_{k=i+1}^m \omega_k - \prod_{k=i}^m \omega_k \right) dV + \dots \right. \\
 &\quad \left. + \theta_{m-1} \int_{D_0} \left( \prod_{k=m-1}^m \omega_k - \prod_{k=m-2}^m \omega_k \right) dV + \theta_m \int_{D_0} \left( \prod_{k=m}^m \omega_k - \prod_{k=m-1}^m \omega_k \right) dV \right) \delta\omega_i \\
 &= \frac{\partial}{\partial\omega_i} \left( (\theta_1 - \theta_2) \int_{D_0} \prod_{k=1}^m \omega_k dV + (\theta_2 - \theta_3) \int_{D_0} \prod_{k=2}^m \omega_k dV + \dots \right. \\
 &\quad \left. + (\theta_{i-1} - \theta_i) \int_{D_0} \prod_{k=i-1}^m \omega_k dV + (\theta_i - \theta_{i+1}) \int_{D_0} \prod_{k=i}^m \omega_k dV \right) \delta\omega_i \\
 &= \sum_{l=1}^i (\theta_l - \theta_{l+1}) \int_{D_0} \frac{\partial}{\partial\omega_i} \prod_{k=l}^m \omega_k dV \delta\omega_i = \sum_{l=1}^i (\theta_l - \theta_{l+1}) \int_{D_0} \frac{1}{\omega_i} \prod_{k=l}^m \omega_k \delta\omega_i dV.
 \end{aligned} \tag{60}$$

## Appendix B. Components for numerical implementation

### B.1. Components for the primal problem

The integrand in Eq. (38)<sub>3</sub> is expanded as

$$\begin{aligned}
 &\frac{\partial P_{ia,n}}{\partial F_{jb}} + \frac{\partial P_{ia,n}}{\partial \gamma^p} \frac{\partial \gamma_n^p}{\partial F_{jb}} + \frac{\partial P_{ia,n}}{\partial \mathbf{n}_{cd}} \frac{\partial \mathbf{n}_{cd,n}}{\partial F_{jb}} \\
 &= \frac{\partial \tau_{ic,n}}{\partial b_{ef}^e} \left( \frac{\partial b_{ef,n}^e}{\partial F_{jb}} + \frac{\partial b_{ef,n}^e}{\partial \gamma^p} \frac{\partial \gamma_n^p}{\partial F_{jb}} + \frac{\partial b_{ef,n}^e}{\partial \mathbf{n}_{gh}} \frac{\partial \mathbf{n}_{gh,n}}{\partial F_{jb}} \right) F_{ac,n}^{-1} - \tau_{ic,n} F_{aj,n}^{-1} F_{bc,n}^{-1}, \\
 &\frac{\partial \tau_{ic,n}}{\partial b_{ef}^e} = \frac{\partial \tau_{vol,ic,n}}{\partial b_{ef}^e} + \frac{\partial \tau_{dev,ic,n}}{\partial b_{ef}^e} = \frac{\kappa}{2} J^{e2} \delta_{ic} b_{ef,n}^{e-1} + \mu J^{e-2/3} \left( \mathbf{1}_{dev,icef} - \frac{1}{3} b_{dev,ic,n}^e b_{ef,n}^{e-1} \right).
 \end{aligned} \tag{61}$$

Here, the superscript ‘‘h’’ representing the FE approximation is omitted for convenience. Also, the derivatives of  $b^e$  with respect to  $F$ ,  $\gamma^p$ , and  $\mathbf{n}$  in Eq. (61) are calculated by

$$\begin{aligned}
 \frac{\partial b_n^e}{\partial \mathbf{F}} &= \exp(-2\Delta t_n \gamma_n^p \mathbf{n}_n) \otimes \left( \mathbf{C}_{n-1}^{p-1} \cdot \mathbf{F}_n^T \right)^T + \left\{ \exp(-2\Delta t_n \gamma_n^p \mathbf{n}_n) \cdot \mathbf{F}_n \cdot \mathbf{C}_{n-1}^{p-1} \right\} \otimes \mathbf{1}, \\
 \frac{\partial b_n^e}{\partial \gamma^p} &= \left\{ D \exp(-2\Delta t_n \gamma_n^p \mathbf{n}_n) : (-2\Delta t_n \mathbf{n}_n) \right\} \cdot \mathbf{b}_n^{e,tr}, \\
 \frac{\partial b_n^e}{\partial \mathbf{n}} &= \underbrace{\left\{ D \exp(-2\Delta t_n \gamma_n^p \mathbf{n}_n) : (-2\Delta t_n \gamma_n^p \mathbf{1}_{sym}) \right\}}_{iakl} * \underbrace{\mathbf{b}_n^{e,tr}}_{aj},
 \end{aligned} \tag{62}$$

in which  $\otimes$  is the dyadic-down product operator, i.e.,  $(\mathbf{1} \otimes \mathbf{1})_{ijkl} = \delta_{il} \delta_{jk}$ , and  $*$  denotes the tensor product operator to realize the above suggested manipulation, respectively.

The derivatives  $\partial_F \gamma_n^p$  and  $\partial_F \mathbf{n}_n$  can be calculated from Eq. (39). To be specific, the following relationships hold:

$$\begin{aligned}
 \frac{\partial \mathcal{R}_{\gamma^p,n}^g}{\partial \mathbf{F}} &= \mathcal{K}_{\gamma^p \gamma^p,n} \frac{\partial \gamma_n^p}{\partial \mathbf{F}} + \mathcal{K}_{\gamma^p \mathbf{n},n} : \frac{\partial \mathbf{n}_n}{\partial \mathbf{F}}, \\
 \frac{\partial \mathcal{R}_{\mathbf{n},n}^g}{\partial \mathbf{F}} &= \mathcal{K}_{\mathbf{n} \gamma^p,n} \otimes \frac{\partial \gamma_n^p}{\partial \mathbf{F}} + \mathcal{K}_{\mathbf{n} \mathbf{n},n} : \frac{\partial \mathbf{n}_n}{\partial \mathbf{F}},
 \end{aligned} \tag{63}$$

where

$$\frac{\partial \mathcal{R}_{\gamma^p, n}^g}{\partial \mathbf{F}} = -\frac{\partial \|\boldsymbol{\tau}_{\text{dev}, n}\|}{\partial \mathbf{F}} = -\frac{\partial \|\boldsymbol{\tau}_{\text{dev}, n}\|}{\partial \mathbf{b}^e} : \underbrace{\frac{\partial \mathbf{b}_n^e}{\partial \mathbf{F}}}_{\text{Eq. (62)}_1}, \quad (64)$$

$$\frac{\partial \mathcal{R}_{\mathbf{n}, n}^g}{\partial \mathbf{F}} = \frac{\partial}{\partial \mathbf{F}} \frac{\boldsymbol{\tau}_{\text{dev}, n}}{\|\boldsymbol{\tau}_{\text{dev}, n}\|} = \left( \frac{1}{\|\boldsymbol{\tau}_{\text{dev}, n}\|} \frac{\partial \boldsymbol{\tau}_{\text{dev}, n}}{\partial \mathbf{b}^e} - \frac{\boldsymbol{\tau}_{\text{dev}, n}}{\|\boldsymbol{\tau}_{\text{dev}, n}\|^2} \otimes \frac{\partial \|\boldsymbol{\tau}_{\text{dev}, n}\|}{\partial \mathbf{b}^e} \right) : \underbrace{\frac{\partial \mathbf{b}_n^e}{\partial \mathbf{F}}}_{\text{Eq. (62)}_1}.$$

Thus, recalling the relationship  $\mathbf{n} = \mathbf{n}^T$ ,  $\partial_{\mathbf{F}} \gamma_n^p$  and  $\partial_{\mathbf{F}} \mathbf{n}_n$  are obtained from

$$\frac{\partial \boldsymbol{\xi}_n}{\partial \mathbf{F}} = \mathbf{K}_{\text{local}, n}^{\text{primal-1}} \cdot \frac{\partial \mathcal{R}_{\boldsymbol{\xi}, n}^g}{\partial \mathbf{F}}, \quad (65)$$

where

$$\frac{\partial \boldsymbol{\xi}_n}{\partial \mathbf{F}} = \left[ \frac{\partial \gamma_n^p}{\partial \mathbf{F}} \quad \frac{\partial n_{11, n}}{\partial \mathbf{F}} \quad \frac{\partial n_{22, n}}{\partial \mathbf{F}} \quad \frac{\partial n_{33, n}}{\partial \mathbf{F}} \quad \frac{\partial n_{23, n}}{\partial \mathbf{F}} \quad \frac{\partial n_{13, n}}{\partial \mathbf{F}} \quad \frac{\partial n_{12, n}}{\partial \mathbf{F}} \right]^T, \quad (66)$$

$$\frac{\partial \mathcal{R}_{\boldsymbol{\xi}, n}^g}{\partial \mathbf{F}} = \left[ \frac{\partial \mathcal{R}_{\gamma^p, n}^g}{\partial \mathbf{F}} \quad \frac{\partial \mathcal{R}_{n_{11}, n}^g}{\partial \mathbf{F}} \quad \frac{\partial \mathcal{R}_{n_{22}, n}^g}{\partial \mathbf{F}} \quad \frac{\partial \mathcal{R}_{n_{33}, n}^g}{\partial \mathbf{F}} \quad 2 \frac{\partial \mathcal{R}_{n_{23}, n}^g}{\partial \mathbf{F}} \quad 2 \frac{\partial \mathcal{R}_{n_{13}, n}^g}{\partial \mathbf{F}} \quad 2 \frac{\partial \mathcal{R}_{n_{12}, n}^g}{\partial \mathbf{F}} \right]^T,$$

and

$$\mathbf{K}_{\text{local}, n}^{\text{primal}} = \begin{bmatrix} \mathcal{K}_{\gamma^p \gamma^p, n} & \mathcal{K}_{\gamma^p n_{11}, n} & \mathcal{K}_{\gamma^p n_{22}, n} & \mathcal{K}_{\gamma^p n_{33}, n} & 2\mathcal{K}_{\gamma^p n_{23}, n} & 2\mathcal{K}_{\gamma^p n_{13}, n} & 2\mathcal{K}_{\gamma^p n_{12}, n} \\ \mathcal{K}_{n_{11} \gamma^p, n} & \mathcal{K}_{n_{11} n_{11}, n} & \mathcal{K}_{n_{11} n_{22}, n} & \mathcal{K}_{n_{11} n_{33}, n} & 2\mathcal{K}_{n_{11} n_{23}, n} & 2\mathcal{K}_{n_{11} n_{13}, n} & 2\mathcal{K}_{n_{11} n_{12}, n} \\ \mathcal{K}_{n_{22} \gamma^p, n} & \mathcal{K}_{n_{22} n_{11}, n} & \mathcal{K}_{n_{22} n_{22}, n} & \mathcal{K}_{n_{22} n_{33}, n} & 2\mathcal{K}_{n_{22} n_{23}, n} & 2\mathcal{K}_{n_{22} n_{13}, n} & 2\mathcal{K}_{n_{22} n_{12}, n} \\ \mathcal{K}_{n_{33} \gamma^p, n} & \mathcal{K}_{n_{33} n_{11}, n} & \mathcal{K}_{n_{33} n_{22}, n} & \mathcal{K}_{n_{33} n_{33}, n} & 2\mathcal{K}_{n_{33} n_{23}, n} & 2\mathcal{K}_{n_{33} n_{13}, n} & 2\mathcal{K}_{n_{33} n_{12}, n} \\ 2\mathcal{K}_{n_{23} \gamma^p, n} & 2\mathcal{K}_{n_{23} n_{11}, n} & 2\mathcal{K}_{n_{23} n_{22}, n} & 2\mathcal{K}_{n_{23} n_{33}, n} & 4\mathcal{K}_{n_{23} n_{23}, n} & 4\mathcal{K}_{n_{23} n_{13}, n} & 4\mathcal{K}_{n_{23} n_{12}, n} \\ 2\mathcal{K}_{n_{13} \gamma^p, n} & 2\mathcal{K}_{n_{13} n_{11}, n} & 2\mathcal{K}_{n_{13} n_{22}, n} & 2\mathcal{K}_{n_{13} n_{33}, n} & 4\mathcal{K}_{n_{13} n_{23}, n} & 4\mathcal{K}_{n_{13} n_{13}, n} & 4\mathcal{K}_{n_{13} n_{12}, n} \\ 2\mathcal{K}_{n_{12} \gamma^p, n} & 2\mathcal{K}_{n_{12} n_{11}, n} & 2\mathcal{K}_{n_{12} n_{22}, n} & 2\mathcal{K}_{n_{12} n_{33}, n} & 4\mathcal{K}_{n_{12} n_{23}, n} & 4\mathcal{K}_{n_{12} n_{13}, n} & 4\mathcal{K}_{n_{12} n_{12}, n} \end{bmatrix}. \quad (67)$$

Similarly, the derivatives  $\partial_{\bar{\alpha}} \gamma_n^p$  and  $\partial_{\bar{\alpha}} \mathbf{n}_n$  can be calculated from Eq. (39), and the following relationships hold:

$$\frac{\partial \mathcal{R}_{\gamma^p, n}^g}{\partial \bar{\alpha}} = \mathcal{K}_{\gamma^p \gamma^p, n} \frac{\partial \gamma_n^p}{\partial \bar{\alpha}} + \mathcal{K}_{\gamma^p \mathbf{n}, n} : \frac{\partial \mathbf{n}_n}{\partial \bar{\alpha}}, \quad (68)$$

$$\frac{\partial \mathcal{R}_{\mathbf{n}, n}^g}{\partial \bar{\alpha}} = \mathcal{K}_{\mathbf{n} \gamma^p, n} \frac{\partial \gamma_n^p}{\partial \bar{\alpha}} + \mathbf{K}_{\mathbf{n} \mathbf{n}, n} : \frac{\partial \mathbf{n}_n}{\partial \bar{\alpha}},$$

where

$$\frac{\partial \mathcal{R}_{\gamma^p, n}^g}{\partial \bar{\alpha}} = R_n \sqrt{\frac{2}{3}} \frac{\partial r_n^p}{\partial \bar{\alpha}} = -R_n \sqrt{\frac{2}{3}} p^p, \quad \frac{\partial \mathcal{R}_{\mathbf{n}, n}^g}{\partial \bar{\alpha}} = \mathbf{0}. \quad (69)$$

Thus,  $\partial_{\bar{\alpha}} \gamma_n^p$  and  $\partial_{\bar{\alpha}} \mathbf{n}_n$  are obtained as

$$\frac{\partial \boldsymbol{\xi}_n}{\partial \bar{\alpha}} = \mathbf{K}_{\text{local}, n}^{\text{primal-1}} \cdot \frac{\partial \mathcal{R}_{\boldsymbol{\xi}, n}^g}{\partial \bar{\alpha}}, \quad (70)$$

where

$$\frac{\partial \boldsymbol{\xi}_n}{\partial \bar{\alpha}} = \left[ \frac{\partial \gamma_n^p}{\partial \bar{\alpha}} \quad \frac{\partial n_{11, n}}{\partial \bar{\alpha}} \quad \frac{\partial n_{22, n}}{\partial \bar{\alpha}} \quad \frac{\partial n_{33, n}}{\partial \bar{\alpha}} \quad \frac{\partial n_{23, n}}{\partial \bar{\alpha}} \quad \frac{\partial n_{13, n}}{\partial \bar{\alpha}} \quad \frac{\partial n_{12, n}}{\partial \bar{\alpha}} \right]^T, \quad (71)$$

$$\frac{\partial \mathcal{R}_{\boldsymbol{\xi}, n}^g}{\partial \bar{\alpha}} = \left[ \frac{\partial \mathcal{R}_{\gamma^p, n}^g}{\partial \bar{\alpha}} \quad \frac{\partial \mathcal{R}_{n_{11}, n}^g}{\partial \bar{\alpha}} \quad \frac{\partial \mathcal{R}_{n_{22}, n}^g}{\partial \bar{\alpha}} \quad \frac{\partial \mathcal{R}_{n_{33}, n}^g}{\partial \bar{\alpha}} \quad 2 \frac{\partial \mathcal{R}_{n_{23}, n}^g}{\partial \bar{\alpha}} \quad 2 \frac{\partial \mathcal{R}_{n_{13}, n}^g}{\partial \bar{\alpha}} \quad 2 \frac{\partial \mathcal{R}_{n_{12}, n}^g}{\partial \bar{\alpha}} \right]^T.$$

### B.2. Components for the adjoint problem

Eq. (28)<sub>4,5</sub> can be modified as follows:

$$\frac{\partial f_{B_0, n}}{\partial \gamma^p} + \mathbf{h}_n : \omega_m^p \frac{\partial \boldsymbol{\tau}_n}{\partial \gamma^p} - \eta_n^p \omega_m^p \left( \frac{\partial \|\boldsymbol{\tau}_{\text{dev}, n}\|}{\partial \gamma^p} - \sqrt{\frac{2}{3}} \left( \frac{\partial R_n}{\partial \gamma^p} (y_0 + r_n^p) + R_n \frac{\partial r_n^p}{\partial \gamma^p} \right) \right) + \boldsymbol{\pi}_n : \omega_m^p \frac{\partial}{\partial \gamma^p} \frac{\boldsymbol{\tau}_{\text{dev}, n}}{\|\boldsymbol{\tau}_{\text{dev}, n}\|} - \omega_m^p p_p \bar{\beta}_n \frac{\partial \alpha_n}{\partial \gamma^p} = 0, \quad (92)$$

$$\frac{\partial f_{B_0, n}}{\partial \mathbf{n}} + \mathbf{h}_n : \omega_m^p \frac{\partial \boldsymbol{\tau}_n}{\partial \mathbf{n}} - \eta_n^p \omega_m^p \frac{\partial \|\boldsymbol{\tau}_{\text{dev}, n}\|}{\partial \mathbf{n}} - \boldsymbol{\pi}_n : \omega_m^p \left( \mathbf{1} \otimes \mathbf{1} - \frac{\partial}{\partial \mathbf{n}} \frac{\boldsymbol{\tau}_{\text{dev}, n}}{\|\boldsymbol{\tau}_{\text{dev}, n}\|} \right) = \mathbf{0} \quad \text{with } \mathbf{h}_n = \frac{\partial \mathbf{w}_n}{\partial \mathbf{x}}.$$

Then, from Eqs. (43) and (72), the following relationships hold:

$$\begin{aligned} \frac{\partial \mathcal{R}_{\eta^p, n}^g}{\partial \mathbf{h}} &= \mathcal{K}_{\eta^p \eta^p, n} \frac{\partial \eta_n^p}{\partial \mathbf{h}} + \mathcal{K}_{\eta^p \pi, n} : \frac{\partial \pi_n}{\partial \mathbf{h}}, \\ \frac{\partial \mathcal{R}_{\pi, n}^g}{\partial \mathbf{h}} &= \mathcal{K}_{\pi \eta^p, n} \otimes \frac{\partial \eta_n^p}{\partial \mathbf{h}} + \underline{\mathcal{K}}_{\pi \pi, n} : \frac{\partial \pi_n}{\partial \mathbf{h}}, \end{aligned} \quad (73)$$

where

$$\frac{\partial \mathcal{R}_{\eta^p, n}^g}{\partial \mathbf{h}} = -\omega_m^p \frac{\partial \tau_n}{\partial \gamma^p}, \quad \frac{\partial \mathcal{R}_{\pi, n}^g}{\partial \mathbf{h}} = -\omega_m^p \frac{\partial \tau_n}{\partial \mathbf{n}}. \quad (74)$$

Accordingly,  $\partial_{\mathbf{h}} \eta_n^p$  and  $\partial_{\mathbf{h}} \pi_n$  are calculated from

$$\frac{\partial \tilde{\xi}_n}{\partial \mathbf{h}} = \mathcal{K}_{\text{local}, n}^{\text{adjoint-1}} \cdot \frac{\partial \mathcal{R}_{\tilde{\xi}, n}^g}{\partial \mathbf{h}}, \quad (75)$$

where

$$\begin{aligned} \frac{\partial \tilde{\xi}_n}{\partial \mathbf{h}} &= \left[ \frac{\partial \eta_n^p}{\partial \mathbf{h}} \quad \frac{\partial \pi_{11, n}}{\partial \mathbf{h}} \quad \frac{\partial \pi_{22, n}}{\partial \mathbf{h}} \quad \frac{\partial \pi_{33, n}}{\partial \mathbf{h}} \quad \frac{\partial \pi_{23, n}}{\partial \mathbf{h}} \quad \frac{\partial \pi_{13, n}}{\partial \mathbf{h}} \quad \frac{\partial \pi_{12, n}}{\partial \mathbf{h}} \right]^T, \\ \frac{\partial \mathcal{R}_{\tilde{\xi}, n}^g}{\partial \mathbf{h}} &= \left[ \frac{\partial \mathcal{R}_{\eta^p, n}^g}{\partial \mathbf{h}} \quad \frac{\partial \mathcal{R}_{\pi_{11}, n}^g}{\partial \mathbf{h}} \quad \frac{\partial \mathcal{R}_{\pi_{22}, n}^g}{\partial \mathbf{h}} \quad \frac{\partial \mathcal{R}_{\pi_{33}, n}^g}{\partial \mathbf{h}} \quad 2 \frac{\partial \mathcal{R}_{\pi_{23}, n}^g}{\partial \mathbf{h}} \quad 2 \frac{\partial \mathcal{R}_{\pi_{13}, n}^g}{\partial \mathbf{h}} \quad 2 \frac{\partial \mathcal{R}_{\pi_{12}, n}^g}{\partial \mathbf{h}} \right]^T, \end{aligned} \quad (76)$$

and

$$\mathcal{K}_{\text{local}, n}^{\text{adjoint}} = \begin{bmatrix} \mathcal{K}_{\eta^p, n} & \mathcal{K}_{\eta^p \pi_{11}, n} & \mathcal{K}_{\eta^p \pi_{22}, n} & \mathcal{K}_{\eta^p \pi_{33}, n} & 2\mathcal{K}_{\eta^p \pi_{23}, n} & 2\mathcal{K}_{\eta^p \pi_{13}, n} & 2\mathcal{K}_{\eta^p \pi_{12}, n} \\ \mathcal{K}_{\pi_{11} \eta^p, n} & \mathcal{K}_{\pi_{11} \pi_{11}, n} & \mathcal{K}_{\pi_{11} \pi_{22}, n} & \mathcal{K}_{\pi_{11} \pi_{33}, n} & 2\mathcal{K}_{\pi_{11} \pi_{23}, n} & 2\mathcal{K}_{\pi_{11} \pi_{13}, n} & 2\mathcal{K}_{\pi_{11} \pi_{12}, n} \\ \mathcal{K}_{\pi_{22} \eta^p, n} & \mathcal{K}_{\pi_{22} \pi_{11}, n} & \mathcal{K}_{\pi_{22} \pi_{22}, n} & \mathcal{K}_{\pi_{22} \pi_{33}, n} & 2\mathcal{K}_{\pi_{22} \pi_{23}, n} & 2\mathcal{K}_{\pi_{22} \pi_{13}, n} & 2\mathcal{K}_{\pi_{22} \pi_{12}, n} \\ \mathcal{K}_{\pi_{33} \eta^p, n} & \mathcal{K}_{\pi_{33} \pi_{11}, n} & \mathcal{K}_{\pi_{33} \pi_{22}, n} & \mathcal{K}_{\pi_{33} \pi_{33}, n} & 2\mathcal{K}_{\pi_{33} \pi_{23}, n} & 2\mathcal{K}_{\pi_{33} \pi_{13}, n} & 2\mathcal{K}_{\pi_{33} \pi_{12}, n} \\ 2\mathcal{K}_{\pi_{23} \eta^p, n} & 2\mathcal{K}_{\pi_{23} \pi_{11}, n} & 2\mathcal{K}_{\pi_{23} \pi_{22}, n} & 2\mathcal{K}_{\pi_{23} \pi_{33}, n} & 4\mathcal{K}_{\pi_{23} \pi_{23}, n} & 4\mathcal{K}_{\pi_{23} \pi_{13}, n} & 4\mathcal{K}_{\pi_{23} \pi_{12}, n} \\ 2\mathcal{K}_{\pi_{13} \eta^p, n} & 2\mathcal{K}_{\pi_{13} \pi_{11}, n} & 2\mathcal{K}_{\pi_{13} \pi_{22}, n} & 2\mathcal{K}_{\pi_{13} \pi_{33}, n} & 4\mathcal{K}_{\pi_{13} \pi_{23}, n} & 4\mathcal{K}_{\pi_{13} \pi_{13}, n} & 4\mathcal{K}_{\pi_{13} \pi_{12}, n} \\ 2\mathcal{K}_{\pi_{12} \eta^p, n} & 2\mathcal{K}_{\pi_{12} \pi_{11}, n} & 2\mathcal{K}_{\pi_{12} \pi_{22}, n} & 2\mathcal{K}_{\pi_{12} \pi_{33}, n} & 4\mathcal{K}_{\pi_{12} \pi_{23}, n} & 4\mathcal{K}_{\pi_{12} \pi_{13}, n} & 4\mathcal{K}_{\pi_{12} \pi_{12}, n} \end{bmatrix}. \quad (77)$$

Thus,  $\partial_{\mathbf{H}} \eta_n^p$  and  $\partial_{\mathbf{H}} \pi_n$  in Eq. (42) are calculated from the following relationship:

$$\frac{\partial \eta_n^p}{\partial \mathbf{H}} = \frac{\partial \eta_n^p}{\partial \mathbf{h}} \cdot \mathbf{F}_n^{-T}, \quad \frac{\partial \pi_n}{\partial \mathbf{H}} = \frac{\partial \pi_n}{\partial \mathbf{h}} \cdot \mathbf{F}_n^{-T}. \quad (78)$$

Meanwhile, from Eq. (43), the following relationship is written:

$$\begin{aligned} \frac{\partial \mathcal{R}_{\eta^p, n}^g}{\partial \beta} &= \mathcal{K}_{\eta^p \eta^p, n} \frac{\partial \eta_n^p}{\partial \beta} + \mathcal{K}_{\eta^p \pi, n} : \frac{\partial \pi_n}{\partial \beta}, \\ \frac{\partial \mathcal{R}_{\pi, n}^g}{\partial \beta} &= \mathcal{K}_{\pi \eta^p, n} \frac{\partial \eta_n^p}{\partial \beta} + \underline{\mathcal{K}}_{\pi \pi, n} : \frac{\partial \pi_n}{\partial \beta}, \end{aligned} \quad (79)$$

where

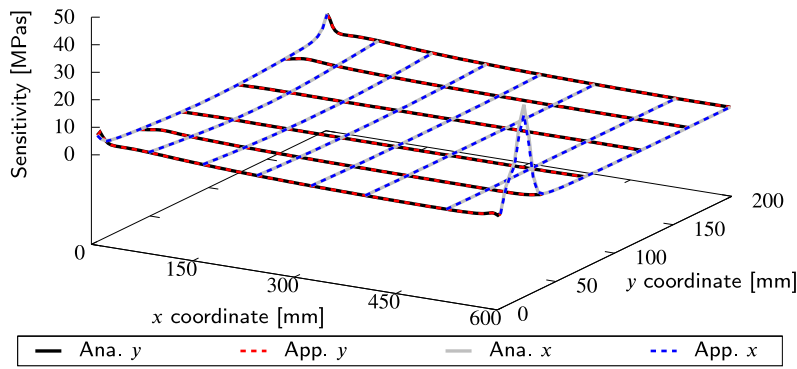
$$\frac{\partial \mathcal{R}_{\eta^p, n}^g}{\partial \beta} = \omega_m^p p_p \frac{\partial \alpha_n}{\partial \gamma^p}, \quad \frac{\partial \mathcal{R}_{\pi, n}^g}{\partial \beta} = \mathbf{0}. \quad (80)$$

Thus,  $\partial_{\beta} \eta_n^p$  and  $\partial_{\beta} \pi_n$  are obtained as follows:

$$\frac{\partial \tilde{\xi}_n}{\partial \beta} = \mathcal{K}_{\text{local}, n}^{\text{adjoint-1}} \cdot \frac{\partial \mathcal{R}_{\tilde{\xi}, n}^g}{\partial \beta}, \quad (81)$$

where

$$\begin{aligned} \frac{\partial \tilde{\xi}_n}{\partial \beta} &= \left[ \frac{\partial \eta_n^p}{\partial \beta} \quad \frac{\partial \pi_{11, n}}{\partial \beta} \quad \frac{\partial \pi_{22, n}}{\partial \beta} \quad \frac{\partial \pi_{33, n}}{\partial \beta} \quad \frac{\partial \pi_{23, n}}{\partial \beta} \quad \frac{\partial \pi_{13, n}}{\partial \beta} \quad \frac{\partial \pi_{12, n}}{\partial \beta} \right]^T, \\ \frac{\partial \mathcal{R}_{\tilde{\xi}, n}^g}{\partial \beta} &= \left[ \frac{\partial \mathcal{R}_{\eta^p, n}^g}{\partial \beta} \quad \frac{\partial \mathcal{R}_{\pi_{11}, n}^g}{\partial \beta} \quad \frac{\partial \mathcal{R}_{\pi_{22}, n}^g}{\partial \beta} \quad \frac{\partial \mathcal{R}_{\pi_{33}, n}^g}{\partial \beta} \quad 2 \frac{\partial \mathcal{R}_{\pi_{23}, n}^g}{\partial \beta} \quad 2 \frac{\partial \mathcal{R}_{\pi_{13}, n}^g}{\partial \beta} \quad 2 \frac{\partial \mathcal{R}_{\pi_{12}, n}^g}{\partial \beta} \right]^T. \end{aligned} \quad (82)$$



(a) Overview (There are 30000 integration points in the design domain, and only some of them are plotted at equal intervals along the x- and y-axes. The red and blue colors mean that the curves are drawn with fixed y and x coordinates, respectively.)

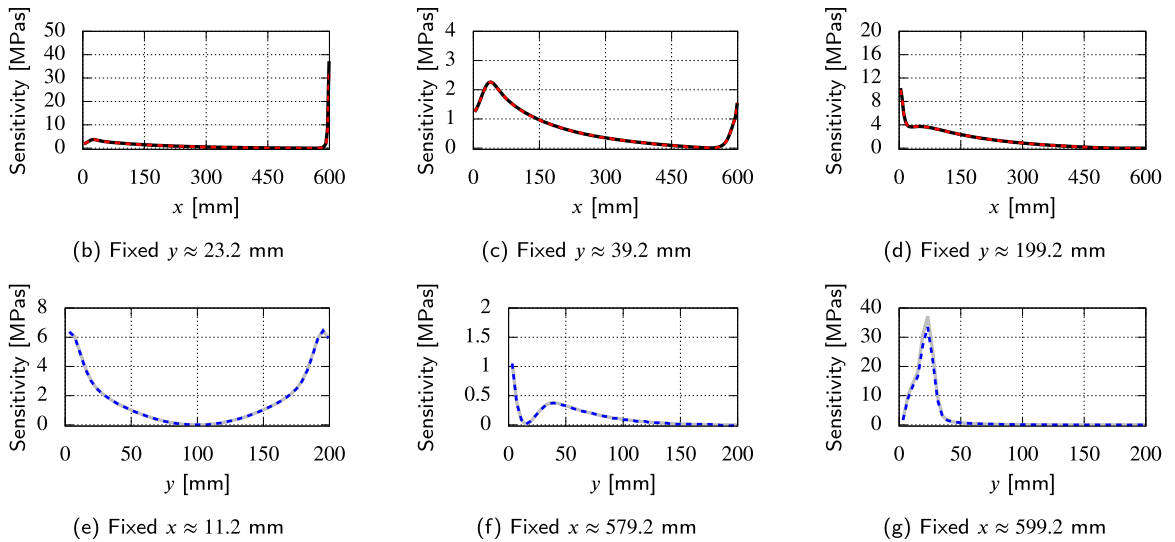


Fig. 33. Comparison of analytical and approximated sensitivity for Example 1: Case  $h10^2$ -sub.

B.3. Supplemental explanation for how to determine the penalty multipliers

Suppose  $m = 1$  is given. Then, the penalty multiplier  $\theta_1$  is calculated as follows:

$$\int_{D_0} \bar{s}_{D_0,1} dV = \int_{D_0} \theta_1 \frac{1}{\omega_1} \prod_{k=1}^1 \omega_k dV \Rightarrow \theta_1 = \frac{\int_{D_0} \bar{s}_{D_0,1} dV}{\int_{D_0} dV}. \tag{83}$$

When  $m = 2$  is considered, the penalty multipliers  $\theta_1$  and  $\theta_2$  are calculated as follows:

$$\begin{aligned} \int_{D_0} \bar{s}_{D_0,1} dV &= \begin{bmatrix} \int_{D_0} \omega_2 dV & \int_{D_0} (-\omega_2) dV \end{bmatrix} \begin{bmatrix} \theta_1 \\ \theta_2 \end{bmatrix}, \\ \int_{D_0} \bar{s}_{D_0,2} dV &= \begin{bmatrix} \int_{D_0} \omega_1 dV & \int_{D_0} (1 - \omega_1) dV \end{bmatrix} \begin{bmatrix} \theta_1 \\ \theta_2 \end{bmatrix}, \\ \Rightarrow \begin{bmatrix} \theta_1 \\ \theta_2 \end{bmatrix} &= \begin{bmatrix} \int_{D_0} \omega_2 dV & \int_{D_0} (-\omega_2) dV \\ \int_{D_0} \omega_1 dV & \int_{D_0} (1 - \omega_1) dV \end{bmatrix}^{-1} \begin{bmatrix} \int_{D_0} \bar{s}_{D_0,1} dV \\ \int_{D_0} \bar{s}_{D_0,2} dV \end{bmatrix}. \end{aligned} \tag{84}$$

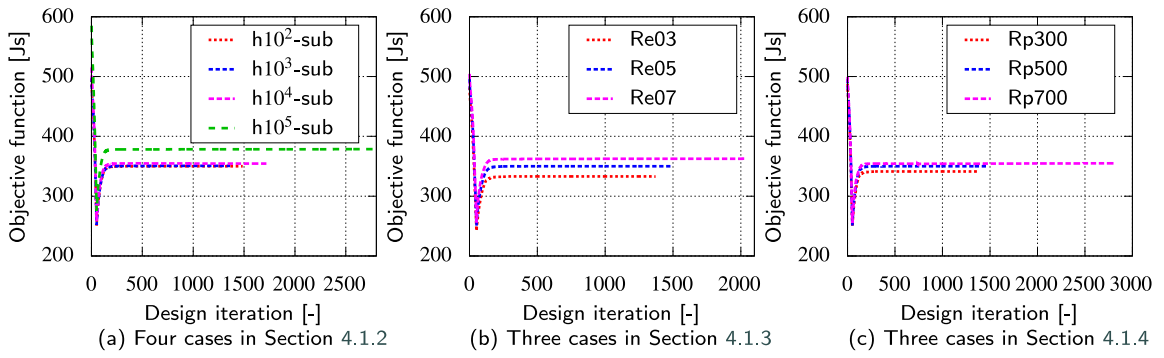


Fig. 34. Histories of objective function for Example 1.

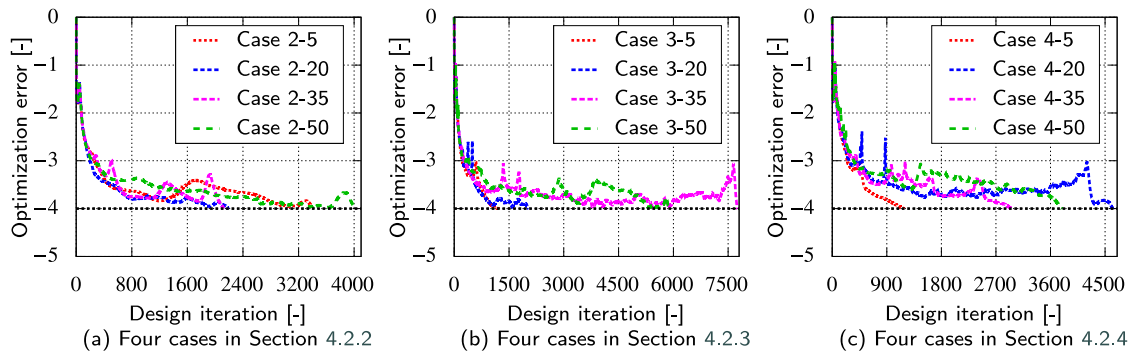


Fig. 35. Optimization error versus design iteration for Example 2: Sections 4.2.2~4.2.4; see Eq. (52).

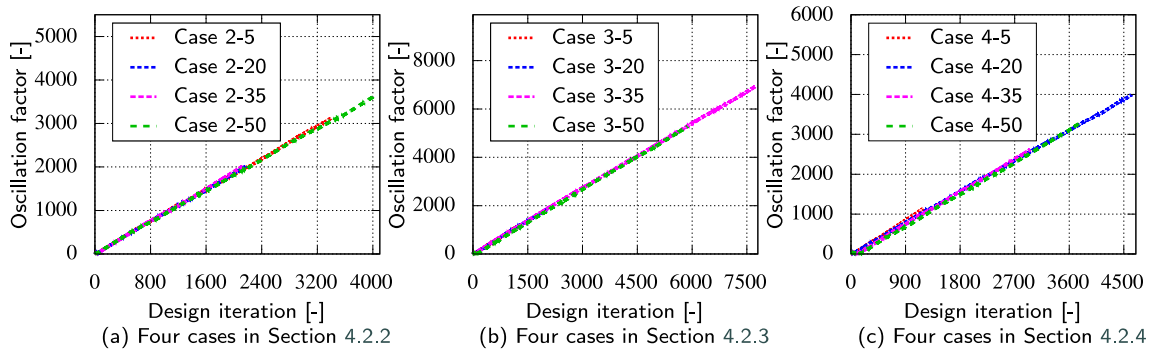


Fig. 36. Oscillation factor versus design iteration for Example 2: Sections 4.2.2~4.2.4; see Eq. (54).

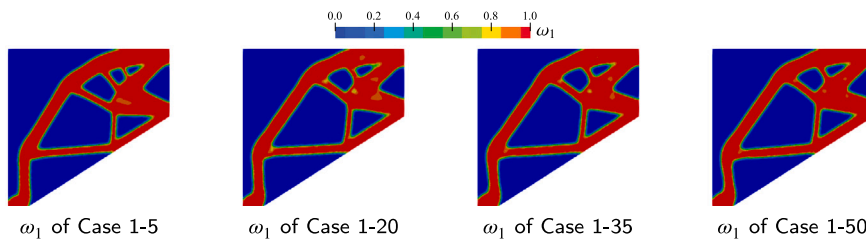


Fig. 37. Distributions of design variables for Example 2: One-material TO. Only half of each specimen is displayed.

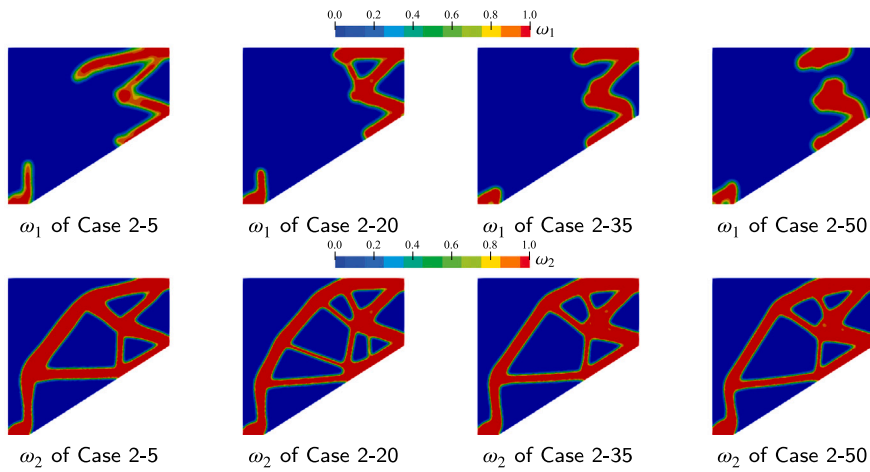


Fig. 38. Distributions of design variables for Example 2: Two-material TO. Only half of each specimen is displayed.

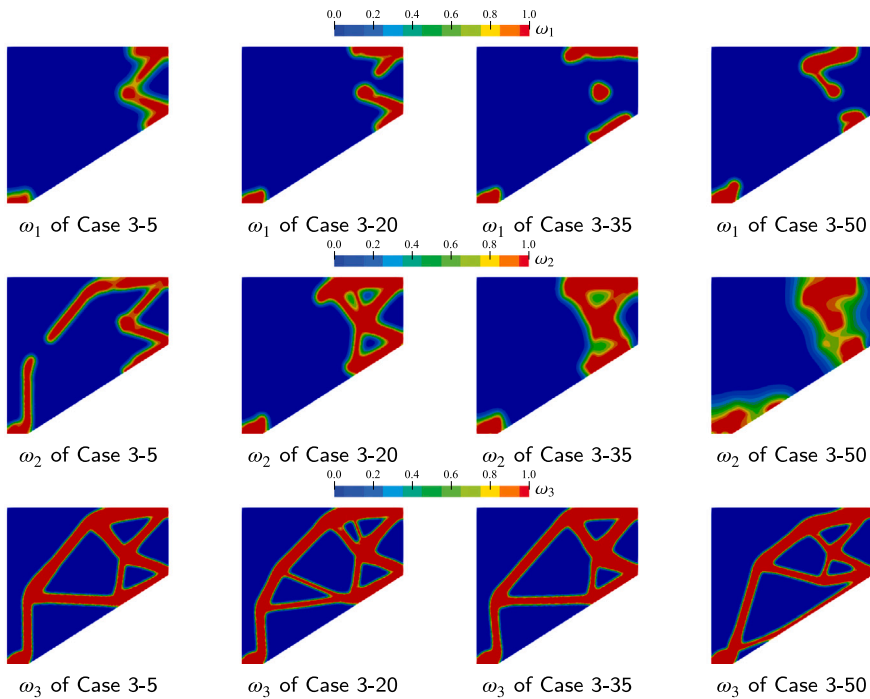


Fig. 39. Distributions of design variables for Example 2: Three-material TO. Only half of each specimen is displayed.

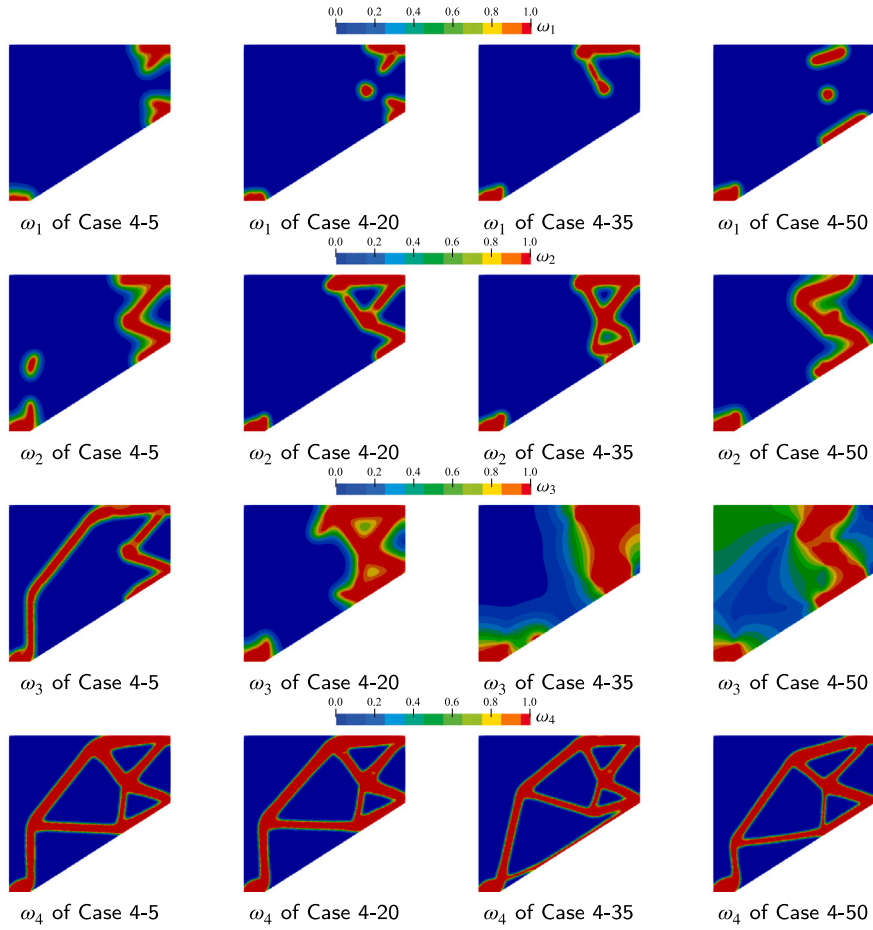


Fig. 40. Distributions of design variables for Example 2: Four-material TO. Only half of each specimen is displayed.

Also, if  $m = 3$  is given, the penalty multipliers  $\theta_1$ ,  $\theta_2$ , and  $\theta_3$  are calculated as follows:

$$\begin{aligned}
 \int_{D_0} \bar{s}_{D_0,1} dV &= \begin{bmatrix} \int_{D_0} \omega_2 \omega_3 dV & \int_{D_0} (-\omega_2 \omega_3) dV & 0 \end{bmatrix} \begin{bmatrix} \theta_1 \\ \theta_2 \\ \theta_3 \end{bmatrix}, \\
 \int_{D_0} \bar{s}_{D_0,2} dV &= \begin{bmatrix} \int_{D_0} \omega_1 \omega_3 dV & \int_{D_0} (-\omega_1 \omega_3 + \omega_3) dV & \int_{D_0} (-\omega_3) dV \end{bmatrix} \begin{bmatrix} \theta_1 \\ \theta_2 \\ \theta_3 \end{bmatrix}, \\
 \int_{D_0} \bar{s}_{D_0,3} dV &= \begin{bmatrix} \int_{D_0} \omega_1 \omega_2 dV & \int_{D_0} (-\omega_1 \omega_2 + \omega_2) dV & \int_{D_0} (-\omega_2 + 1) dV \end{bmatrix} \begin{bmatrix} \theta_1 \\ \theta_2 \\ \theta_3 \end{bmatrix}, \\
 \Rightarrow \begin{bmatrix} \theta_1 \\ \theta_2 \\ \theta_3 \end{bmatrix} &= \begin{bmatrix} \int_{D_0} \frac{\omega_1 \omega_2 \omega_3}{\omega_1} dV & \int_{D_0} \frac{(-\omega_1 \omega_2 \omega_3)}{\omega_1} dV & 0 \\ \int_{D_0} \frac{\omega_1 \omega_2 \omega_3}{\omega_2} dV & \int_{D_0} \frac{(\omega_2 \omega_3 - \omega_1 \omega_2 \omega_3)}{\omega_2} dV & \int_{D_0} \frac{(-\omega_2 \omega_3)}{\omega_2} dV \\ \int_{D_0} \frac{\omega_1 \omega_2 \omega_3}{\omega_3} dV & \int_{D_0} \frac{(\omega_2 \omega_3 - \omega_1 \omega_2 \omega_3)}{\omega_3} dV & \int_{D_0} \frac{(\omega_3 - \omega_2 \omega_3)}{\omega_3} dV \end{bmatrix}^{-1} \begin{bmatrix} \int_{D_0} \bar{s}_{D_0,1} dV \\ \int_{D_0} \bar{s}_{D_0,2} dV \\ \int_{D_0} \bar{s}_{D_0,3} dV \end{bmatrix}.
 \end{aligned} \tag{85}$$

Based on these relationships, the following relationship is inductively obtained:

$$\begin{aligned}
 & \int_{D_0} \bar{s}_{D_0,i} dV \\
 &= \int_{D_0} (\theta_1 - \theta_2) \frac{1}{\omega_i} \prod_{k=1}^m \omega_k dV + \int_{D_0} (\theta_2 - \theta_3) \frac{1}{\omega_i} \prod_{k=2}^m \omega_k dV + \dots + \int_{D_0} (\theta_i - \theta_{i+1}) \frac{1}{\omega_i} \prod_{k=i}^m \omega_k dV \\
 &= \theta_1 \left( \int_{D_0} \frac{1}{\omega_i} \prod_{k=1}^m \omega_k dV - \int_{D_0} \frac{1}{\omega_i} \prod_{k=0}^m \omega_k dV \right) + \theta_2 \left( \int_{D_0} \frac{1}{\omega_i} \prod_{k=2}^m \omega_k dV - \int_{D_0} \frac{1}{\omega_i} \prod_{k=1}^m \omega_k dV \right) \\
 &+ \dots + \theta_{i+1} \left( \int_{D_0} \frac{1}{\omega_i} \prod_{k=i+1}^m \omega_k dV - \int_{D_0} \frac{1}{\omega_i} \prod_{k=i}^m \omega_k dV \right) = \chi_i \cdot \theta,
 \end{aligned} \tag{86}$$

where

$$\begin{aligned}
 \chi_i &= \left[ \chi_i^{1,0} \quad \chi_i^{2,1} \quad \dots \quad \chi_i^{i-1,i-2} \quad \chi_i^{i,i-1} \quad \chi_i^{i+1,i} \quad \dots \quad \chi_i^{m-1,m-2} \quad \chi_i^{m,m-1} \right], \\
 \theta &= \left[ \theta_1 \quad \theta_2 \quad \dots \quad \theta_{i-1} \quad \theta_i \quad \theta_{i+1} \quad \dots \quad \theta_{m-1} \quad \theta_m \right]^T, \\
 \text{with } \chi_i^{j,j-1} &= \int_{D_0} \frac{1}{\omega_i} \prod_{k=j}^m \omega_k dV - \int_{D_0} \frac{1}{\omega_i} \prod_{k=j-1}^m \omega_k dV.
 \end{aligned} \tag{87}$$

Accordingly, the penalty multipliers of multiple materials are obtained as

$$\begin{bmatrix} \theta_1 \\ \theta_2 \\ \vdots \\ \theta_i \\ \vdots \\ \theta_{m-1} \\ \theta_m \end{bmatrix} = \begin{bmatrix} \chi_1^{1,0} & \chi_1^{2,1} & 0 & \dots & & & & & & \\ \chi_2^{1,0} & \chi_2^{2,1} & \chi_2^{3,2} & 0 & \dots & & & & & \\ \vdots & \\ \chi_i^{1,0} & \chi_i^{2,1} & \chi_i^{3,2} & \dots & \chi_i^{i,i-1} & \chi_i^{i+1,i} & 0 & \dots & & \\ \vdots & \\ \chi_{m-1}^{1,0} & \chi_{m-1}^{2,1} & \chi_{m-1}^{3,2} & \dots & \chi_{m-1}^{i,i-1} & \chi_{m-1}^{i+1,i} & \dots & \chi_{m-1}^{m-1,m-2} & \chi_{m-1}^{m,m-1} & \\ \chi_m^{1,0} & \chi_m^{2,1} & \chi_m^{3,2} & \dots & \chi_m^{i,i-1} & \chi_m^{i+1,i} & \dots & \chi_m^{m-1,m-2} & \chi_m^{m,m-1} & \end{bmatrix}^{-1} \begin{bmatrix} \int_{D_0} \bar{s}_{D_0,1} dV \\ \int_{D_0} \bar{s}_{D_0,2} dV \\ \vdots \\ \int_{D_0} \bar{s}_{D_0,i} dV \\ \vdots \\ \int_{D_0} \bar{s}_{D_0,m-1} dV \\ \int_{D_0} \bar{s}_{D_0,m} dV \end{bmatrix}. \tag{88}$$

It is noted that the original penalty multipliers in Eq. (88) are multiplied by exponential functions for imposing the volume constraints effectively. Thus, in the main part of this paper,  $\theta$  in Eq. (88) is written by  $\bar{\theta}$ .

Similarly, the normalization factor  $C_{D_0,i}$  is calculated by

$$\begin{bmatrix} \frac{1}{C_{D_0,1}} \\ \frac{1}{C_{D_0,2}} \\ \vdots \\ \frac{1}{C_{D_0,i}} \\ \vdots \\ \frac{1}{C_{D_0,m-1}} \\ \frac{1}{C_{D_0,m}} \end{bmatrix} = \begin{bmatrix} \chi_1^{1,0} & \chi_1^{2,1} & 0 & \dots & & & & & & \\ \chi_2^{1,0} & \chi_2^{2,1} & \chi_2^{3,2} & 0 & \dots & & & & & \\ \vdots & \\ \chi_i^{1,0} & \chi_i^{2,1} & \chi_i^{3,2} & \dots & \chi_i^{i,i-1} & \chi_i^{i+1,i} & 0 & \dots & & \\ \vdots & \\ \chi_{m-1}^{1,0} & \chi_{m-1}^{2,1} & \chi_{m-1}^{3,2} & \dots & \chi_{m-1}^{i,i-1} & \chi_{m-1}^{i+1,i} & \dots & \chi_{m-1}^{m-1,m-2} & \chi_{m-1}^{m,m-1} & \\ \chi_m^{1,0} & \chi_m^{2,1} & \chi_m^{3,2} & \dots & \chi_m^{i,i-1} & \chi_m^{i+1,i} & \dots & \chi_m^{m-1,m-2} & \chi_m^{m,m-1} & \end{bmatrix}^{-1} \begin{bmatrix} \int_{D_0} |\bar{s}_{D_0,1}| dV \\ \int_{D_0} |\bar{s}_{D_0,2}| dV \\ \vdots \\ \int_{D_0} |\bar{s}_{D_0,i}| dV \\ \vdots \\ \int_{D_0} |\bar{s}_{D_0,m-1}| dV \\ \int_{D_0} |\bar{s}_{D_0,m}| dV \end{bmatrix}. \tag{89}$$

It is noted other normalization factors  $C_{\partial D_0^N,1,\bar{n}}$  and  $C_{\partial D_0^D,1,\bar{n}}$  can be calculated by a similar manner as in Eq. (89). Since the sensitivity on the Neumann and Dirichlet boundaries eventually vanishes in numerical examples, corresponding manipulations are omitted in this study.

### Appendix C. Supplemental information for the numerical examples

See Figs. 33–40.

### Data availability

Data will be made available on request.

## References

- [1] M.P. Bendsøe, N. Kikuchi, Generating optimal topologies in structural design using a homogenization method, *Comput. Methods Appl. Mech. Engrg.* 71 (2) (1988) 197–224, [http://dx.doi.org/10.1016/0045-7825\(88\)90086-2](http://dx.doi.org/10.1016/0045-7825(88)90086-2).
- [2] M.P. Bendsøe, O. Sigmund, Material interpolation schemes in topology optimization, *Arch. Appl. Mech. (Ing. Archiv)* 69 (1999) 635–654, <http://dx.doi.org/10.1007/s004190050248>.
- [3] M.Y. Wang, X. Wang, Color level sets: a multi-phase method for structural topology optimization with multiple materials, *Comput. Methods Appl. Mech. Engrg.* 193 (2004) 469–496, <http://dx.doi.org/10.1016/j.cma.2003.10.008>.
- [4] Y. Wang, Z. Luo, Z. Kang, N. Zhang, A multi-material level set-based topology and shape optimization method, *Comput. Methods Appl. Mech. Engrg.* 283 (2015) 1570–1586, <http://dx.doi.org/10.1016/j.cma.2014.11.002>.
- [5] P. Liu, Y. Luo, Z. Kang, Multi-material topology optimization considering interface behavior via xfem and level set method, *Comput. Methods Appl. Mech. Engrg.* 308 (2016) 113–133, <http://dx.doi.org/10.1016/j.cma.2016.05.016>.
- [6] P. Vogiatis, S. Chen, X. Wang, T. Li, L. Wang, Topology optimization of multi-material negative Poisson's ratio metamaterials using a reconciled level set method, *Computer-Aided Des.* 83 (2017) 15–32, <http://dx.doi.org/10.1016/j.cad.2016.09.009>.
- [7] H. Ghasemi, H.S. Park, T. Rabczuk, A multi-material level set-based topology optimization of flexoelectric composites, *Comput. Methods Appl. Mech. Engrg.* 332 (2018) 47–62, <http://dx.doi.org/10.1016/j.cma.2017.12.005>.
- [8] P. Gangl, A multi-material topology optimization algorithm based on the topological derivative, *Comput. Methods Appl. Mech. Engrg.* 366 (2020) 113090, <http://dx.doi.org/10.1016/j.cma.2020.113090>.
- [9] S. Zhou, M.Y. Wang, Multimaterial structural topology optimization with a generalized cahn–hilliard model of multiphase transition, *Struct. Multidiscip. Optim.* 33 (2006) 89–111, <http://dx.doi.org/10.1007/s00158-006-0035-9>.
- [10] C.F. Hvejsel, E. Lund, Material interpolation schemes for unified topology and multi-material optimization, *Struct. Multidiscip. Optim.* 43 (2011) 811–825, <http://dx.doi.org/10.1007/s00158-011-0625-z>.
- [11] W. Zuo, K. Saitou, Multi-material topology optimization using ordered simp interpolation, *Struct. Multidiscip. Optim.* 55 (2017) 477–491, <http://dx.doi.org/10.1007/s00158-016-1513-3>.
- [12] Q.X. Lieu, J. Lee, A multi-resolution approach for multi-material topology optimization based on isogeometric analysis, *Comput. Methods Appl. Mech. Engrg.* 323 (2017) 272–302, <http://dx.doi.org/10.1016/j.cma.2017.05.009>.
- [13] J. Gao, Z. Luo, M. Xiao, L. Gao, P. Li, A nurbs-based multi-material interpolation (n-mmi) for isogeometric topology optimization of structures, *Appl. Math. Model.* 81 (2020) 818–843, <http://dx.doi.org/10.1016/j.apm.2020.01.006>.
- [14] P. Liu, Z. Kang, Y. Luo, Two-scale concurrent topology optimization of lattice structures with connectable microstructures, *Addit. Manuf.* 36 (2020) 101427, <http://dx.doi.org/10.1016/j.addma.2020.101427>.
- [15] S. Xu, J. Liu, B. Zou, Q. Li, Y. Ma, Stress constrained multi-material topology optimization with the ordered simp method, *Comput. Methods Appl. Mech. Engrg.* 373 (2021) 113453, <http://dx.doi.org/10.1016/j.cma.2020.113453>.
- [16] Z. Han, K. Wei, Multi-material topology optimization and additive manufacturing for metamaterials incorporating double negative indexes of Poisson's ratio and thermal expansion, *Addit. Manuf.* 54 (2022) 102742, <http://dx.doi.org/10.1016/j.addma.2022.102742>.
- [17] K. Maute, S. Schwarz, E. Ramm, Adaptive topology optimization of elastoplastic structures, *Struct. Optim.* 15 (2) (1998) 81–91, <http://dx.doi.org/10.1007/BF01278493>.
- [18] X. Huang, Y.M. Xie, G. Lu, Topology optimization of energy-absorbing structures, *Int. J. Crashworthiness* 12 (6) (2007) 663–675, <http://dx.doi.org/10.1080/13588260701497862>.
- [19] J. Kato, H. Hoshiba, S. Takase, K. Terada, T. Kyoya, Analytical sensitivity in topology optimization for elastoplastic composites, *Struct. Multidiscip. Optim.* 52 (3) (2015) 507–526, <http://dx.doi.org/10.1007/s00158-015-1246-8>.
- [20] P.B. Nakshatrala, D.A. Tortorelli, Topology optimization for effective energy propagation in rate-independent elastoplastic material systems, *Comput. Methods Appl. Mech. Engrg.* 295 (2015) 305–326, <http://dx.doi.org/10.1016/j.cma.2015.05.004>.
- [21] F. Fritzen, L. Xia, M. Leuschner, P. Breitkopf, Topology optimization of multiscale elastoviscoplastic structures, *Internat. J. Numer. Methods Engrg.* 106 (6) (2016) 430–453, <http://dx.doi.org/10.1002/nme.5122>.
- [22] L. Li, G. Zhang, K. Khandelwal, Topology optimization of energy absorbing structures with maximum damage constraint, *Internat. J. Numer. Methods Engrg.* 112 (7) (2017) 737–775, <http://dx.doi.org/10.1002/nme.5531>.
- [23] G. Zhang, L. Li, K. Khandelwal, Topology optimization of structures with anisotropic plastic materials using enhanced assumed strain elements, *Struct. Multidiscip. Optim.* 55 (6) (2017) 1965–1988, <http://dx.doi.org/10.1007/s00158-016-1612-1>.
- [24] M.A. Herfelt, P.N. Poulsen, L.C. Hoang, Strength-based topology optimisation of plastic isotropic von Mises materials, *Struct. Multidiscip. Optim.* 59 (3) (2019) 893–906, <http://dx.doi.org/10.1007/s00158-018-2108-y>.
- [25] B. Blachowski, P. Tazowski, J. Lógó, Yield limited optimal topology design of elastoplastic structures, *Struct. Multidiscip. Optim.* 61 (5) (2020) 1953–1976, <http://dx.doi.org/10.1007/s00158-019-02447-9>.
- [26] J. Desai, G. Allaire, F. Jouve, C. Mang, Topology optimization in quasi-static plasticity with hardening using a level-set method, *Struct. Multidiscip. Optim.* 64 (5) (2021) 3163–3191, <http://dx.doi.org/10.1007/s00158-021-03034-7>.
- [27] J.B. Russ, H. Waisman, A novel elastoplastic topology optimization formulation for enhanced failure resistance via local ductile failure constraints and linear buckling analysis, *Comput. Methods Appl. Mech. Engrg.* 373 (2021) 113478, <http://dx.doi.org/10.1016/j.cma.2020.113478>.
- [28] N. Noii, H.A. Jahangiry, H. Waisman, Level-set topology optimization for Ductile and Brittle fracture resistance using the phase-field method, *Comput. Methods Appl. Mech. Engrg.* 409 (2023) 115963, <http://dx.doi.org/10.1016/j.cma.2023.115963>.
- [29] M. Wallin, V. Jönsson, E. Wingren, Topology optimization based on finite strain plasticity, *Struct. Multidiscip. Optim.* 54 (4) (2016) 783–793, <http://dx.doi.org/10.1007/s00158-016-1435-0>.
- [30] N. Ivarsson, M. Wallin, D. Tortorelli, Topology optimization of finite strain viscoplastic systems under transient loads, *Internat. J. Numer. Methods Engrg.* 114 (2018) 1351–1367, <http://dx.doi.org/10.1002/nme.5789>.
- [31] N. Ivarsson, M. Wallin, O. Amir, D.A. Tortorelli, Plastic work constrained elastoplastic topology optimization, *Internat. J. Numer. Methods Engrg.* 122 (2021) 4354–4377, <http://dx.doi.org/10.1002/nme.6706>.
- [32] G. Zhang, K. Khandelwal, Gurson–tvergaard–needleman model guided fracture-resistant structural designs under finite deformations, *Internat. J. Numer. Methods Engrg.* 123 (2022) 3344–3388, <http://dx.doi.org/10.1002/nme.6971>.
- [33] J. Han, K. Furuta, T. Kondoh, S. Nishiwaki, K. Terada, Topology optimization of finite strain elastoplastic materials using continuous adjoint method: Formulation, implementation, and applications, *Comput. Methods Appl. Mech. Engrg.* 429 (2024) 117181, <http://dx.doi.org/10.1016/j.cma.2024.117181>.
- [34] K.B. Kim, T.H. Kim, E.H. Lee, Effect of formulation method for plastic deformation rate on topology optimization considering elastic–plastic behavior, *Eur. J. Mech. A Solids* 106 (2024) 105347, <http://dx.doi.org/10.1016/j.euromechsol.2024.105347>.
- [35] J. Han, K. Furuta, T. Kondoh, K. Izui, S. Nishiwaki, K. Terada, Topology optimization for nonlocal elastoplasticity at finite strain, *Comput. Methods Appl. Mech. Engrg.* 435 (2025) 117678, <http://dx.doi.org/10.1016/j.cma.2024.117678>.
- [36] K. Hashiguchi, Subloading surface model in unconventional plasticity, *Int. J. Solids Struct.* 25 (1989) 917–945, [http://dx.doi.org/10.1016/0020-7683\(89\)90038-3](http://dx.doi.org/10.1016/0020-7683(89)90038-3).

- [37] K. Hashiguchi, Y. Yamakawa, *Introduction To Finite Strain Theory for Continuum Elasto-Plasticity*, Wiley, 2012, <http://dx.doi.org/10.1002/9781118437711>.
- [38] K. Hashiguchi, *Foundations of Elastoplasticity: Subloading Surface Model*, Springer International Publishing, 2023, <http://dx.doi.org/10.1007/978-3-030-93138-4>.
- [39] S. Forest, Micromorphic approach for gradient elasticity, viscoplasticity, and damage, *J. Eng. Mech.* 135 (3) (2009) 117–131, [http://dx.doi.org/10.1061/\(asce\)0733-9399\(2009\)135:3\(117\)](http://dx.doi.org/10.1061/(asce)0733-9399(2009)135:3(117)).
- [40] F. Wang, B.S. Lazarov, O. Sigmund, J.S. Jensen, Interpolation scheme for fictitious domain techniques and topology optimization of finite strain elastic problems, *Comput. Methods Appl. Mech. Engrg.* 276 (2014) 453–472, <http://dx.doi.org/10.1016/j.cma.2014.03.021>.
- [41] X.S. Zhang, H. Chi, G.H. Paulino, Adaptive multi-material topology optimization with hyperelastic materials under large deformations: A virtual element approach, *Comput. Methods Appl. Mech. Engrg.* 370 (2020) 112976, <http://dx.doi.org/10.1016/j.cma.2020.112976>.
- [42] M. Otomori, T. Yamada, K. Izui, S. Nishiwaki, Matlab code for a level set-based topology optimization method using a reaction diffusion equation, *Struct. Multidiscip. Optim.* 51 (5) (2015) 1159–1172, <http://dx.doi.org/10.1007/s00158-014-1190-z>.
- [43] J. Han, K. Furuta, T. Kondoh, K. Izui, S. Nishiwaki, K. Terada, Topology optimization with a finite strain nonlocal damage model using the continuous adjoint method, *Comput. Methods Appl. Mech. Engrg.* 432 (2024) 117333, <http://dx.doi.org/10.1016/j.cma.2024.117333>.
- [44] J.C. Simo, T.J.R. Hughes, *Computational inelasticity*, in: *Interdisciplinary Applied Mathematics*, Springer-Verlag, New York, 1998, <http://dx.doi.org/10.1007/b98904>.
- [45] E.A. de Souza Neto, D. Perić, D.R.J. Owen, *Computational Methods for Plasticity*, Wiley, 2008, <http://dx.doi.org/10.1002/9780470694626>.
- [46] R. Toluei, M. Kharazi, Implementation of subloading surface model for hyperelastoplasticity with nonlinear kinematic/isotropic hardening based on reference and intermediate configurations, *Appl. Math. Model.* 121 (2023) 751–779, <http://dx.doi.org/10.1016/j.apm.2023.05.026>.
- [47] R. Toluei, M. Kharazi, The subloading surface model in hyperelastic-based plasticity with time integration algorithms in intermediate and current configurations, *Int. J. Non-Linear Mech.* 162 (2024) 104696, <http://dx.doi.org/10.1016/j.ijnonlinmec.2024.104696>.
- [48] M.K. Darabi, R.K.A. Al-Rub, E.A. Masad, C.-W. Huang, D.N. Little, A modified viscoplastic model to predict the permanent deformation of asphaltic materials under cyclic-compression loading at high temperatures, *Int. J. Plast.* 35 (2012) 100–134, <http://dx.doi.org/10.1016/j.ijplas.2012.03.001>.
- [49] S. Zhang, W. Leng, F. Zhang, Y. Xiong, A simple thermo-elastoplastic model for geomaterials, *Int. J. Plast.* 34 (2012) 93–113, <http://dx.doi.org/10.1016/j.ijplas.2012.01.011>.
- [50] K. Sun, A. Zhou, A multisurface elastoplastic model for frozen soil, *Acta Geotech.* 16 (2021) 3401–3424, <http://dx.doi.org/10.1007/s11440-021-01391-7>.
- [51] A. Asaoka, T. Noda, E. Yamada, K. Kaneda, M. Nakano, An elasto-plastic description of two distinct volume change mechanisms of soils, *Soils Found.* 42 (2002) 47–57, [http://dx.doi.org/10.3208/sandf.42.5\\_47](http://dx.doi.org/10.3208/sandf.42.5_47).
- [52] T. Nakai, M. Hinokio, A simple elastoplastic model for normally and over consolidated soils with unified material parameters, *Soils Found.* 44 (2004) 53–70, [http://dx.doi.org/10.3208/sandf.44.2\\_53](http://dx.doi.org/10.3208/sandf.44.2_53).
- [53] K. Hashiguchi, T. Mase, Y. Yamakawa, Elaborated subloading surface model for accurate description of cyclic mobility in granular materials, *Acta Geotech.* 17 (2022) 699–719, <http://dx.doi.org/10.1007/s11440-021-01203-y>.
- [54] Y. Yamakawa, K. Hashiguchi, T. Sasaki, M. Higuchi, K. Sato, T. Kawai, T. Machishima, T. Iguchi, Anisotropic subloading surface cam-clay plasticity model with rotational hardening: Deformation gradient-based formulation for finite strain, *Int. J. Numer. Anal. Methods Geomech.* 45 (2021) 2321–2370, <http://dx.doi.org/10.1002/nag.3268>.
- [55] K. Hashiguchi, H. Yamazaki, S. Nakane, Y. Kato, G. Rosales-Sosa, M. Ueno, Subloading-elastoplastic constitutive equation of glass, *J. Mater. Sci. Technol.* 185 (2024) 221–232, <http://dx.doi.org/10.1016/j.jmst.2023.10.023>.
- [56] Y. Lai, L. Jin, X. Chang, Yield criterion and elasto-plastic damage constitutive model for frozen sandy soil, *Int. J. Plast.* 25 (2009) 1177–1205, <http://dx.doi.org/10.1016/j.ijplas.2008.06.010>.
- [57] K. Hashiguchi, S. Ozaki, Constitutive equation for friction with transition from static to kinetic friction and recovery of static friction, *Int. J. Plast.* 24 (2008) 2102–2124, <http://dx.doi.org/10.1016/j.ijplas.2008.03.004>.
- [58] K. Hashiguchi, Y. Yamakawa, T. Anjiki, M. Ueno, Comprehensive review of subloading surface model: Governing law of irreversible mechanical phenomena of solids, *Arch. Comput. Methods Eng.* 31 (2024) 1579–1609, <http://dx.doi.org/10.1007/s11831-023-10022-1>.
- [59] J. Han, S. Matsubara, S. Moriguchi, K. Terada, Variational crack phase-field model for ductile fracture with elastic and plastic damage variables, *Comput. Methods Appl. Mech. Engrg.* 400 (2022) 115577, <http://dx.doi.org/10.1016/j.cma.2022.115577>.
- [60] J. Han, S. Matsubara, T. Kondoh, K. Izui, S. Nishiwaki, A general formulation of topology optimization for nonlinear materials incorporating internal variables by the continuous adjoint method, 2025, <http://dx.doi.org/10.13140/RG.2.2.21896.12809>, Preprint.
- [61] J. Han, S. Matsubara, S. Moriguchi, M. Kaliske, K. Terada, Crack phase-field model equipped with plastic driving force and degrading fracture toughness for ductile fracture simulation, *Comput. Mech.* 69 (1) (2022) 151–175, <http://dx.doi.org/10.1007/s00466-021-02087-1>.
- [62] J. Han, S. Matsubara, S. Nishi, K. Takada, M. Muramatsu, M. Omiya, K. Ogawa, K. Oide, T. Kobayashi, M. Murata, S. Moriguchi, K. Terada, Gradient damage model for ductile fracture introducing degradation of damage hardening modulus: implementation and experimental investigations, *Int. J. Fract.* 240 (2) (2023) 183–208, <http://dx.doi.org/10.1007/s10704-022-00681-9>.
- [63] X. Gao, H. Ma, Topology optimization of continuum structures under buckling constraints, *Comput. Struct.* 157 (2015) 142–152, <http://dx.doi.org/10.1016/j.compstruc.2015.05.020>.
- [64] G. Zhang, K. Khandelwal, T. Guo, Finite strain topology optimization with nonlinear stability constraints, *Comput. Methods Appl. Mech. Engrg.* 413 (2023) 116119, <http://dx.doi.org/10.1016/j.cma.2023.116119>.